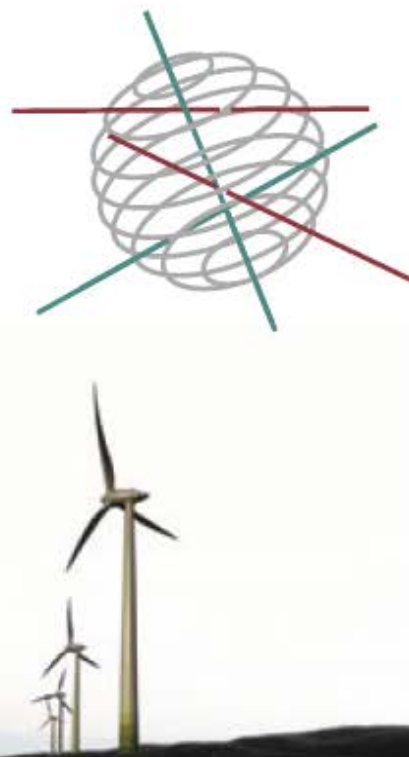# SSD

SCIENCE FOR A SUSTAINABLE DEVELOPMENT

"CONSTRAINING ICE MASS CHANGES IN COASTAL DRONNING MAUD LAND, ANTARCTICA"

«ICECON»

FRANK PATTYN, CARINE BRUYNINX, JEAN-LOUIS TISON, NICOLAS BERGEOT, LIONEL FAVIER, TONIE VAN DAM, REINHARD DREWS, DENIS CALLENS, MORGANE PHILIPPE, KENICHI MATSUOKA, BRYN HUBBARD

ENERGY

TRANSPORT AND MOBILITY

AGRO-FOOD
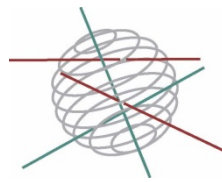
HEALTH AND ENVIRONMENT

CLIMATE

BIODIVERSITY

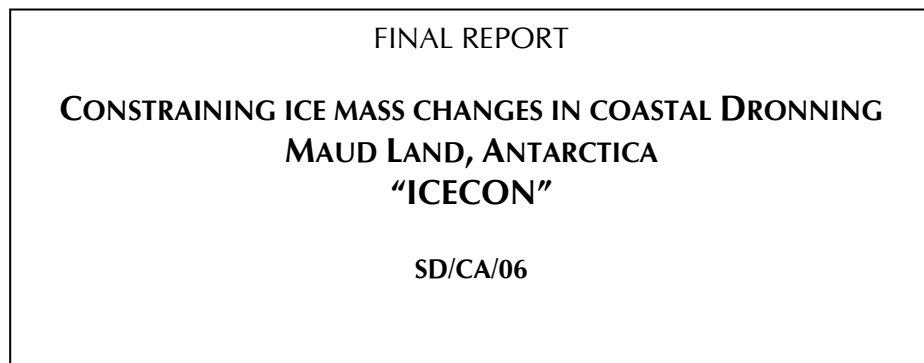ATMOSPHERE AND TERRESTRIAL AND MARINE ECOSYSTEMS

TRANSVERSAL ACTIONS

.be

Thematic Antarctica - Climate

FINAL REPORT

CONSTRAINING ICE MASS CHANGES IN COASTAL DRONNING MAUD LAND, ANTARCTICA
"ICECON"

SD/CA/06

Promotors
Frank PATTYN, Laboratoire de Glaciologie, Université Libre de Bruxelles
Jean-Louis TISON, Laboratoire de Glaciologie, Université Libre de Bruxelles
Carine BRUYNINX, Koninklijke Sterrenwacht van België/Observatoire Royal de Belgique

Authors
Frank PATTYN (1), Carine BRUYNINX (2), Jean-Louis TISON (1), Nicolas BERGEOT (2), Lionel FAVIER (1), Tonie VAN DAM (3), Reinhard DREWS (1), Denis CALLENS (1), Morgane PHILIPPE (1), Kenichi MATSUOKA (4), Bryn HUBBARD (5)

(1) Laboratoire de Glaciologie, Université Libre de Bruxelles
(2) Koninklijke Sterrenwacht van België/Observatoire Royal de Belgique
(3) Faculté des Sciences, de la Technologie et de la Communication, University of Luxembourg, Luxemburg
(4) Norwegian Polar Institute, Norway
(5) Centre for Glaciology, Institute of Geography & Earth Sciences, Aberystwyth University, UK

Frank PATTYN, Carine BRUYNINX, Jean-Louis TISON, Nicolas BERGEOT, Lionel FAVIER, Tonie VAN DAM, Reinhard DREWS, Denis CALLENS, Morgane PHILIPPE, Kenichi MATSUOKA, Bryn HUBBARD. ***Constraining ice mass changes in coastal Dronning Maud Land, Antarctica - ICECON***. Final Report. Brussels : Belgian Science Policy 2018 – 87 p. (Research Programme Science for a Sustainable Development)

Table of Contents

ACRONYMS, ABBREVIATIONS AND UNITS
Liste comme utilisée dans le rapport

ApRES: phase-sensitive radar
BELARE: Belgian Antarctic Research Expedition
BELSPO: Belgian Science Policy Office
DIR: Derwael Ice Rise
DML: Dronning Maud Land
GIA: Glacial Isostatic Adjustment
GNSS: Global Navigational Satellite System
GPS: Global Positioning System
HF: High Frequency
IPF: International Polar Foundation
LF: Low Frequency
LGM: Last Glacial Maximum
PEA: Princess Elisabeth, Antarctica
PGR: Post-Glacial Rebound
POLENET: The Polar Earth Observing Network
PPP: Precise Point Positioning
RBIS: Roi Baudouin Ice Shelf
SCAR: Scientific Committee on Antarctic Research
SERCE: Solid Earth Response and influence on Cryosphere Evolution

SUMMARY

A. CONTEXT

IceCon aims at a better understanding of the past and present ice volumes and extension of the Antarctic ice sheet in Dronning Maud Land (DML) through a new series of measurements and observations in conjunction with ice sheet system modelling. Knowledge of past ice volumes are important, since the ice sheet is still reacting to what happened in the past, especially since the Last Glacial Maximum (LGM), roughly 18,000 years ago, when the Antarctic ice sheet was significantly bigger. Improving this knowledge is one of the prime SCAR Horizon Scan objectives. As a matter of fact, it covers two of the major SCAR Horizon Scan priorities, i.e. (i) understand how, where and why ice sheets lose mass, and (ii) elucidate Antarctica's glacial history.

Because of this prioritized research objective, IceCon is a direct contribution to the SCAR Scientific Research Programme SERCE (Solid Earth Response and influence on Cryosphere Evolution) and AntClim21 (Antarctic Climate Change in the 21st Century). SERCE aims to improve understanding of the solid earth response to cryospheric and tectonic forcing. AntClim21 is aimed to deliver improved regional predictions of key elements of the Antarctic atmosphere, ocean and cryosphere for the next 20 to 200 years and to understand the responses of the physical and biological systems to natural and anthropogenic forcing factors.

The IceCon project is also part of a large initiative to study ice rises and ice shelves in the whole Dronning Maud Land sector in collaboration with Japanese and Norwegian scientists, which is a co-sponsored CliC (Climate and Cryosphere) activity. Finally, the research is part of ISMASS (SCAR/IASC/CliC) – Ice Sheet Mass Balance and Sea Level.

B. OBJECTIVES

The IceCon project aims at a better understanding of the past and present deglaciation of the Antarctic ice sheet in Dronning Maud Land (DML) through a new series of measurements and observations with the aid of ice sheet system modelling. Precise knowledge of past ice volume variations is essential in constraining present-day observations of ice sheet change. The ice sheet imbalance signal is generally obtained by subtracting the supposed isostatic rebound due to past ice volume change from the global observed mass change through satellite gravity observations, such as GRACE. Understanding past and present-day ice flow is essential to improve the prediction of future behaviour and change of the Antarctic ice sheet and its contribution to global sea-level rise. For that, state-of-the-art ice sheet system models controlled using precise observations and measurements are necessary. Moreover, a precise knowledge of the type of ice flow (fast low traction – slow high traction) is essential in evaluating the effect of buttressing ice rises around the Antarctic continent in grounding line migration.

The followed approach is multidisciplinary, involving ice sheet modelling, precise GNSS observations, radio-echo sounding, and ice core drilling and analysis. All applied methods converge to one single objective: reducing the uncertainty on the present-day mass balance in the coastal area of Dronning Maud Land and associated changes herein.

C. CONCLUSIONS

We have an improved understanding on how deglaciation in Antarctic coastal ice sheet areas works. We have shown for the first time that ice rises (pinning points that keep the floating parts of ice sheets in place) are formed during the transition between glacial and interglacial periods, which

significantly slows down the response of the ice sheet to climate change. This is the first study that is able to shed a light on the formation of pinning points and ice rises.

The coastal shelf area has not been ridden over by a large and thick grounded ice sheet during the last glaciation. Analysis of internal radar reflection layers of the Derwael ice rise in Dronning Maud Land point to a long time stability of the ice flow in this region and the fact that the ice rise remained a local flow feature for at least 6000 years. The consequence of this observation is that the coastal shelf could not have been overridden by a big grounded ice sheet, as earlier ice sheet simulation suggest, but that a grounding of the ice shelf during the LGM led to the formation of large (and low-topography) ice streams flowing around the ice rise.

Present day surface mass balance is increasing, a signal that has not been detected before. We have been able to reconstruct the snow accumulation history at Derwael ice Rise across the 1747-2012 time interval, taking into account firnification and ice deformation following two different models. The long-term annual accumulation is between 0.39 and 0.46 m/y water equivalent. Whichever deformation scenario is used, all curves show a positive accumulation trend with time. The steepest increase occurs between the periods 1902-1955 and 1955-1992 (36% to 45%), although this percentage is of course dependent on the time windows used. On longer time scales (1768-1955 vs. 1955-2012), a 55% to 84% increase is observed. To our knowledge, this is the longest record with steady increase of the accumulation rate in this sector of the Antarctic.

Surface mass balance (SMB) is spatially very heterogenous across ice rises. While SMB is generally constant over flat areas, such as ice shelves, the highest variability is found over ice rises. This variability is, in places, higher than across the continental sectors of Dronning Maud Land. The reason of the heterogeneity is found in the effect of wind erosion and deposition. IceCon made the link between high-resolution SMB modelling, direct ice-core evidence and near surface radar measurements.

We developed a novel method to infer vertical strain rates near the surface by combining several measurement techniques and independently from modelling. The main advantage of the method is that it may help deciphering the variability in deformation rates in the presence of melt layers.

Ice-sheet changes since LGM have been minor in the area between the Sor Rondane Mountains and the coast. Analysis of the post-glacial rebound (PGR), based on geodetic GNSS measurements between the Sor Rondane Mountains and the coast, reveal a very low signal in present vertical variations of the lithosphere. This corroborates the lack of a very thick ice cover in this area during the LGM.

Major future ice sheet changes are anticipated in the grounded ice sheet of adjacent ice shelves of the Roi Baudouin ice shelf. In order to make predictions of future ice-sheet behaviour and its potential contribution to global sea level rise, ice sheet models need to be inialized to the present-day situation. Such initialization is based on satellite remote sensing data of surface ice sheet/ice shelf velocity and present-day observed geometry (ice thickness). We have shown that inaccurate mapping of ice-shelf pinning points results in an erroneous initial ice sheet state, which hampers correct projections, leading to an underestimation of potential ice-sheet collapse in overdeepened basins of the grounded ice sheet, also known as Marine Ice Sheet Instability (MISI). The occurrence of future MISIs in the Dronning Maud Land sector has been shown for projected basal melt rates underneath the ice shelves, leading to significant ice loss in the marine area.

D. CONTRIBUTION OF THE PROJECT IN A CONTEXT OF SCIENTIFIC SUPPORT TO A SUSTAINABLE DEVELOPMENT POLICY

We have been able to provide refined estimates of LGM ice mass change and present-day isostatic uplift rates on a regional scale (coastal area of DML) at both sides of the present-day grounding line. Results of the project have shed a new light on the mechanisms of ice flow dynamics between the ice sheet and the ice shelf in DML, Antarctica, which is directly related to objectives of SCAR. This gave rise to better constraints on ice discharge in coastal DML and therefore the results will automatically feed into IPCC AR6 (understanding present-day ice sheet dynamics and processes). It will also aid in improving models of isostatic rebound that are used to determine the present-day ice sheet imbalance from satellites, such as GRACE, particularly in this area.

The glaciological measurements on the Derwael ice rise also serve as a preparation for future deep drilling in such ice rises. Ice rises can be regarded as climatic dipsticks of the ice sheet. Due to their local ice flow pattern, they precisely record past climatic variations in their vicinity without being distorted by ice flow from the Antarctic interior. As preliminary modelling suggests, the age of the bottom ice layers of Derwael varies between 4000 years at 90% ice depth and 8000 years at 98% depth, which in view of the relatively high accumulation rates will assure a high resolution climatic record of the last millennium, which is a contribution to IPICS (International Partnership in Ice Core Sciences). The high-resolution chemical measurements in the Derwael Ice Rise ice cores contribute to a better understanding of the recent climate fluctuations in the framework of the IPICS y-2k sub-program.

E. KEYWORDS

Antarctica, Postglacial Isostatic Rebound, Ice Sheet Deglaciation, Sea-Level Rise, Ice Sheet Mass Balance

1. INTRODUCTION

The IceCon project aims at a better understanding of the past and present deglaciation of the Antarctic ice sheet in Dronning Maud Land (DML) through a new series of measurements and observations with the aid of ensemble experiments using ice sheet system modelling. Precise knowledge of past ice volume variations is essential in constraining present-day observations of ice sheet change. The ice sheet imbalance signal is generally obtained by subtracting the supposed isostatic rebound due to past ice volume change from the global observed mass change through satellite gravity observations, such as GRACE. Understanding past and present-day ice flow is essential to improve the prediction of future behaviour and change of the Antarctic ice sheet and its contribution to global sea-level rise. For that, state-of-the-art ice sheet system models controlled using precise observations and measurements are necessary. Moreover, a precise knowledge of the type of ice flow (fast low traction – slow high traction) is essential in evaluating the effect of buttressing ice rises around the Antarctic continent in grounding line migration.

The followed approach is multidisciplinary, involving ice sheet modelling, precise GNSS observations, radio-echo sounding, and ice core drilling and analysis. All applied methods converge to one single objective: reducing the uncertainty on LGM ice volumes and the associated timing of deglaciation of the Antarctic ice sheet in DML. The setup of a series of continuous GNSS measurements of isostatic rebound on isolated nunataks in the coastal area of DML forms part of a global network of continuous measurements all around Antarctica.

The report describes first the different methodologies applied (GNNS measurements, ice core analysis, Optical Televiewer imaging, ice-radar measurements), followed by an overview of the different findings using these techniques, i.e. reconstruvtion of surface mass balance variability (both temporaly and spatially. The final sections pertain to the long-term stability of the ice sheet in this area since Last Glacial Maximum and the potential of future instability due to sub-ice shelf melting and ocean warming.

2. METHODOLOGY AND RESULTS

2.1. cGNSS processing and results

High precision GNSS stations allow estimating in their vicinity, the motion of the upper part of the Earth's crust in response to past and present mass balance of ice sheet (e.g. Bevis et al., 2012). Such crustal motions are at mm/yr to cm/yr level and affect mainly the vertical component. Consequently, in order to retrieve the 3D velocity motion of the stations, it is necessary to estimate daily 3D-positions with mm-level accuracy. For that, we need a network of stations installed on stable places, in order to avoid any second order motion (e.g. slip motion due to fractured rock …).

For that reason, we installed during the 2012-2103 and 2013-2014 BELARE seasons three high-precision GNSS stations called ULX1, ROB1 and ROB2 (Figure 2.1.1). The infrastructure for these stations was prepared in collaboration with UNAVCO (USA), in order to allow continuous data acquisition without any external power supply (e.g. supply from the Princess Elisabeth Antarctic (PEA) polar base). To achieve this goal, the GNSS receivers are connected to batteries powered by solar panels and wind turbines.

The continuous GNSS stations ULX1 (installed in 2012 on stable rock at Seal Nunatak) and ROB1 (installed in 2012 on the Derwael ice rise, 250 km north of PEA) have been revisited every BELARE season (2013-2014, 2014-2015 and 2015-2016).

The ROB2 station (installed in 2013) is installed on stable rock at the Yet Yuten nunatak in the Röysane mountain range, at an altitude of 2371 m, 40 km south west of PEA. The ROB2 station completes the network of 5 cGNSS stations (2 from the GIANT project and 3 from the IceCon project) distributed over a line from the coast to the SW of PEA.
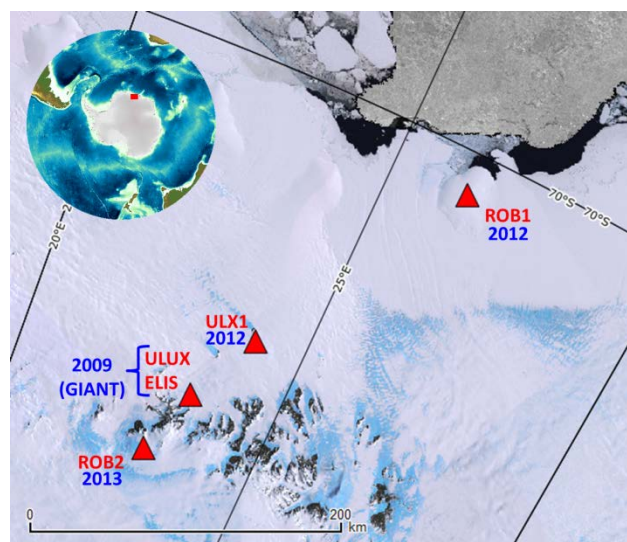
Figure 2.1.1: *GNSS stations installed in the frame of the IceCon and GIANT projects.*

At ROB1 the data acquisition ran all year round. At the same time, the antenna was uplifted to account for the snow accumulation and antenna subsidence during the winter. During the expedition of 2015-2016, the ROB1 station has been dismantled in order to maintain ROB2.

The main problem encountered at ROB2 and ULX1 stations was related to the wind turbines included in the Antarctic GNSS observation system that was purchased from UNAVCO. It seems that during the austral winter the temperature becomes too cold for the grease inside the bearings, causing them to have high friction and insufficient lubrication, shortening the lifespan of the bearings dramatically. If this type of windmill will be used in the future, an investigation on a 'cold climate' version (other grease) of these bearings is required.

The data from these GNSS stations around PEA have been analyzed together with a worldwide well-distributed network composed of 143 reference stations (see Figure 2.1.2). This assures the

computation of unbiased station positions and velocities expressed in the last realization of the International Terrestrial Reference Frame (ITRF2014, Altamimi et al. 2016).
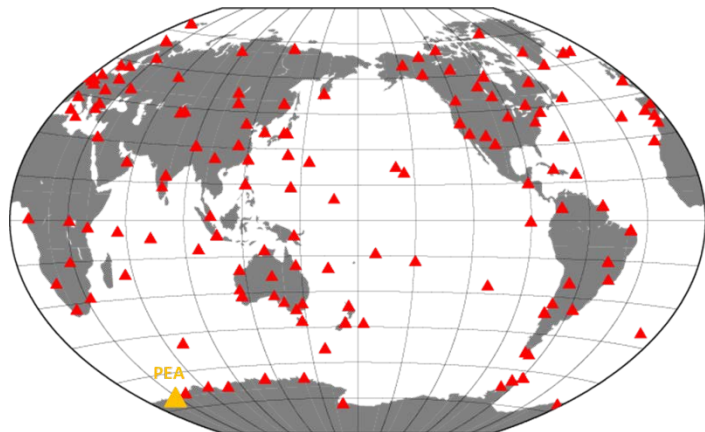
Figure 2.1.2: *Global network of GNSS stations processed since 1998 to achieve mm-level precision on the daily position estimation.*

The reprocessing of the entire network since 1998 has been done using the Bernese 5.2 GNSS software (Dach et al., 2013) and the CATREF software (Altamimi et al. 2007). Annual and semi-annual signals have been estimated and removed from the daily station positions before estimating their velocities. The analysis provides a first approximation of the stations behavior. Figure 2.1.3 shows the motion (as well as its formal error) of the IceCon stations ROB1, ROB2, and ULX1 as well as the station ELIS at the Princess Elisabeth basis (GIANT project).

The station ROB1, installed on the ice on Derwael ice rise, shows a change in its North-velocity from Dec. 2013 (see Table 2.1.1), while its velocity towards the West increases over time. In addition, its subsidence decreases each year. The velocity seems not as linear as expected in that region. The mean subsidence rate is about 1.35 m/year and can be explained by ice and snow compaction, surface thinning and vertical motion of the ice (submergence velocity). Table 2.1.1 gives the station velocities that have been estimated using the presently available data. It is clear that the length of the observation period as well as (bi-)annual signals degrade the accuracy of these estimated velocity for most stations.
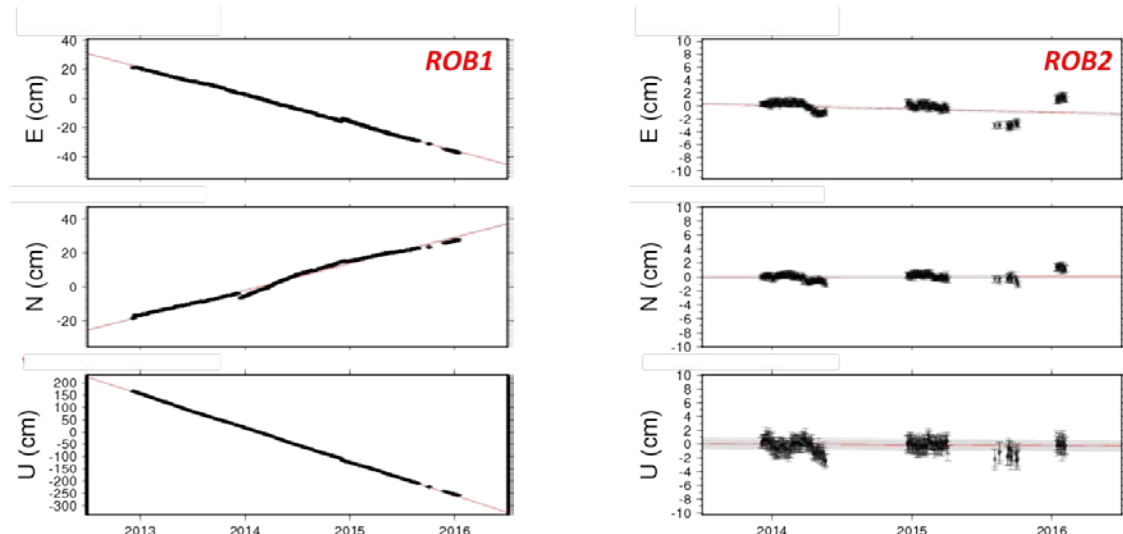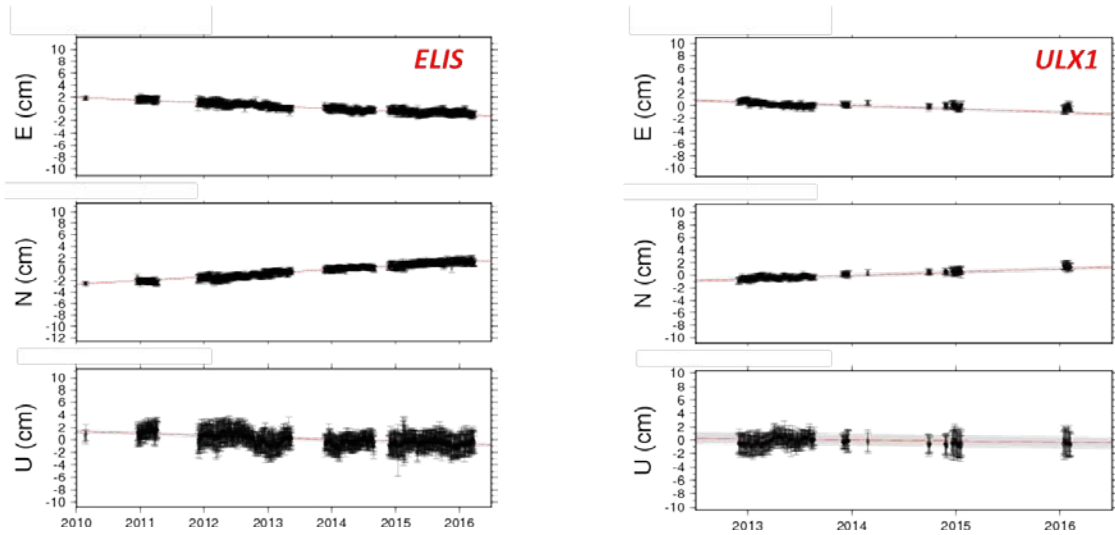
Figure 2.1.3: *Change of the 3D daily estimated coordinates (bottom: vertical; middle: North; top: East) of the GNSS stations based on the data that was gathered up to now.*

Table 2.1.1: *Velocities and (underestimated) formal errors (3 σ) computed for each GNSS station over its complete observation period.*

Station	East [cm/yr]	North [cm/yr]	Up [cm/yr]
ROB1 (12//342-13/346)	-17.7 ± 0.2	14.2 ± 0.3	-139.1 ± 0.9
ROB1 (13/346-14/338)	-20.3 ± 0.2	22.8 ± 0.3	-136.7 ± 1.0
ROB1 (14/338-16/013)	-21.2 ± 0.2	11.6 ± 0.2	-130.0 ± 0.8
ROB2	-0.2 ± 0.1	0.3 ± 0.1	-0.1 ± 0.4
ULX1	-0.4 ± 0.1	0.6 ± 0.1	0.0 ± 0.4
ELIS	-0.5 ± 0.1	0.6 ± 0.1	-0.3 ± 0.1

From our results, the GNSS stations anchored on stable rock around PEA subside at a level of mm/yr. This can be interpreted as a general increase of ice mass in East Antarctica (see Figure 2.1.4) compared to ice mass decrease in West Antarctica.
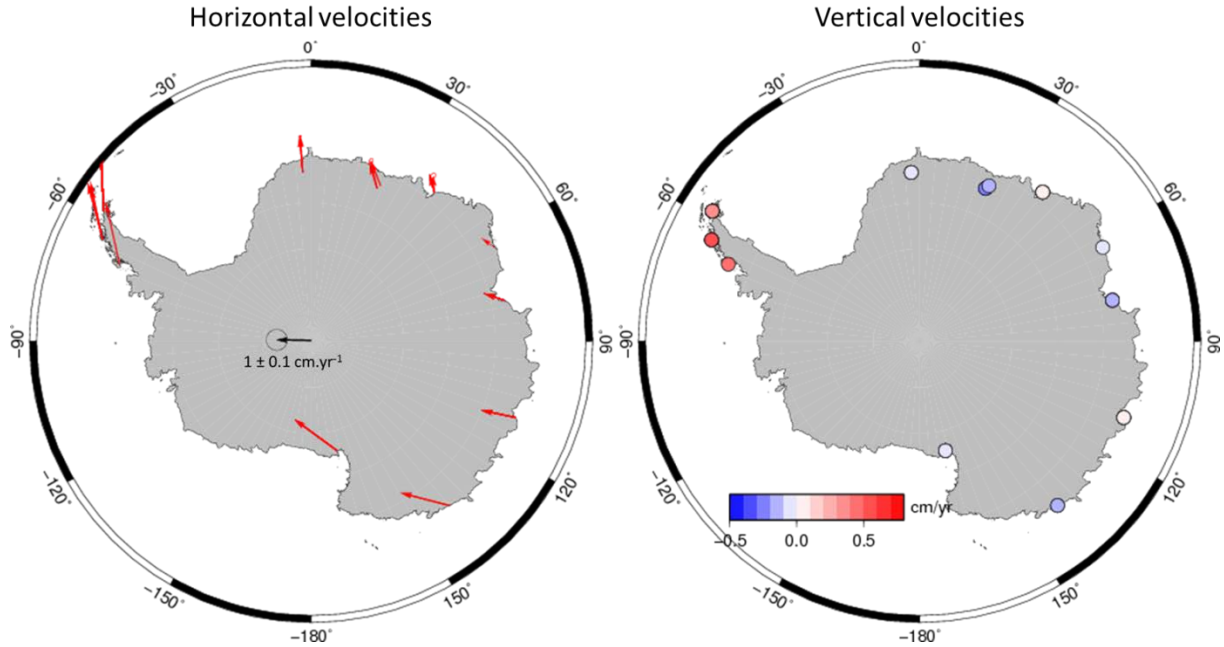
Figure 2.1.4: *Velocity field for Antarctica stations.*

2.2. Ice core drilling and Optical Televiewer imaging (OPTV)

2.2.1. Ice core drilling

Two field trips to the study area of the Princess Ragnhild Coast were dedicated to ice core drilling and optical televiewer measurements in respectively November-December 2012 and 2014. Figure and Table 2.2.1 summarize all the medium-depth (0-120 m) ice cores locations.

During the first field trip, a total of 120 meters of a firn/ice core were recovered from the ice divide of Derwael ice Rise (see IC12 location on Figure 2.2.1) using a Canadian Eclipse Drill, recently acquired by the IPF (International Polar Foundation). A total of 174 core sections with a mean length of 0.48m (min: 0.10m - max: 2.18m) were recovered, and the firn ice transition was observed below ca. 70 meters.
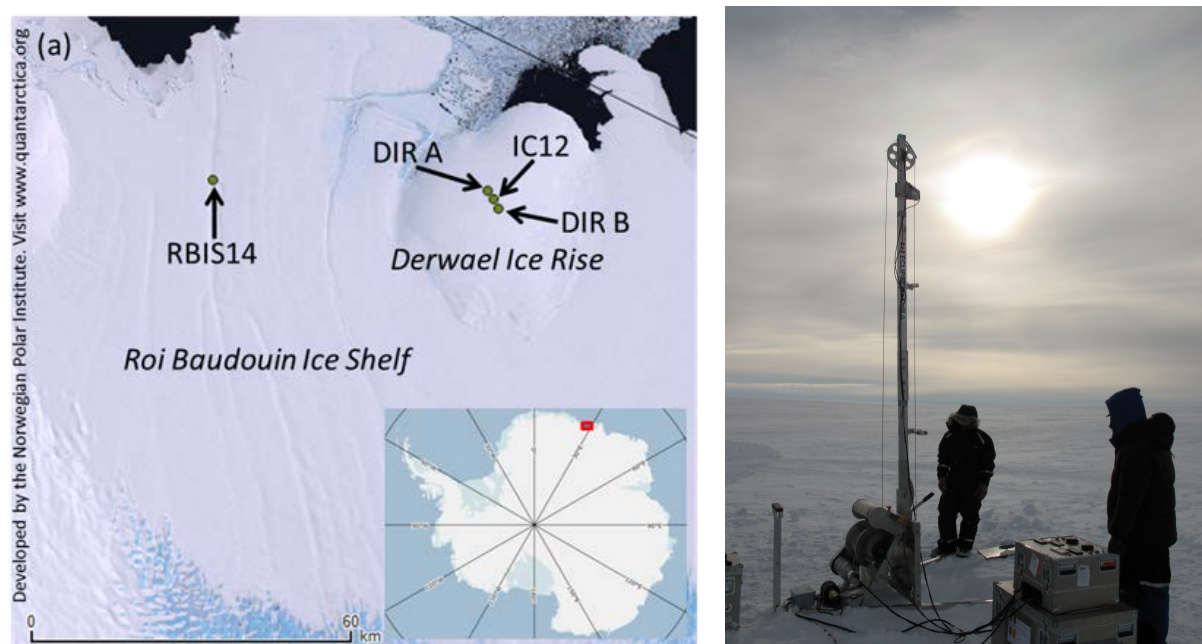
Figure 2.2.1: *Left: location map of the boreholes from the 2012 and 2014 fields trips. The RBIS (2010, BELSPO - Bellissima Project) is also shown. Right: The Eclipse drilling system.*

Directly after retrieval, ice temperatures were measured on each new piece of ice extracted, drilling a small hole 3mm in diameter, at 10 cm from the top or the bottom of the ice piece, fitting exactly the outer diameter of the temperature probe used (TESTO 720). Precision of the measurements is ± 0.1°C. All ice cores have been immediately packed in plastic bags and stored in a -25°C reefer container that has been sent back to Belgium by ship, for further analyses at the Laboratoire de Glaciologie (ULB).

Ice core	Latitude	Longitude
RBIS14	-70.42011	25.03437
DIR A	-70.2362	26.29113
IC12	-70.2458	26.33485
DIR B	-70.25582	26.37974

Table 2.2.1: *location of ice cores of the 2012 and 2014 field campaigns*

Nine secondary shallow firn cores were also drilled manually on the main radar transect (perpendicular to the ice divide crest, 8 kilometres on both sides) in order to document potential spatial variation in surface density.

New ice core drilling was performed during the Nov-Dec 2014 fieldtrip. The rationale focused on two scientific questions: a) what is the accumulation variability between upwind and downwind locations of the 2012 ice core (IC12) at the summit of Derwael Ice Rise? Large variability is indeed expected from the work of Lenaerts et al. (2014), with higher accumulation on the upwind side and lower accumulation (or even erosional relocation) on the downwind side; and b) What are ice shelf ice characteristics within the longitudinal surface trenches as compared to the Derwael Ice Rise and

the rest of the ice shelf sampled close to the western ice rift in 2010 (RBIS10), and can we reach the bottom of the ice shelf (expected at about 120-150 meters) to look for ocean properties (CTD) and indications of marine ice accumulation or active erosion? 30 meters ice cores DIR A and DIR B (see table 2.2.1 for locations) were drilled to reach the first objective, and 107m ice core RBIS14 was performed in an attempt to answer question b).

Unfortunately, the cold chain has been broken for probably several days during the 2014 ice cores transfer to Belgium, in the beginning of year 2015. The reefer arrived in Belgium with a positive temperature of +6°C and clear signs of melting were visible on the samples. This has jeopardized the scientific return of our second fieldtrip in terms of ice cores analyses (see section 2.4).

2.2.2. Optical televiewer measurements

Once cores were recovered, the boreholes were logged by OPTV at a resolution of about 1mm laterally and vertically. OPTV differs in one fundamental respect from traditional (directional) borehole video in that OPTV acquires a geometrically accurate image of the complete borehole wall. This is achieved by the probe's downward-looking digital camera recording a 360° annular image of the borehole wall as reflected in a hyperboloidal mirror (Fig. 2.2.2a and b). Accurate winch control then allows the probe to be raised and lowered at a precise rate along the borehole, typically producing images with a vertical resolution that can be user-set to a pixel dimension as small as 1mm and at a lateral resolution of either 360 or 720 pixels per row (ca.1.0mm and ca. 0.5mm per pixel, respectively, for a borehole of 12cm diameter). This geometrical accuracy provides a powerful means of mapping the structures that intersect a borehole wall because each visible intersecting plane appears as a sinusoidal trace on the raw OPTV image. Here, the dip and dip-direction of each such plane (orientated by magnetometers located within the OPTV probe) are represented respectively by the amplitude and phase of the associated sinusoid (Fig. 2.2.2c and d). Structural analysis of an OPTV log thereby allows all such features to be located, characterized in terms of their thickness and appearance, and their orientations to be logged.
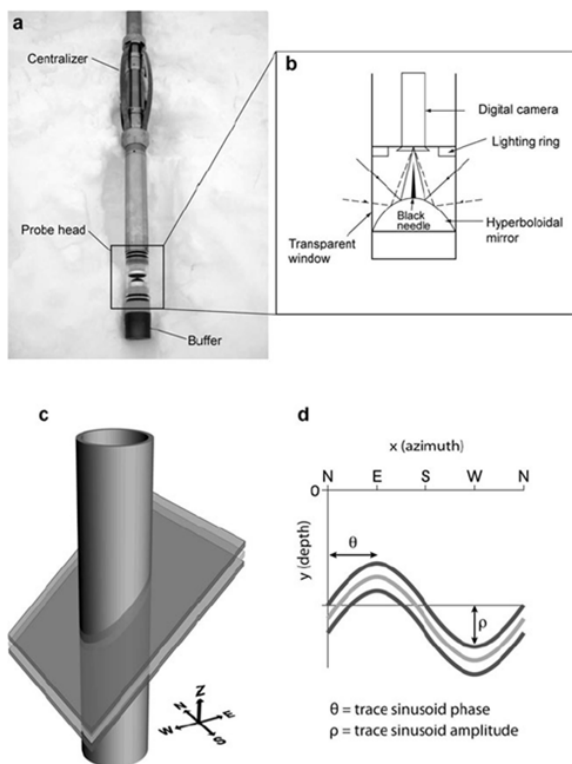

Figure 2.2.2: *Illustration of the principles of OPTV operation. (a) Image of OPTV probe and (b) expanded sketch of probe head, (c) schematic illustration of a borehole intersecting three closely spaced layers dipping west and (d) illustration of their equivalent sinusoids on the raw OPTV image. (Hubbard et al., 2012).*
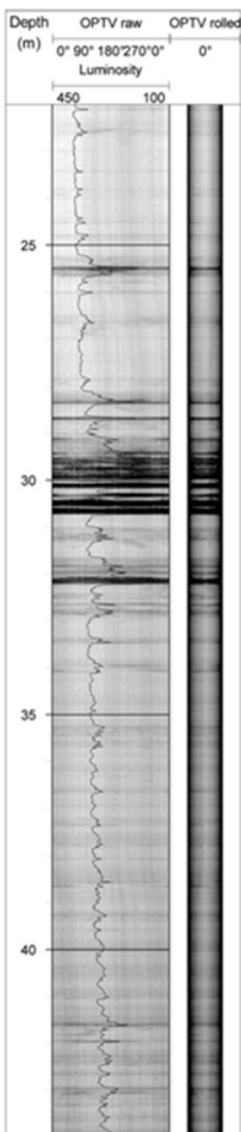
Figure 2.2.3: *OPTV log of the ice-shelf core RBIS-2010 between 20 and 45m. The raw OPTV image is plotted on the left-hand side of each panel and its rolled equivalent is plotted on the right. The luminosity trace overlaid on the raw OPTV image is sampled each millimetre in the vertical and is scaled to decrease, over the range 450–100 (non-dimensioned) units, to the right. (Hubbard et al., 2012)*

Once logged, OPTV images were collated, analysed and prepared for presentation (including rolling to create virtual core images) using WellCAD software (see Fig. 2.2.3 for an example section from the RBIS Ice Shelf drilling in 2010 - BELISSIMA project). This analysis included calculating the luminosity (expressed in non-dimensioned units of RGB pixel brightness) of each 1mm depth step, represented by the mean value of each ring of 720 pixels. Within some metres (depending on the optical transmissivity of the material being cored) of the borehole surface, recorded light is dominated by that transmitted from the surface, but below this zone it is exclusively composed of that reflected back from the borehole walls to the OPTV sensor. Since borehole illumination, achieved by a circular array of white LEDs, is uniform in time and therefore also in space as the probe moves along a borehole, the net luminosity of the recorded signal varies with the reflectivity of the material formi ng the borehole wall.

As discussed by Hubbard et al. (2012), three types of structural information can be retrieved from OPTV data, in this case of the surface firn to ice transition of ice shelves (the RBIS case) or ice rises (the DIR case): a) a large scale trend of steadily decreasing luminosity downwards which is the signature of progressive firnification, specifically the gradual isolation and coalescence of bubbles resulting in a net increase in the optical transmissivity (and concomitant decrease in reflectivity) of the borehole wall; b) a small scale pattern of regularly repeated mildly darker layers, considered as the "primary" layering of annual layers, similar to those previously identified on the basis of directional video by for example Hawley and others (2003) and Hawley and Morris (2006), and c) occasional much darker layers (indicating less reflected light), consistent with bubble-poor ice and an interpretation as refrozen surface melt-layers.

A total of 9 more OPTV logs were performed in 2014 to either re-visit the 2012 Derwael Ice Rise ice core IC12 drill hole (buried under more than 2 meters of new accumulation! - 3 logs) or document the new boreholes: 2 logs in each of DIR A, DIR B and RBIS14 boreholes. Re-visiting the 2012 Derwael Ice Rise drill hole has allowed us to trace down identical markers (mainly ice layers patterns), providing direct measurement of strain between 2012 and 2014, as will be further discussed in section 2.7.

2.3. Laboratory ice core measurements

2.3.1. Ice density measurements

Material density was measured by gravimetry in a -15°C cold room at ULB. Samples, cut by band saw or diamond-wire saw, were recovered at a higher resolution from the RBIS 2010 (collected in 2010 during the BELSPO Bellissima project) core than from the DIR core. Hence, 472 cubes of dimension ~26 mm were cut and analysed from 13 core sections of the former while 48 square-columnar core sections, each of 28 mm side length and 0.05 - 0.25 m long, were cut and analysed from the latter. A total of 40 samples have further been collected from the RBIS14 core to assess the damage caused to the samples from the 2014 field season. Once cut, precise sample dimensions were measured three times in each direction by digital caliper to a precision of 0.02 mm. Each sample was weighed three times by analytical scale to a precision of 0.1 mg. Measurements were repeated on two different samples for each depth interval for the RBIS 2010 core, comparison of which yielded a standard deviation in measured density of <4%. Such an empirical comparison was not carried out for the DIR and RBIS14 samples, but their larger size gives confidence that the error in their measured density is less than that for the RBIS 2010 samples.

2.3.2. Ice chemistry and water stable isotopes measurements

Ice cores sent back to Europe will find their main use in providing a complete high-resolution suite of concentrations (and fluxes) of chemical compounds ($\delta^{18}O$, δD, $SO_4^=$, NO_3^-, Na^+, MSA, Ca^{++}, Cl^-, K^+, Mg^{++}) the seasonal cycle of which will be used in a combined approach to delineate annual layers in the core. Given the expected accumulation and compaction rates a sampling resolution of 10 to 5 cm has been chosen to resolve the seasonality cycle. The cores are cut using a band saw, following the cutting plan shown in Fig. 2.3.1. Pieces from the sides of the core (marked 1 in Fig. 2.3.1) are collected for water stable isotopes measurements. These parts are then melted and bottled before measurements are carried out using a PICARRO L 2130-i laser analyzer (available at the VUB, precision: 0.05‰ for $\delta^{18}O$ and 0.3‰ for δD). Another piece is kept for thin sections observations (marked 2 in Figure 2.3.1)
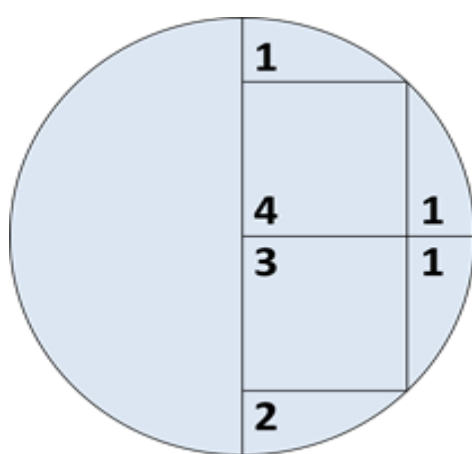
Figure 2.3.1: *Cutting plan. 1) Parts that were used for stable isotopes analysis ($\delta^{18}O$, δD) at the VUB; 2) Part used as a possible basis for thin sections; 3) part decontaminated for Ion chromatography ($SO_4^=$, NO_3^-, NA^+, MSA, Ca^{++}, …), and 4) archive.*

For ion chromatography analyses, a central 3cm on 3 cm beam is cut (marked 3 in Fig. 2.3.1), and fixed on an home-made Teflon holder set up in a laminar flow hood within the cold room laboratory. There, 5 cm long samples are decontaminated again, scraping all sides using a clean microtome knife or a clean razor blade (Figure 2.3.2, left). A clean vial is then fitted around the sample (Figure 2.3.2, right), which is cut by a quick hit of the knife, at its base. Samples are then temporarily stored in the freezer (-25°C), and melted just before the analyses. The cations and anions are analyzed using a new two-channel Dionex ICS 5000 HPLC system acquired on the project (ULB). The two eluent used are MSA (49mM, 0.36 ml/min) for cations separation and KOH (15-40mM, 0.01ml/min) for anions separation. This method has been tested on blank ice samples

and on samples of ice from the Roi Baudouin Ice Shelf in order to measure the expected concentrations levels. The system has a standard deviation of 2 ppb for Na^+ and SO_4^-, 8 ppb for Cl^-, 7 ppb for NO_3^-, and 1 ppb for MSA. Non-sea-salt sulfate was calculated as *nss*SO4 = $[SO_4^-]_{tot} - 0.052 \times [Cl^-]$ following Mulvaney et al. (1992) and represents all SO_4^- not of a marine aerosol origin. The ratio Na^+ / SO_4^- was also calculated as an indicator of seasonal SO_4^- production.
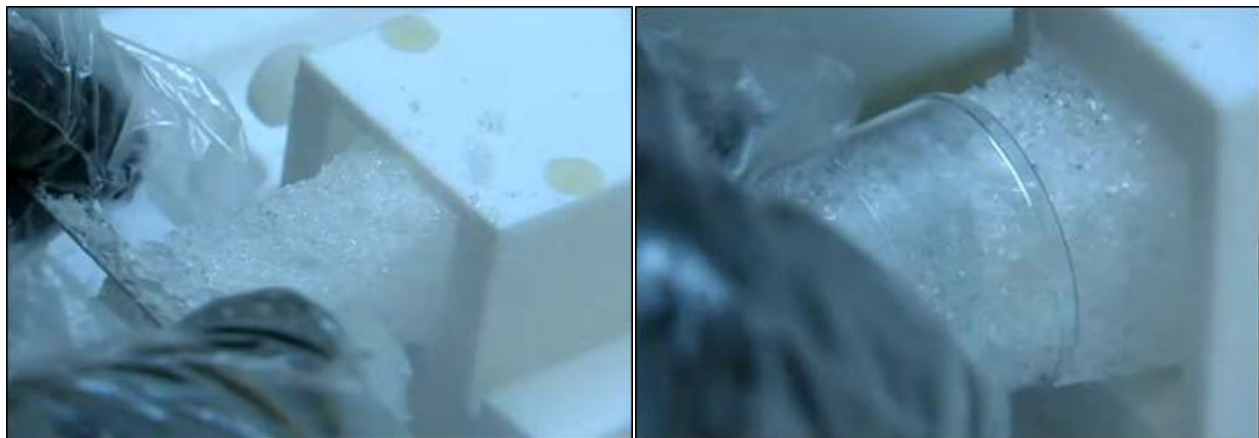
Figure 2.3.2: *decontamination and bottling process under laminar flow hood.*

2.3.3. Electrical conductivity measurements (ECM)

Thanks to our sustained collaboration with our Danish collaborators at the Niels Bohr Institute - University of Copenhagen (NBI), we have been able to obtain ECM measurements on half cores from the IC12 location. These were not planned initially, but helped us to improve our age-depth relationship, including by providing absolute dating on known volcanic eruptions. We used the new ECM device at NBI. The principle is simple: the microtome flattened surface of the half core is scratched with two electrodes sending a DC current into the ice (Figure 2.3.3). The intensity of the current is proportional to ice acidity i.e. to the anionic impurity content located at the crystal boundaries (SO_4^-, NO_3^-, Cl^- …). This impurity content varies seasonally and shows local maxima associated to sulfate production from volcanic eruptions. It can therefore be used both as a relative and absolute dating tool.

As measurements were principally made in firn, we applied the technique described by Kjær et al. (2016) to correct for the effect of firn porosity on the amplitude of the signal. Because ECM scales inversely with air content, we multiplied the measured ECM signal by the ratio of the ice density to firn density (ρ_{ice}/ρ_{firn}), using the gravimetric density best fit from Hubbard et al. (2013). While there are millimetric-scale differences between the optical televiewer log and the ice core depth scales used to derive this best fit, the correlation provides an acceptably high coefficient of determination ($r^2 = 0.96$) for this purpose. ECM data were then smoothed with a 301-point first-order Savitsky-Golay filter (Savitsky and Golay, 1964) which eliminates peaks due to random noise and small-scale variations in material chemical composition, while preserving the larger peaks, including those due to volcanic eruptions. Finally, the ECM data were normalized by subtracting the mean and dividing by the stan- dard deviation following Karlöf et al. (2000).

Fig. 2.3.3 : *ECM measurement on an ice core*

2.4. Density measurements compared to OPTV

2.4.1. Shallow (3 m depth) ice cores across the DIR ice divide

Mean shallow core density increases steadily from East to West along a perpendicular to the DIR ice divide, from 425 kg m^{-3} at 8km East of the divide, on the upwind slope where accumulation is high, to 450 kg m^{-3} at 8km West of the divide, on the downwind slope where accumulation is lower (Figure 2.4.1).
The results are in accordance with predictions from regional climate models (Lenaerts et al., 2014) and triggered our interest in documenting contrasts in accumulation rates on both flanks of Derwael Ice Rise with the two 2014 30m deep DIRA and DIRB ice cores.
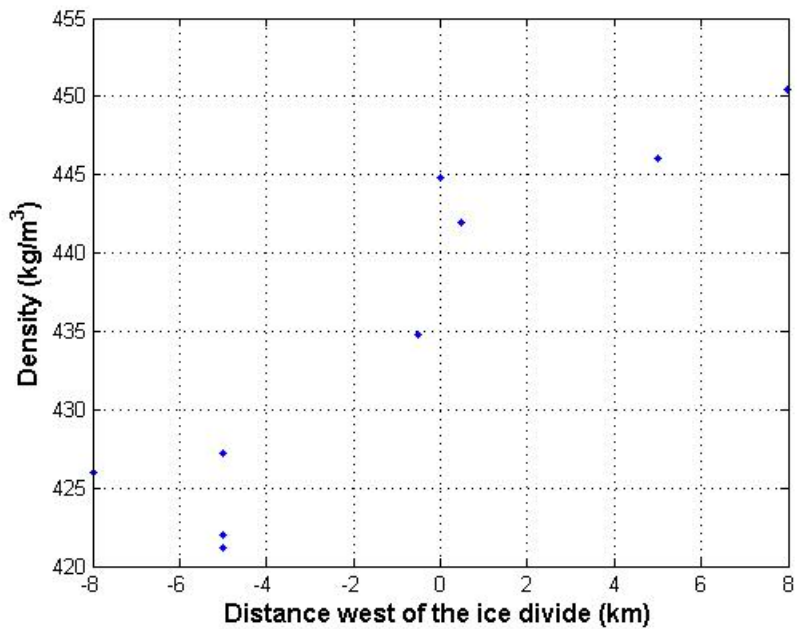
Figure 2.4.1: *Density measured on 3m deep firn cores along a transect 8km East (Upwind) and 8km West (Downwind) from the divide.*

2.4.2. Roi Baudouin Ice Shelf (RBIS 2010) and Derwael Ice rise (DIR-IC12) profiles
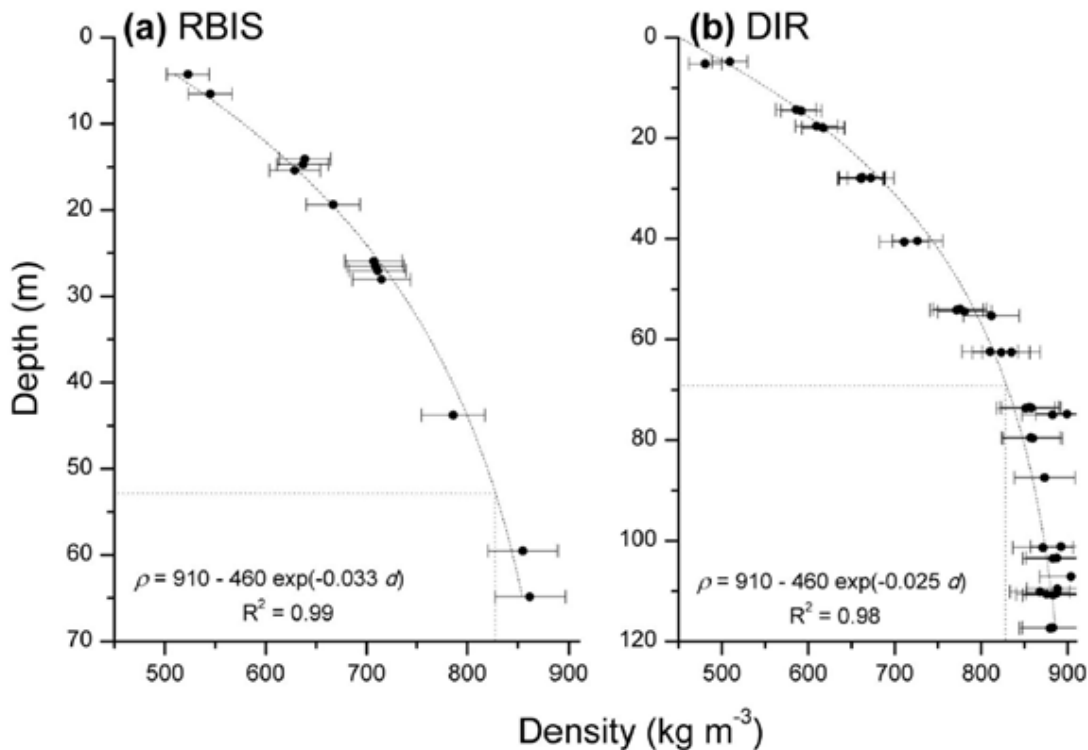
Figure 2.4.2: *Density measured gravimetrically on core samples plotted against depth for (a) the RBIS 2010 core and (b) the DIR-IC12 core. The $\pm 4\%$ bars reflect measured, at-a-depth variation. Dashed line and equation give best-fit exponential relationship between the variables. Dotted lines indicate the location of the firn-ice transition, defined by a density of 830 kg m^{-3} (~ 53 m at RBIS 2010 and ~ 70 m at DIR-IC12). Note the different depth scales.*

Gravimetric density has been measured from discrete samples along both the Roi Baudouin Ice Shelf (RBIS 2010, 2010 - 67 meters) and Derwael Ice Rise (DIR-IC12, 2012 - 118 meters) ice cores. The full RBIS 2010 core shows an increase in density with depth, rising from just under 500 kg m^{-3} at a depth of ∼4 m below the surface to approaching 900 kg m^{-3} at the base of the core. Each core section analyzed is also characterized by high resolution variations in density caused by the presence of small-scale layers along the core. However, for the purpose of analysis at the scale of 100 - 101 m, it is appropriate to exclude these small-scale deviations. We therefore calculate and plot the mean density of each core section sampled against its center-point depth for the RBIS 2010 core. The resulting decimeter scale is similar to that at which the DIR-IC12 core samples were recovered and analyzed. The resulting profiles, illustrated in Figure 2.4.2, show a steady increase in density with depth that may be fit, following Sjögren [2007], to an exponential function of the form:

$$\rho(d) = \rho \text{ ice } - (\rho_{ice} - \rho_{snow}) \exp (\alpha \, d) \qquad (2.4.1)$$

where ρ is density (kg m^{-3}), d is depth below the surface (m), and α is determined empirically. The best fit of our gravimetric density measurements to this function, fixing ρ_{ice} at 910 kg m^{-3} and ρ_{snow} at 450 kg m^{-3}, gives α = -0.033 (R^2 = 0.99) for RBIS 2010 (Figure 2.4.2a) and α = - 0.025 (R^2 = 0.98) for DIR-IC12 (Figure 2.4.2b). These data indicate a more rapid increase in density with depth at RBIS than at DIR-IC12, and that the (830 kg m^{-3}) firn-ice transition occurs at a depth of ∼53 m at RBIS and at ∼70 m at DIR-IC12.

2.4.3. OPTV luminosity as a proxy for core density
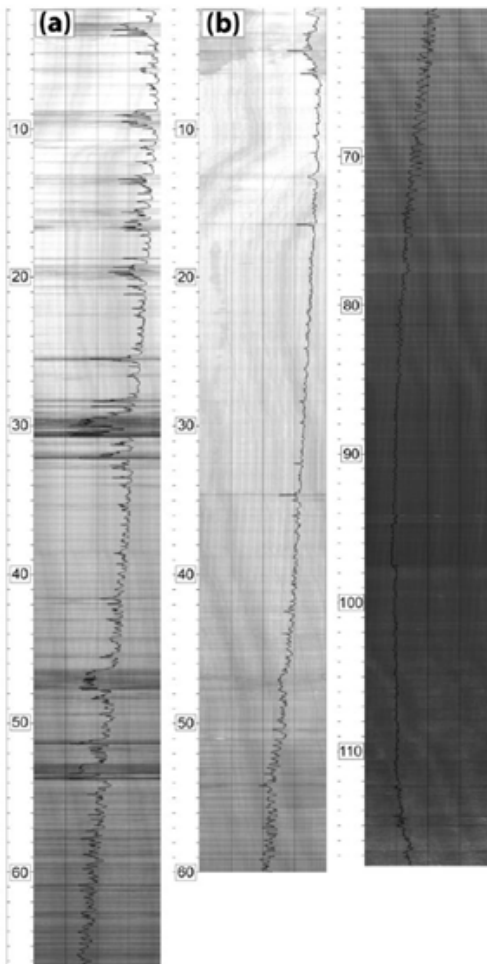
Figure 2.4.3: *Raw OPTV logs with overlaid luminosity traces (scaled 0 - 255 across the width of each log) for (a) the RBIS 2010 borehole and (b) the DIR-IC12 borehole. Note that the quasi-vertical streaks along the logs are caused by scoring of the borehole walls by drill and OPTV probe centralizers.*

Borehole-scale trend

The complete OPTV logs of the RBIS and DIR boreholes are presented in Figure 2.4.3. In accordance with previous investigations, luminosity increases slightly over the uppermost few metres with the maximum for each log located at a depth of 4.81 m at RBIS and 7.05 m at DIR. These are notably shallower than the ∼10-15 m depth recorded on e.g. the Greenland ice sheet, suggesting that grain-boundary sliding ceases sooner and at more shallow depths at the low-elevation and relatively warm Roi Baudouin Ice Shelf sites, particularly at RBIS. Below this, the luminosity trace shows a steady general decrease from ∼250 to <100 approaching the base of the deeper DIR borehole. Similar to the density measurements, this general decrease in luminosity includes a high degree of small-scale variability, particularly in the RBIS log (Figure 2.4.3a). To allow direct comparison between the OPTV luminosity data and the density data we therefore sub-sampled and averaged the OPTV luminosities over the same decimetre-length core sections as those analysed

gravimetrically for density. The resulting records reveal that, inverse to density, luminosity (L) decreases approximately exponentially with depth (d) following:

$$L = L_0 - \beta \exp(\gamma\, d) \qquad (2.4.2)$$

which, for $L_0 = 255$, yields $\beta = 21$ and $\gamma = 0.032$ ($R^2 = 0.95$) for RBIS and $\beta = 25$ and $\gamma = 0.025$ ($R^2 = 0.95$) for DIR.

Plotting gravimetrically-measured density (ρ) against OPTV luminosity (L) for the core sections analyzed (Figure 2.4.4) similarly reveals a very close match to an exponential relationship, this time of the form:
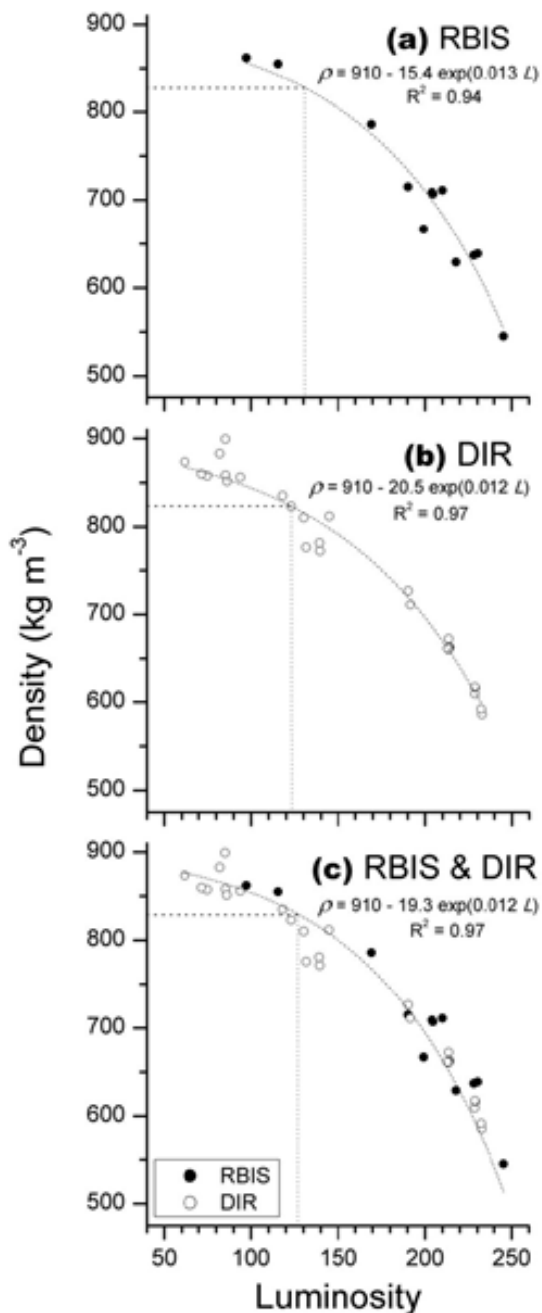
$$\rho = \rho_{ice} - \delta \exp(\varepsilon\, L) \qquad (2.4.3)$$

which yields best-fit values of $\delta = 13.4$ and $\varepsilon = 0.014$ ($R^2 = 0.94$) for RBIS 2010 (Figure 2.4.4a) and $\delta = 20.5$ and $\varepsilon = 0.012$ ($R^2 = 0.97$) for DIR-IC12 (Figure 2.4.4b). One key issue concerning the applicability of OPTV luminosity as a proxy for snow and ice density is whether a single calibration between the two variables holds universally or whether a local calibration is needed for each borehole analysed. The similarity between the best fit exponential relationships for the RBIS borehole (Figure 2.4.4a) and the DIR borehole (Figure 2.4.4b) supports the universality of the method. We evaluate this further by comparing these individual borehole regression data with those for both boreholes combined into a single data set. This comparison, shown in Figure 2.4.4c, reveals a high degree of consistency between the RBIS data and the DIR data. Combining both and fitting them to Equation 3 yields best fit values of $\delta = 19.3$ and $\varepsilon = 0.012$, with an R² value of 0.97.

The exponential relationship between density and luminosity outlined above continues for the full lengths of both boreholes, to depths well below the firn-ice transition (defined by a density of 830 kg m⁻³). This suggests that OPTV luminosity continues to provide a proxy for density at least during the early stages of ice densification by bubble closure.

Small-scale variations (10⁻³ - 10⁻¹ m)

As noted above, both borehole logs are characterized by the presence of regularly-repeated light and dark bands (Figure 2.4.3). At this low-elevation ice shelf, located at ~70° south, the lighter layers are considered to be deposited under the influence of little or no melt during the winter, and the darker layers are considered to be deposited under the influence of variable intensities of melting during the summer [Hubbard et al., 2012]. As well as these regular annual layers, numerous thicker and generally darker bands also appear in both OPTV logs, although they are far more prevalent in the RBIS log (Figure 2.4.3a) than in the DIR log (Figure 2.4.3b). These layers appear to overprint the annual layers and, for RBIS,

Figure 2.4.4: Gravimetrically-measured density plotted against OPTV luminosity for (a) the RBIS borehole, (b) the DIR borehole and (c) both boreholes combined.
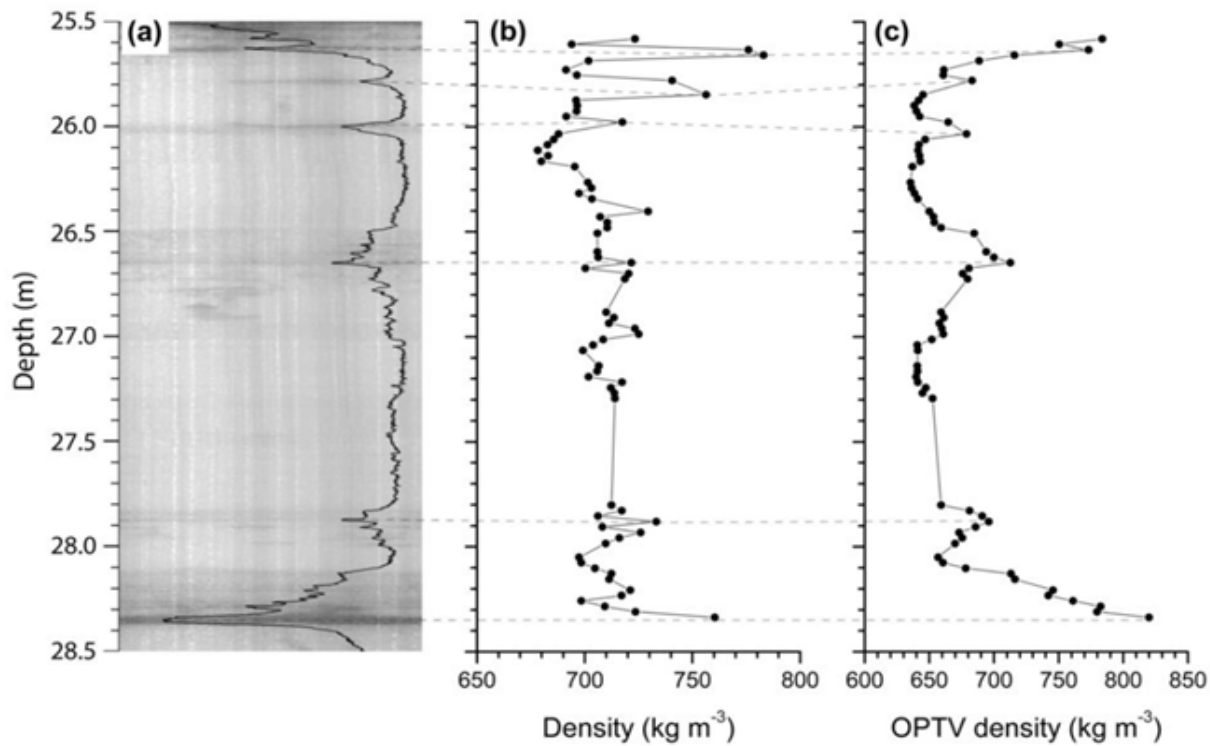
Figure 2.4.5: Expansion of RBIS data between 25.5 and 28.5 m depth: (a) raw OPTV log with overlaid luminosity trace (scaled 100 - 220 across the width of the log), (b) gravimetric density measured on ∼26 mm samples from four core sections and (c) density reconstructed from OPTV luminosity sub-sampled at the same scale as the gravimetrically measured density samples shown in (b). Superimposed dashed lines join likely ice-rich/high density layers across the three records.

were interpreted by Hubbard et al. (2012) as icy layers resulting from intense summer surface melting.

112 high-resolution gravimetrically-measured density samples from seven sections of the RBIS core are available for direct comparison with OPTV luminosity. However, for technical reasons, the depths of the two records are insufficiently well constrained to allow direct comparison at the millimeter scale without depth-matching. Depths were therefore matched for each complete core sub section by correlating gravimetric density with OPTV luminosity for each 1 mm shift over a 0.1 m window either side of the logged depth and selecting the offset with the highest correlation coefficient. The resulting comparisons all reveal that the general trends are well-matched between the two records, but that they deviate substantially in detail. This comparison is illustrated by a sequence of four separate core sections that are either contiguous or slightly offset between the depths of ∼25.5 m and ∼28.5 m (Figure 2.4.5). Here, the general decreases in luminosity at ∼25.65, 25.78, 26.00, 26.64, 27.88, and 28.36 m are all represented as darker quasi-horizontal layers in the raw log (Figure 2.4.5a) and as local increases in the gravimetrically measured density data (Figure 2.4.5b). They are also replicated in the OPTV-derived density log (Figure 2.4.5c), although this is entirely expected because these densities are reconstructed as an exponential function of the luminosity data. However, precise peaks and troughs in the gravimetrically-measured density data do not match up precisely with those in the OPTV-reconstructed density data, despite core-scale depth matching. Indeed, plotting the two density data sets against each other produces an R^2 value of 0.21. Beyond unknown errors involved in reconstructing density from OPTV luminosity, this weak match between measured density and reconstructed density at the scale of 10^{-3} - 10^{-2} m can be explained by a combination of several possible influences, considered below:

- The measured data are subject to an empirically-determined error, defined as one standard deviation in repeat samples, of up to 4%. This alone could account for a density range of

~ 55 kg m^{-3} for this data set. However, the general match between the overall gravimetric and OPTV-derived density profiles suggests that the actual error in measured density is less than this, and that this potential error is supplemented by other factors.

- OPTV-derived density is laterally-averaged at the scale of the borehole cross-section, but material density is laterally inhomogeneous at this scale. Most, if not all, of the darker sub-horizontal layers in the raw OPTV log shown in Figure 2.4.5a are not uniform around all of the borehole circumference, indicating lateral variability at the scale of millimetres to centimetres. For example, the thin dark layer at a depth of ~ 25.8 m is only present in the SE-SW quadrant of the borehole. The gravimetrically-measured density peak at this depth is noticeably more pronounced than the luminosity minimum and its associated peak in OPTV density. This particular mismatch therefore could be due to the 26 mm gravimetric sample being cut from the SE-SW quadrant of the core while the OPTV data average across the entire ~ 110 mm borehole cross-section.

- The OPTV probe records light reflected back to the probe from the borehole's walls following emission from a ring of LEDs located some centimetres above the hyperboloidal mirror. Therefore, depending on the precise reflective properties of the section of borehole wall being logged, the recorded signal may not strictly have come from the horizontal plane given by the mid-point between the LED array and mirror. Although this effect is considered to be minor, and unlikely to result in any significant offset, it could introduce some blurring of sharp layer boundaries.

- Despite depth matching at the core scale, the two data sets could still be offset, at least by some millimetres, as a consequence of imperfect depth-matching and depth control. While the latter is more likely in terms of the core sampling for gravimetric analysis, the OPTV log depth will also be subject to some error. The depth-control precision of the OPTV log is nominally ~ 0.5 mm (1000 pulses recorded per 500 mm rotation of a surface sheave wheel). However, it is possible that the actual OPTV depth recorded could deviate from the core depth as a result of cable stretch and/or borehole deviation from vertical. However, neither is likely to be significant, even at millimetric scale, at the relatively shallow depth investigated herein.

2.4.4. Density bias in the 2014 cores as a measure of transport damages and contrasts between ice shelf locations (RBIS 2010 vs. RBIS14)
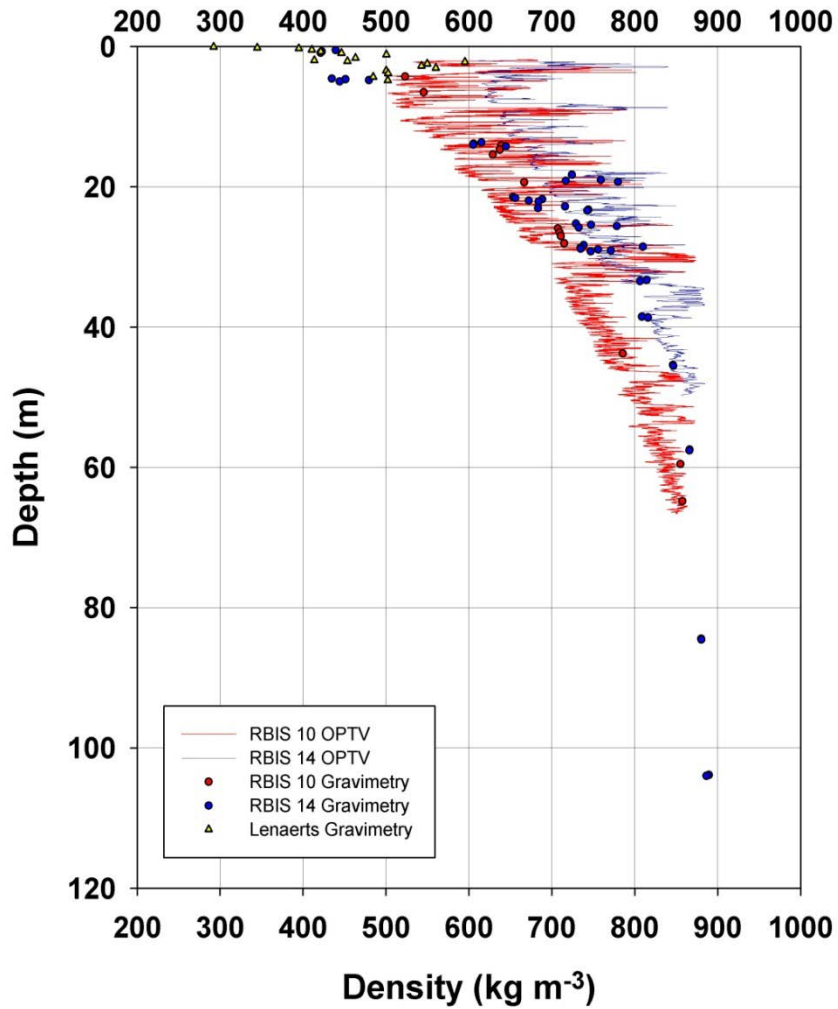
Figure 2.4.6: *Comparison of density profiles from OPTV brightness and gravimetric measurements for the 2012 and 2014 RBIS ice cores*

In order to assess damages (and therefore of the reliability of future measurements on the cores) we have performed gravimetric density measurements on a series of samples from the RBIS14 ice core. These are compared, in Figure 2.4.6, to the density records calculated from the OPTV brightness (Hubbard et al., 2013) with a double aim: a) check the concordance of OPTV and gravimetric density estimates on the RBIS14 core and judge of the reliability of using the RBIS14 profile to calibrate radar measurements in the area and b) to compare the RBIS10 and RBIS14 records to pinpoint potential contrasts in the density profiles across the ice shelf.

Clearly, the gravimetric measurements (blue dots) look coherent with the OPTV derived estimates (blue curve) for RBIS14 only from about 20-30 m depth downwards. This is in accordance with the visual observations made on the ice cores. Melting has mainly affected the density of the most porous firn, with mass loss and meltwater transfer to the bottom of the bags, where it refroze when negative temperatures were re-established (before the measurements took place). Beyond 30 meters, for densities higher than ca. 750 kg m^{-3}, the permeability of the cores became sufficiently low for the melting and refreezing processes to be only surface localized, thereby affecting less the central part of the cores that has been used for gravimetric measurements. Both types of measurements therefore concur in the less modified part of the core, giving credibility to the OPTV

curve, calculated from the brightness of the RBIS14 drill hole, but using a transfer function based on the calibration with the IC12 core.

Comparison of the RBIS10 (red) and RBIS14 (blue) curves is also of interest. It shows an important contrast in the neveification rate between the higher and lower parts of the ice shelf (the latter correspond to longitudinal surface depressions associated to under ice channels, Drews et al., 2015). Densities are clearly higher for equivalent depth in the longitudinal depressions. Visual examination of the icy layers in the OPTV record (see 2.4.3a for RBIS 2010 and 2.4.7 for RBIS14) shows larger abundance and greater thickness of individual layers at site RBIS14, also showing as higher density peaks than at RBIS10. Density records converge at ca. 60m for the two sites (which again gives credit to the use of a common brigthness-density transfer function), but the ice stage is reached much sooner at RBIS14 (ca. 45m vs. 65m at RBIS10). It is not clear yet if this firnification contrast results from more intense melting in the channel location or simply sub-surface accumulation of meltwater in the depression. Clearly no water stagnation was observed at the surface, probably due to the high permeability of the surface firn.
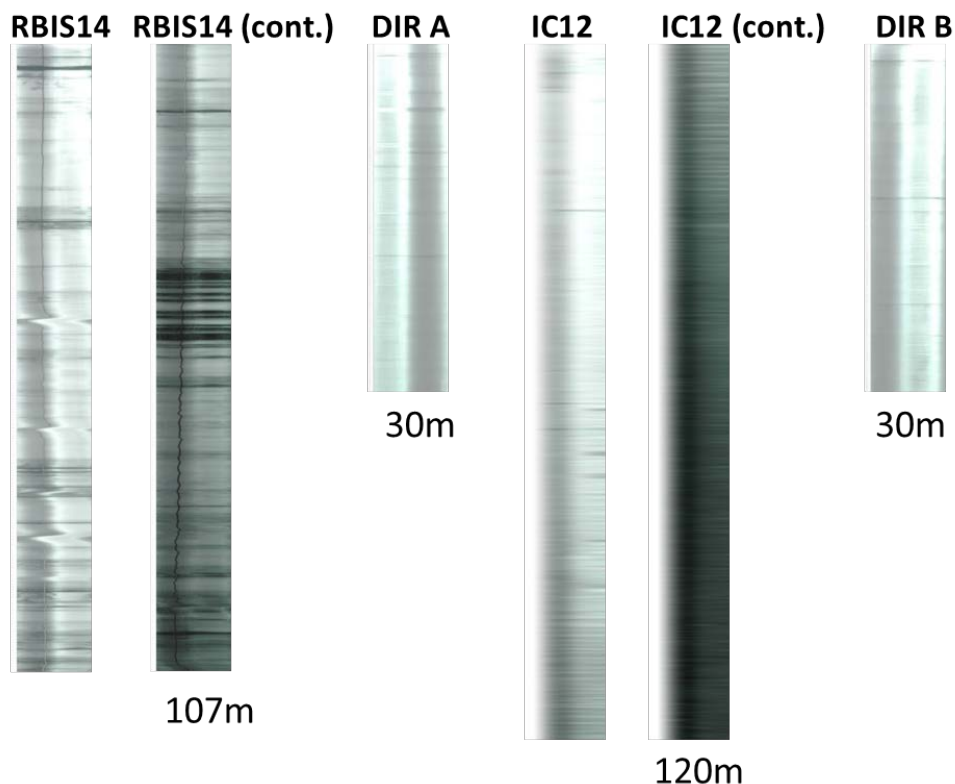
Figure 2.4.7: *Visual OPTV records from drill 2012-2014 holes: RBIS14 = Roi Baudouin Ice Shelf in longitudinal depression; IC12 = 2012 120 meters ice core at the summit of Derwael Ice Rise; DIR A = ca. 2 km downwind from IC12; DIR B = ca. 2 km upwind from IC12 – see Fig. 2.2.1 for location.*

Finally, Figure 2.4.6 also plots high resolution gravimetric density measurements in the first 4-5 meters of the RBIS14 location (about 100 meters from the drill site - personal communication from J. Lenaerts). These data show a large variability revealing the frequent occurrence of icy layers. It should be noted that the density curves deduced from the OPTV measurements tend to overestimate densities in these shallow depths, confirming the limitations we have previously described for the use of the OPTV brightness-density proxy within the first 10 meters of the drill hole (Hubbard et al., 2013).

2.4.5. Spatial variability of DIR Ice Rise density profiles from OPTV records

As described above, both 30 metres cores at DIR A and DIR B have very likely lost their scientific value, especially because they mainly consist of firn. Fortunately, OPTV profiling has been performed in the two boreholes where the cores were taken from. These are shown in Figure 2.4.7, where they look very similar. However, a detailed look at these brightness OPTV records and at the deduced density profiles (Figure 2.4.8) is already much instructive. First, comparing DIR A (downwind site) and DIR B (upwind site) shows that the density is higher in the downwind location at all depths. Also, counting ice layers with significant departure from the baseline, gives 8-9 peaks/30 m on the downwind location vs. 4-5 on the upwind location. These observations are coherent with a contrasted accumulation/erosion between both locations, wind redistribution and erosion favoring compaction and icy crusts formation (we have indeed shown previously that a fair proportion of the icy layers at the summit of Derwael (IC12) are located in the "winter" layers, with more negative $\delta^{18}O$ signature). The IC12 density profile (black curve) has more in common with the downwind location (DIR A, red curve). Note that the IC12 curve in Figures 2.4.8 and 2.4.9 is derived from the re-measured IC12 brightness curve in 2014. It thus needs to be shifted downwards (compared to the DIR A and DIR B profiles) by an amount equivalent to the snow accumulation on

Figure 2.4.8: Density profiles at DIR A (site A), DIR B (site B) and DIR-IC12. All profiles obtained from the OPTV brightness-Density proxy using equation (2) in Hubbard et al. (2013). Grey-area denotes upper 10 meters where OPTV derived densities are potentially not reliable. The DIR-IC12 curve has been shifted downwards by 2.83 m (see text for explanation).

DIR A and DIR B sites between 2012 and 2014. Unfortunately, these are currently unknown and are likely to be different from each other and from the one observed at the IC12 location (Lenaerts et al., 2014). In this first approach, we have chosen to consider equivalent 2012-2014 accumulations at all sites. We have two estimates available for this accumulation at the IC12 location: the depth of the trench drilled to recover the IC12 drill hole (2.80 m) and the cumulated GPS pole burying in 2012-2013 and 2013-2014 (1.36m + 1.50m = 2.86m; N. Bergeot, pers. comm.). The IC12 density curve in Figures 2.4.8 and 2.4.9 has therefore been shifted downwards by 2.83m.

Careful examination of the small scale density patterns (peaks, troughs, plateau and dissymmetry) in the two profiles allows us to visually correlate those patterns between the two curves (numbers in Figure 2.4.9). An interesting pattern emerges. Initially, equivalent peaks show a slightly shallower depth at the DIR A location. The features then progressively "catch-up", so that the peaks are nearly "synchronous" between 18.5 and 24 meters. This is the case for the most obvious peak at ca. 18.5 m. Below that depth range, the trend reverses. This suggests, if we consider icy layers as time-markers that the submergence vertical velocity is higher at DIR A than at IC12, which is in accordance with the "Raymond bump" evidenced by the radar measurements in the area (Drews et al., 2015). The offset is however still quite subdued, since we are only at less than 10% of the total ice thickness.

2.5. Past accumulation rates at Derwael Ice Rise

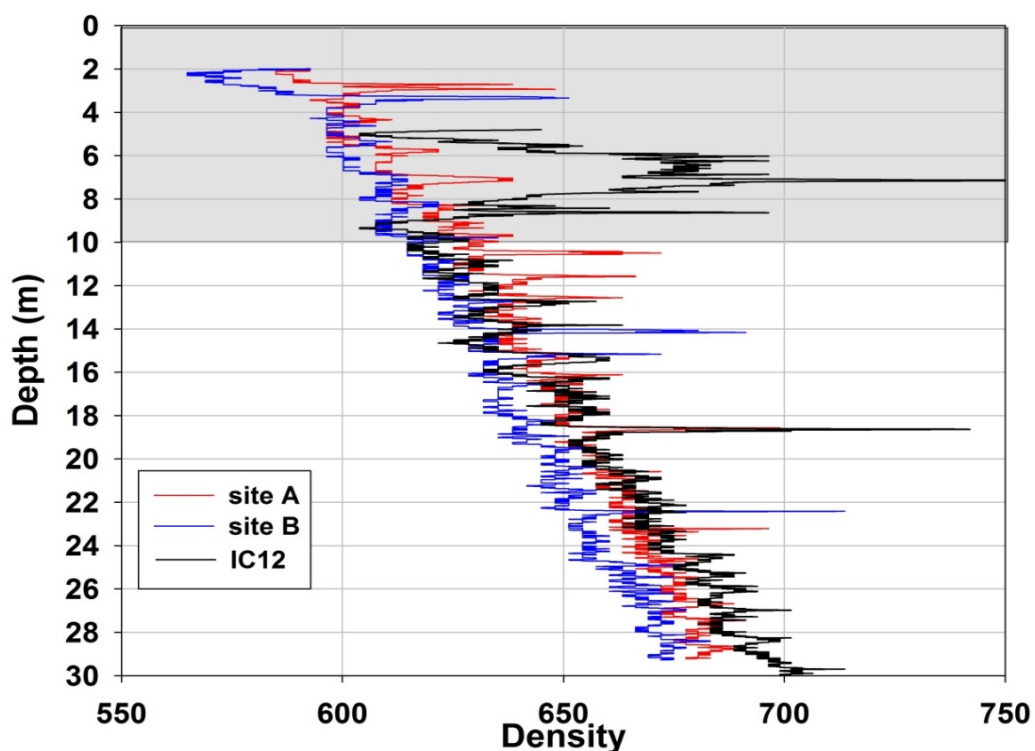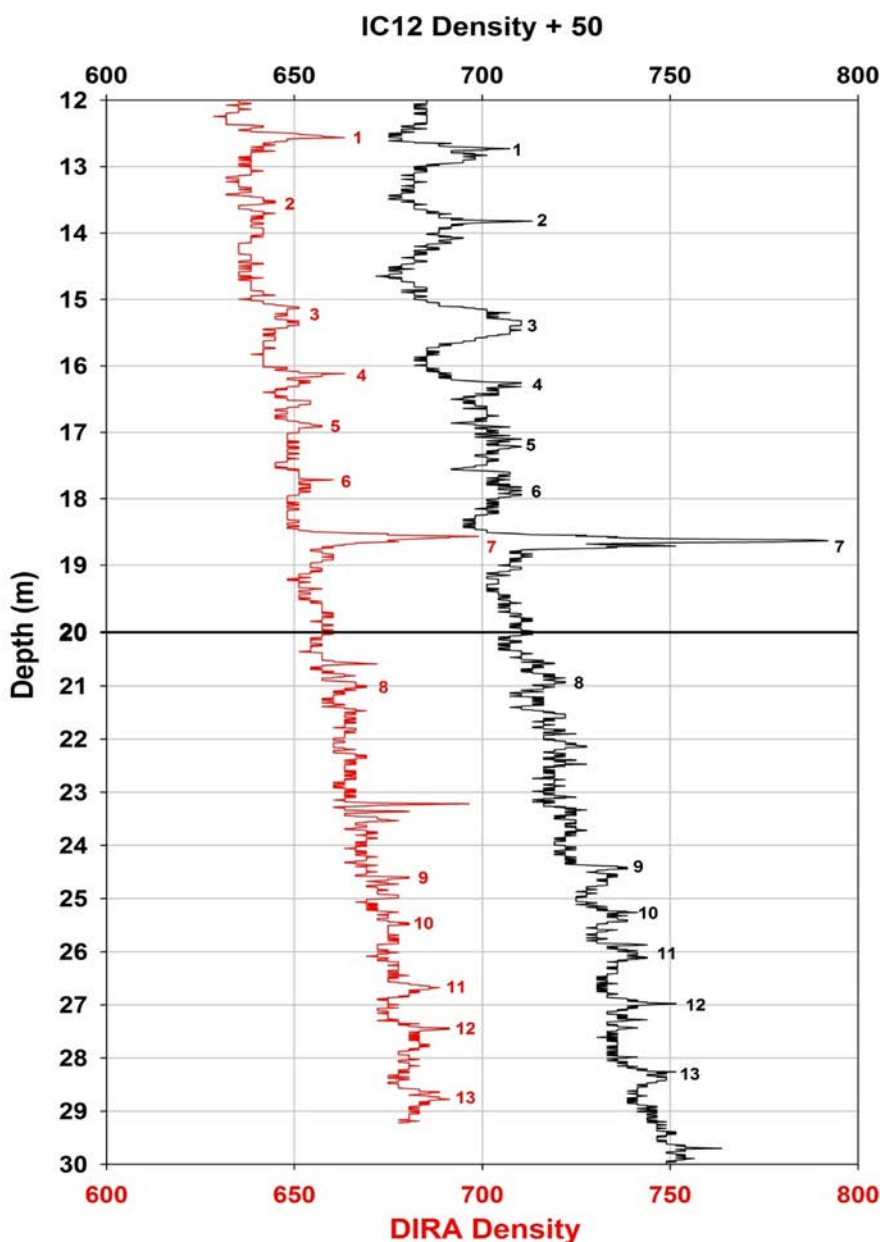*Figure 2.4.9: Density profiles at DIR A (site A) and IC12- enlargement. All profiles obtained from the OPTV brightness- Density proxy using equation (2) in Hubbard et al. (2013). The IC12 curve has been shifted downwards by 2.83 m (see text for explanations), and rightwards (by adding 50 of density) for clarity. Numbers relate to visually correlated peaks/features.*

2.5.1. The context

In a changing climate, it is important to know the surface mass balance (SMB, i.e. precipitation minus evaporation, sublimation, meltwater runoff, and/or erosion) of Earth's ice sheets as it is an essential component of their total mass balance, which directly affects sea level (Rignot et al., 2011). The average rate of Antarctic contribution to sea level rise is estimated to have increased from 0.08 [−0.10 to 0.27] mm a^{-1} for 1992–2001 to 0.40 [0.20 to 0.61] mm a^{-1} for 2002–2011, mainly due to increasing ice discharge from West Antarctica (Vaughan et al., 2013), where the present-day warming seems to be focused (Turner et al., 2005; Bromwich et al., 2014; Ludescher et al., 2015). Some studies suggested that this increase in dynamic ice loss could be partly compensated for by a warming-related increase in precipitation (e.g. Krinner et al., 2007; Palerme et al., 2016) by the end of the 21st century, but this is subject to debate. For example, Frieler et al. (2015) argued on the basis of ice core data and modelling that past Antarctic SMB was positively correlated with air temperature during glacial-interglacial changes. However, Fudge et al. (2016) found that SMB and temperature have not always been positively correlated in West Antarctica.
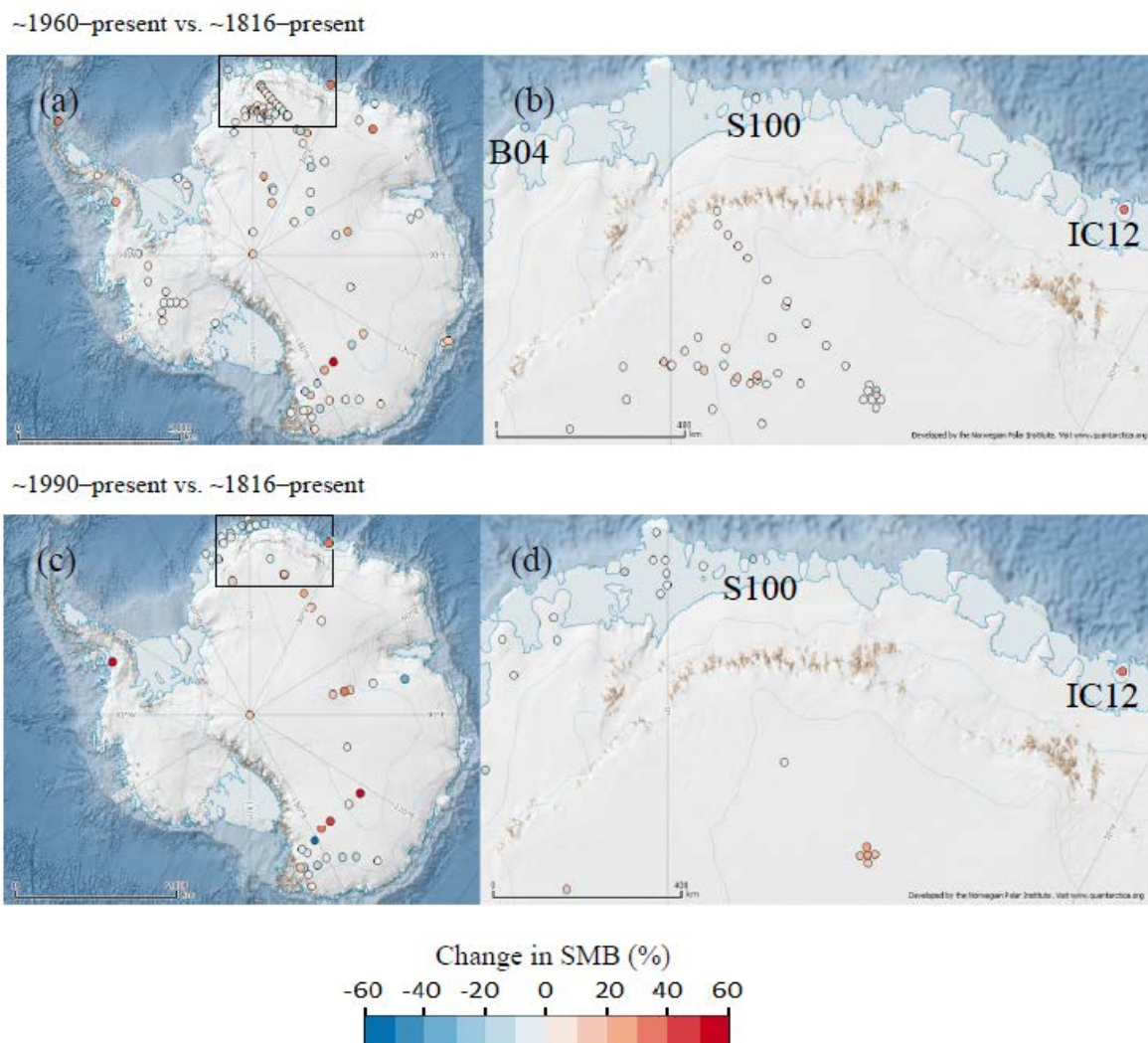
Figure 2.5.1: *Location of DIR IC12 and other ice cores referred to in this section. **(a–b)** Difference in mean annual SMB between the period ~1960- present and the period ~ 1816-present; **(c–d)** same as **(a–b)** for the period ~ 1990- present compared with ~ 1816-present. Panels **(b)** and **(d)** are expansions of the framed areas in panels **(a)** and **(c)**.*

A clear spatio-temporal pattern in Antarctic SMB change is yet to emerge. Figure 2.5.1 summarizes results of SMB trends from studies based on ice cores, stake networks, and radar. For the continent as a whole, there appears to have been no significant long-term trend in SMB over the past few decades (Nishio et al., 2002; van de Berg et al., 2006; Monaghan et al., 2006; van den Broeke et al., 2006; Bromwich et al., 2011; Lenaerts et al., 2012; Wang et al., 2016). Accordingly, 69 % of studies show < 10 % change over the last ~ 50 years relative to the last ~ 200 years. For example, Isaksson et al. (1996) found <3 % change at the EPICA drilling site (Amundsenisen) in Dronning Maud Land (DML) between 1865-1965 and 1966-1991. Considering studies comparing only the last 20 years with the last 200 years, the percentage reporting no significant trend falls from 69 to 46 %. The trends revealed over this time period are both negative and positive, although slightly in favour of the latter, with 18 % of studies showing a decrease of > 10 and 36 % showing an increase of > 10 %. These data compare with 9 and 21 % respectively of studies reporting SMB change over the past ~50 years. This analysis therefore hints at a recent increase in SMB change, whether positive or negative. Indeed, at some locations SMB change appears only to have begun ~ 20 years ago (e.g. Site M: Karlöf et al., 2005).

Regionally, East Antarctica appears to have experienced recent positive mass balance as a whole (Shepherd et al., 2012) and particularly at inland sites, e.g. at South Pole Station (Mosley-Thompson et al., 1999), Dome C (Frezzotti et al., 2005), Dome A (Ren et al., 2010; Ding et al., 2011), and DML (Moore et al., 1991; Oerter et al., 2000). However, in DML the picture is by no means clear, with some studies reporting little or no recent SMB change (Isaksson et al., 1999; Oerter et al., 1999, 2000; Hofstede et al., 2004; Fernandoy et al., 2010) and others reporting negative change, both inland (e.g. Anschütz et al., 2011) and near the coast (Kaczmarska et al., 2004: S100; Isaksson and Melvold, 2002: Site H; Isaksson et al., 1999: S20; Isaksson et al., 1996: Site E; Isaksson et al., 1999: Site M). Altnau et al. (2015) compiled DML SMB records and reported a statistically significant positive trend for the region's interior and a negative trend for the coast. In contrast, satellite data and regional climate models indicate a recent increase in precipitation in coastal East Antarctica (Davis et al., 2005; Lenaerts et al., 2012).

Similarly, King et al. (2012) estimated on the basis of glacial isostatic adjustment modelling that a 60 ± 13 Gt a^{-1} mass increase calculated for the East Antarctic Ice Sheet during the last 20 years was concentrated along its coastal regions, particularly in DML. Indeed, coastal DML appears to have experienced several high SMB years since 2009 (Boening et al., 2012; Lenaerts et al., 2013), similar to positive trends in coastal West Antarctica (Thomas et al., 2008; Aristarain et al., 2004). Such increases are supported by calibrated regional atmospheric climate models, which indicate higher SMB along coastal sectors during the period 1980–2004 (e.g. van de Berg et al., 2006). Furthermore, Wang et al. (2016) reported that climate models generally underestimate SMB in coastal DML. This is broadly consistent with the analysis of Frezzotti et al. (2013), who compared sites with low SMB (< 0.3 m water equivalent (w.e.) a^{-1}) with sites with high SMB (> 0.3 m w.e. a^{-1}), reporting that most of the high SMB sites show an increase in SMB.

It is therefore apparent that, while there is a clear need for data from all of the coastal areas of East Antarctica (IS- MASS Committee, 2004; van den Berg et al., 2006; Magand et al., 2007; Wang et al., 2016), there is particular uncertainty concerning the SMB history of the coastal region of DML. Indeed, although 17 of the records report data from ice cores drilled below 1500 m above sea level and within 100 km of the DML coast, only two of these cover a period longer than 100 years: S100 (Kaczmarska et al., 2004) and B04 (Schlosser and Oerter, 2002), both indicating a small negative trend (Fig. 1). Despite this scarcity, SMB records from such cores are valuable for several reasons, including evaluating regional climate models (e.g. Lenaerts et al., 2014), calibrating internal reflection horizons in radio-echo sounding records (e.g. Fujita et al., 2011; Kingslake et al., 2014), and validating ice sheet flow and dating models (e.g. Parennin et al., 2007). Cores from coastal regions also generally provide higher temporal resolution than from the interior because SMB generally decreases with both elevation and distance from the coast (Frezzotti et al., 2005). Near the coast, ice rises represent ideal locations for palaeoclimate studies (Matsuoka et al., 2015) because they are undisturbed by upstream topography, lateral

flow is almost negligible, and melt events are likely to be much less frequent than on ice shelves (Hubbard et al., 2013).

In this section we report water stable isotope ($\delta^{18}O$ and δD), major ion data, and continuous ECM measurements along the DIR-IC12 ice core to document accumualtion rates in the recent past. We date the core base to AD 1759 $\pm$ 16 by layer counting. After correcting for dynamic vertical thinning (see section 2.5.2), we calculate average SMB and annual SMB for the last $\sim$ 250 years, i.e. across the Anthropocene transition, and compare them with other reported trends from the region (see previous section) and to regional model outputs (see 2.5.3).

2.5.2. Methods for ice flow correction

The compression of snow under its own weight involves not only vertical density changes, but also lateral deformation of the underlying ice. Failure to take the latter process into account would result in an underestimation of reconstructed initial annual layer thickness, and therefore of the SMB, especially within the deepest and hence oldest part of the record. We explore two different models to represent vertical strain rate evolution with depth: (i) strain rates derived from a full Stokes model that represent the full Raymond effect measured at the ice divide (Drews et al., 2015), and (ii) a modified Dansgaard-Johnsen model (Dansgaard and Johnsen, 1969) based on the description given in Cuffey and Paterson (2010).

The Drews et al. (2015) strain rate profile accounts for the best fit to rada layers at depth, taking into account a small amount of surface lowering (0.03 m a^{-1}) and rheological anisotropy of the ice (run $A(n = 3)$, dH = 100, χ = 0.03 m a^{-1}, layer-depth SMB). The magnitude of applied surface lowering is small and does not alter the strain rates significantly compared to a steady-state scenario. To determine horizontal strain rates independently, we used data from eight markers located along a circle with a 2 km radius around the dome. The markers were positioned using differential GPS in 2012 and 2013 (Drews et al., 2015). The horizontal strain rates ($\dot{\varepsilon}_{xx} + \dot{\varepsilon}_{yy}$) were calculated to be 2×10^{-3} a^{-1}. Mass conservation then gives a vertical strain rate at the surface of -2×10^{-3} a^{-1}. The shape of the vertical velocity profile was then used and scaled to match this value with the long-term SMB of 0.55 m a^{-1} ice equivalent (Fig. 2.5.2).

The second model, based on Dansgaard–Johnsen (D–J), was used to fit the characteristics of the Raymond effect at the ice divide. Assuming that the horizontal velocity here is zero, the vertical velocity is maximum at the surface, given by the SMB (with negative sign), and is zero at the bed. Assuming a vertical strain rate of -2×10^{-3} a^{-1} at the surface, we can determine the kink point (between constant strain rate above and a strain rate linearly decreasing with depth below) that obeys these conditions (Cuffey and Paterson, 2010). This approach indicates that the kink point lies at 0.9 H, where H is the ice thickness. As seen in Fig. 2.5.2b, this method yields a vertical strain pattern that is consistent with that of Drews et al. (2015), especially in the first 120 m corresponding to the length of the ice core.

We calculate annual layer thickness, and consequent SMB, using vertical strain rates determined by both the Drews and the D–J methods. Annual layer thicknesses were then converted from ice equivalent to water equivalent to facilitate comparison with other studies.
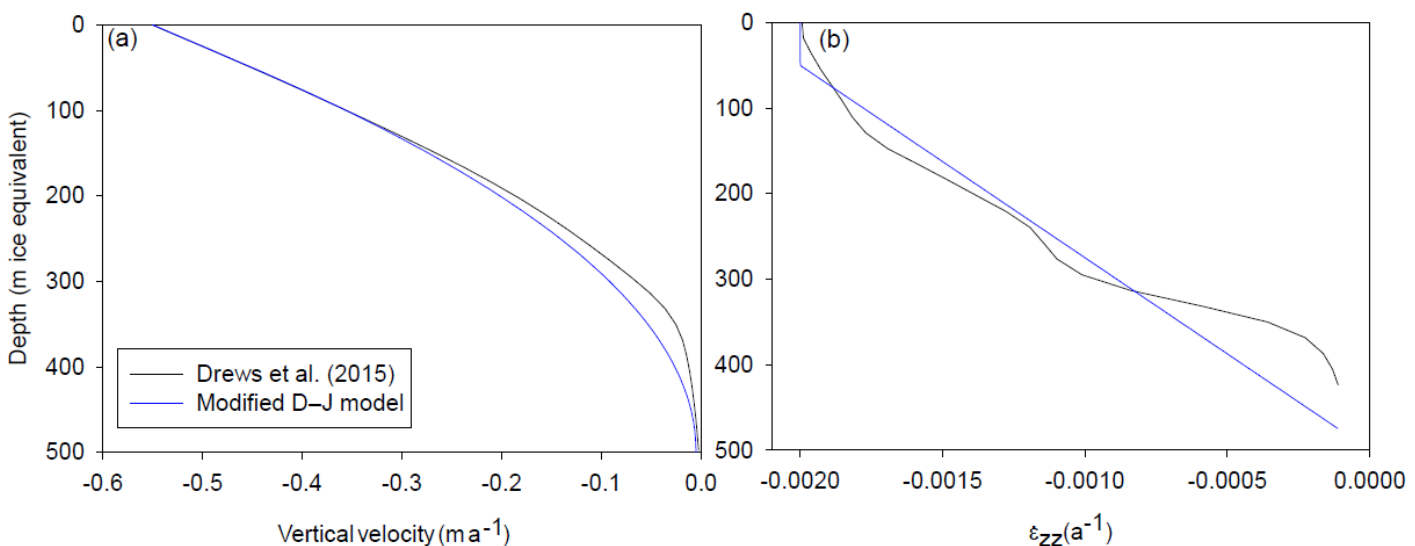
Figure 2.5.2: (a) Vertical velocity profiles and **(b)** vertical strain-rate profiles according to the modified Dansgaard–Johnsen model (blue) and the full Stokes model (black; Drews et al., 2015).
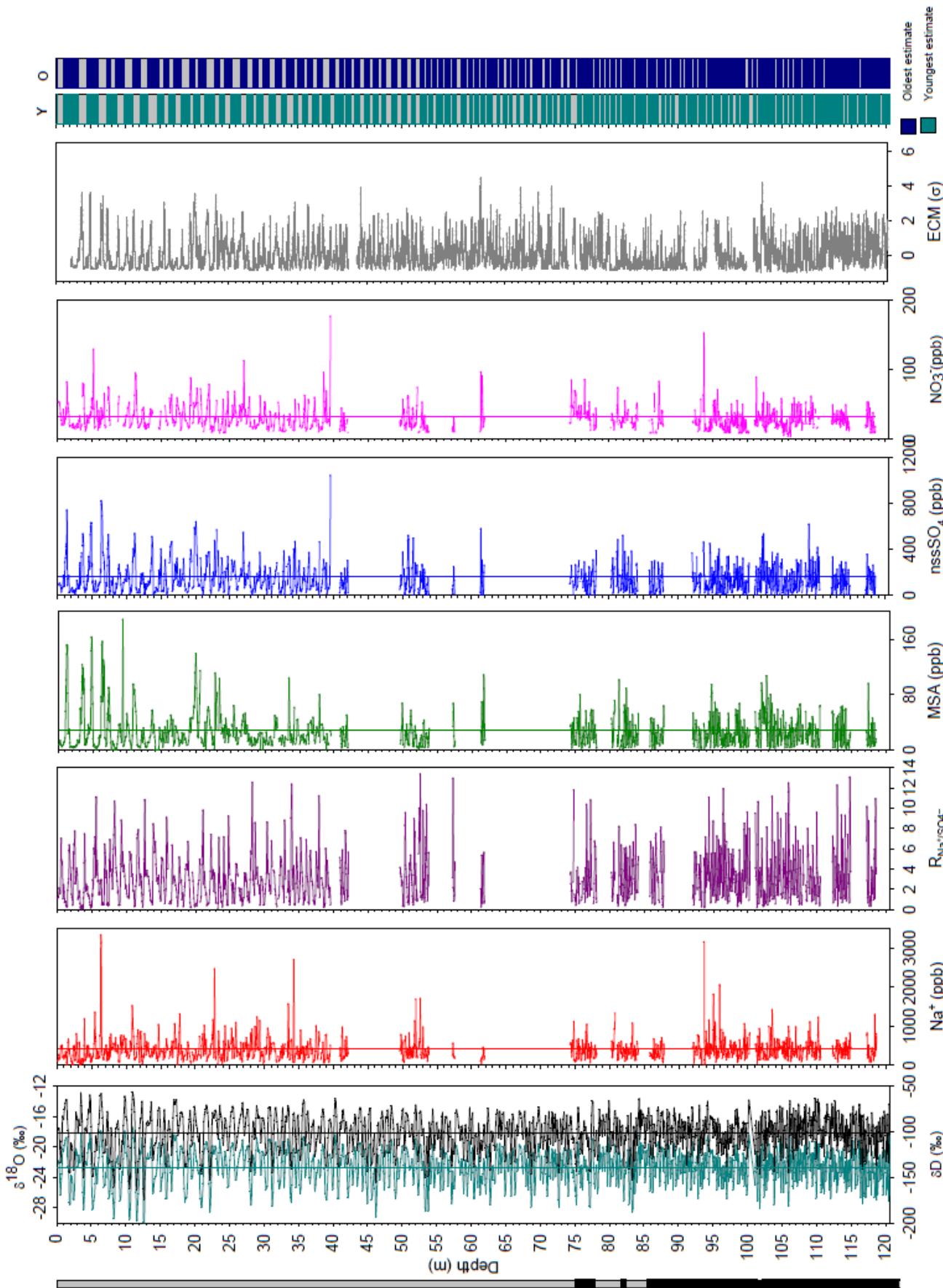
Figure 2.5.3: *Full vertical profile of water stable isotopes and chemical species at DIR-IC 12, with, from left to right: a grey and black band indicating sections of sampling for major ions at 10 cm and 5 cm resolution, respectively; water stable isotopes, taken at 5 cm resolution for the entire core; major ions, taken at 5 cm resolution for discrete sections; normalized ECM conductivity (0.05 m running mean, expressed as multiple of standard deviation, σ; annual layer boundaries in the youngest (Green) and the oldest (Blue) estimates (each colour transition indicates a boundary)*
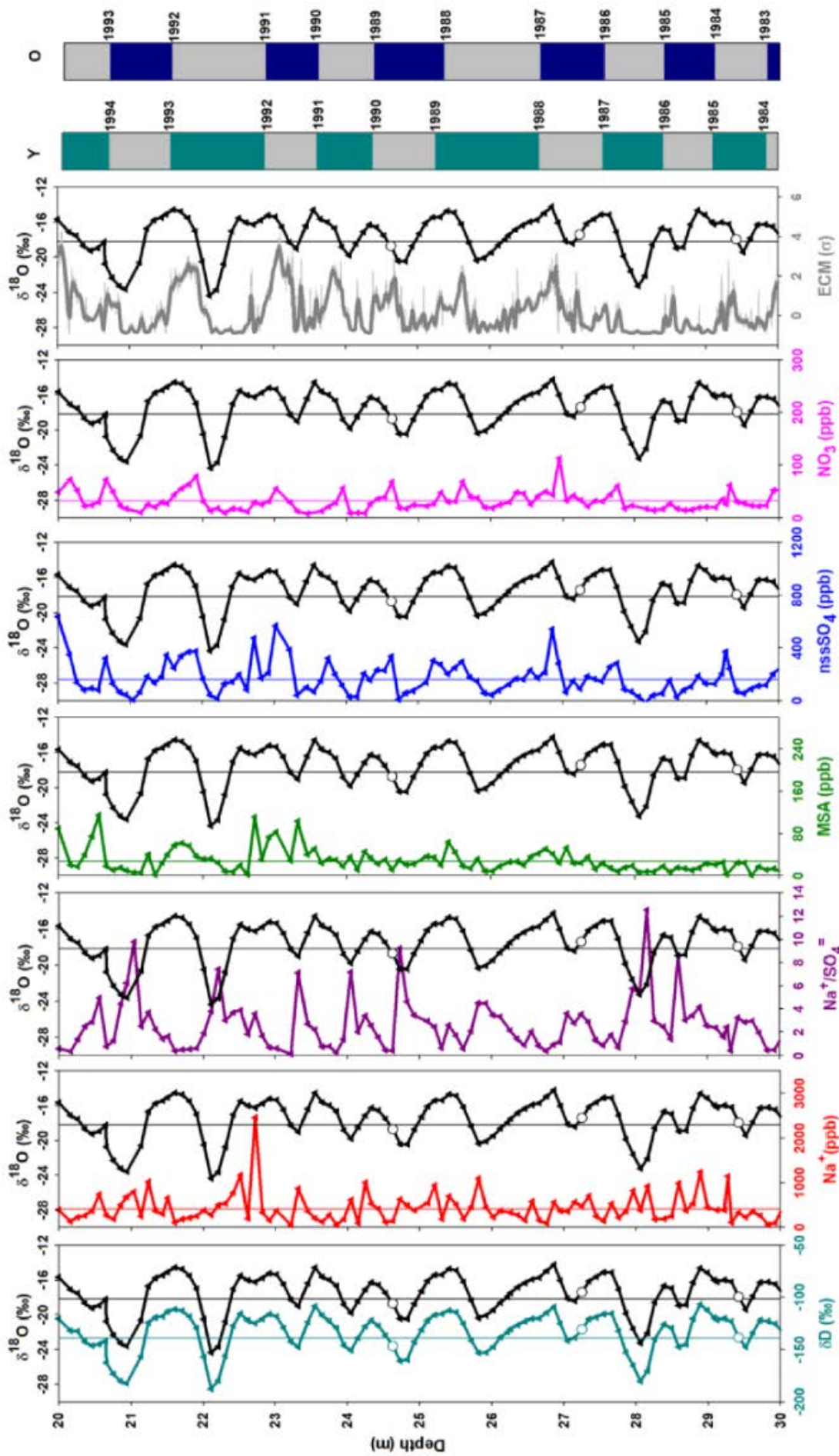
Figure 2.5.4. *A 10 m-long illustrative example of how variations in stable isotopes ($\delta^{18}O$, δD), chemical species (or their ratios), and smoothed ECM (running mean, 0.1 m) are used to identify annual layers. Coloured bars on the right indicate the annual layer boundaries (middle depth of each period corresponding to above average $\delta^{18}O$ values) for the youngest (Y) and oldest (O) estimates, with 1-year difference at 20 m depth. White dots in the $\delta^{18}O$ and δD profiles indicate thin ice layers identified visually in the core. $\delta^{18}O$ profiles are shown multiple times to better illustrate correlations between $\delta^{18}O$ and other profiles.*

2.5.3. Community Earth System Model (CESM)

Atmospheric reanalyses (ERA-Interim; Dee and Uppala, 2009) and regional climate models are compared to the ice core SMB in section 2.5.7 . These models extend back to 1979, covering only a small proportion of the ice core record.

Thus, to interpret our ice-core-derived SMB record and relate it to large-scale climate conditions, we use SMB, sea ice, and temperature output from the Community Earth System Model (CESM). CESM is a global, fully coupled, CMIP6- generation climate model with an approximate horizontal resolution of 1°, and has recently been used successfully to simulate present-day Antarctic climate and SMB (Lenaerts et al., 2016). Because CESM is not bound by observations, and is a freely evolving model that generates its own climate, the simulated SMB time series cannot be directly compared to the observed one. Instead we use a statistical approach: we use the historical time series of CESM (156 years, 1850– 2005) that overlaps with most of the ice core record, and group the 16 single years (i.e. ~ 10 %) with the highest SMB and lowest SMB in that time series. We take the mean SMB of the ice-covered CESM grid points of the coastal region around the ice core (20–30°E, 69–72°S) as a representative value. For the grouped years of highest and lowest SMB, we take the anomalies (relative to the 1850–2005 mean) in near-surface temperature and sea-ice fraction as parameters to describe the regional ocean and atmosphere conditions corresponding to these extreme years. The sea-ice extent simulated by CESM during the observational period matches observations closely (Lenaerts et al., 2016) and does not show any temporal trend in the Atlantic sector, providing confidence that the model treats sea ice realistically.

2.5.4. Dating the ice core
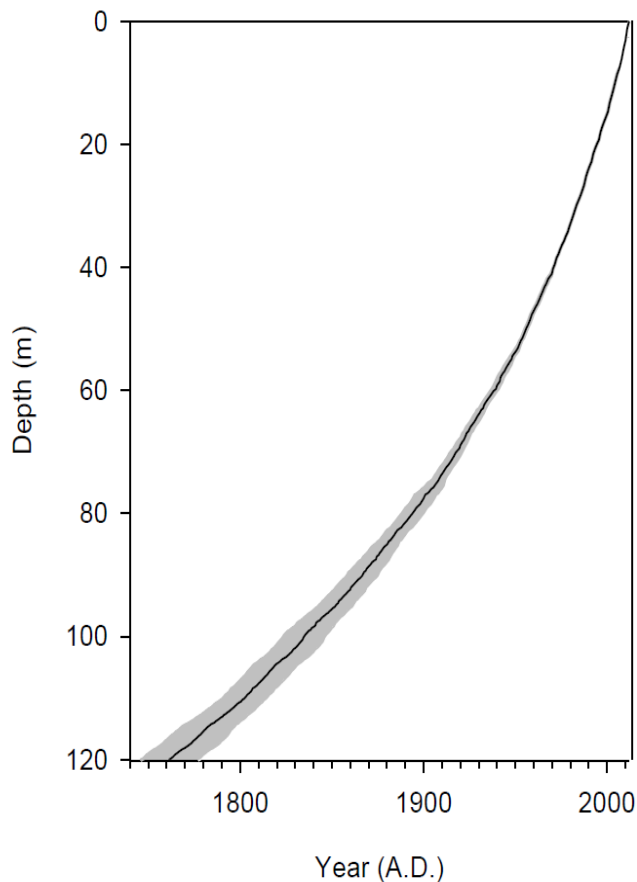
Figure 2.5.5: Age–depth relationship for DIR-IC12 reconstructed from the relative dating process. Grey shading shows the uncertainty range between the oldest and the youngest estimates. The uncertainty range reaches a maximum of ±16 years at the base of the core.

Relative dating (seasonal peak counting)

Annual layers are identified on the basis of high-resolution water stable isotopes ($\delta^{18}O$, δD), smoothed ECM, chemical species, and their ratios (Figures. 2.5.3 et 2.5.4). While all of these physico-chemical properties generally show a clear seasonality, they also change smoothly over the few very thin ice layers identified in the core (white dots in Figure 2.5.4), indicating that they are not disturbed by surface melting. The summer peak in water stable isotopes is obvious in most cases. The boundary between annual layers was identified as the middle depth of the peak above the mean $\delta^{18}O$ value (thin black line in Figure 2.5.4), considered as the "summer season". Major ions such as $nssSO_4$, NO_3^-, and especially the ratio $Na^+/SO_4^=$, generally help to distinguish ambiguous peaks in the isotopic record. $SO_4^=$ is one of the oxidation products of dimethyl sulfide (DMS), a degradation product of DMSP (dimethylsulfoniopropionate), which is synthesized by sea ice microorganisms (sympagic) as an antifreeze and osmotic regulator (e.g. Levasseur, 2013). Both $nssSO_4$ and $Na^+/SO_4^=$ vary seasonally. NO_3^- also shows a seasonal signal, but the processes controlling its seasonality are not yet fully understood (Wolff et al., 2008). For ECM, there

is also a regular seasonal signal, which is sometimes blurred below 80 m, although some seasonal cycles can still be seen, between 115 and 118 m, for example. Two extreme age-depth profiles (youngest and oldest) resulted from this counting procedure, taking the remaining ambiguities into account. The mean age-depth profile is presented in Figure 2.5.5 with the ranges associated with the two extreme age-depth estimates. Between 237 and 269 annual cycles were identified between the reference surface (November AD 2012) and the bottom of the core, which is correspondingly dated to AD 1775 and 1743 respectively, with a mean age of AD 1759 $\pm$ 16.

In the oldest estimate, each Na^+/SO_4^- can generally be associated with a $\delta^{18}O$ minimum, even in the deep parts of the record. This is the case between 101 and 110 m or between 112 and 115 m, for example, while in the youngest estimate, these years show a double peak in Na^+/SO_4^-, suggesting the latter underestimates the number of years. This age-depth range may be evaluated further on the basis of identifying volcanic signals in the core's ECM record.

Refinement of the age-depth scale on the basis of the volcanic horizons

Volcanic indicators (ECM, $nssSO_4$, SO_4^-/Na^+) can potentially be used to identify specific, dated volcanic eruptions, allowing us to reduce the uncertainties resulting from the relative dating procedure. However, the unambiguous identification of eruptions is challenging in ice cores from coastal regions, where the ECM and $nssSO_4$ background signals are commonly highly variable due to the proximity of the ocean and ocean-related MSA products. Given our preliminary relative core-based date of AD 1759 $\pm$ 16, we searched our ECM record for volcanic horizons of known ages that fell within our relative age range. The best match here is provided by our oldest age-depth scale , with the major Tambora eruption seeming to appear at 102.35 m (Fig. 2.5.6). Here, the peak in our ECM record exceeds 4σ, while an adjacent earlier peak, exceeding 2σ, may be attributed to an eruption from an unknown volcano in 1809 (Traufetter et al., 2004). Although these ECM responses are less pronounced than in other inland cores such as at West Antarctic Ice Sheet divide (Sigl et al., 2013), a 2σ threshold is commonly considered as sufficient evidence for a match to volcanic
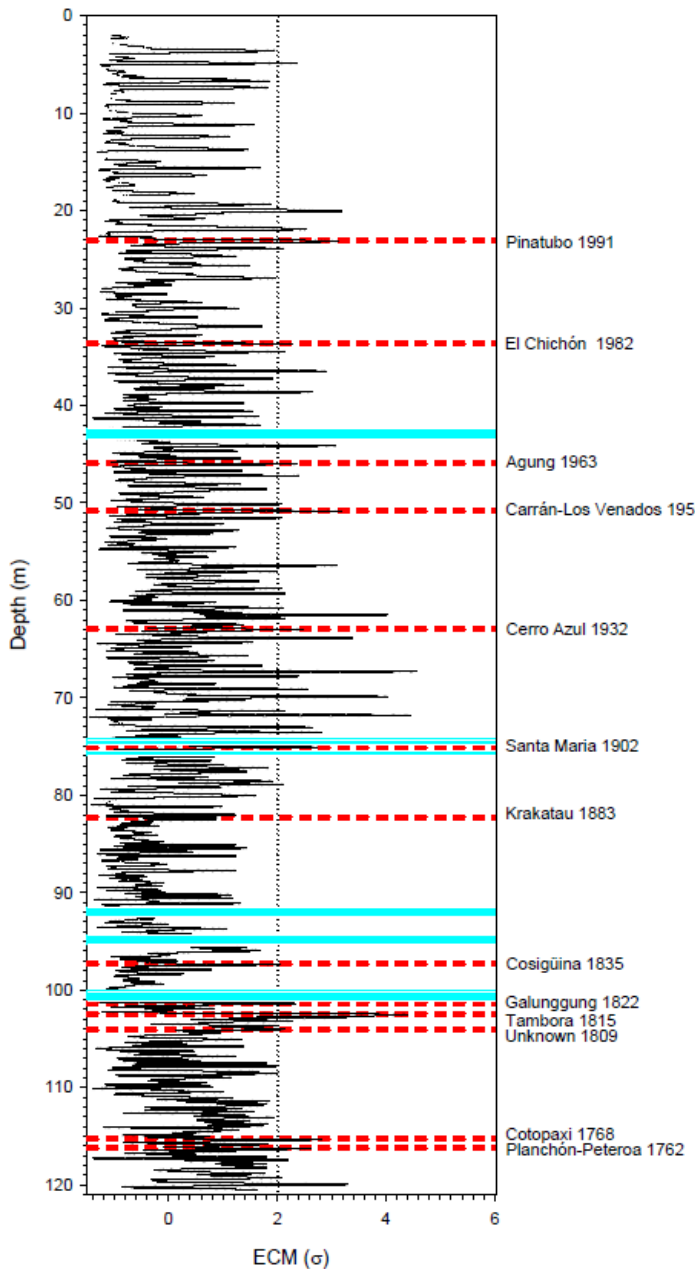

Figure 2.5.6 *Continuous record of ECM (except for six measurement gaps shown as cyan bands). Normalized conductivity (black line) is expressed as a multiple of standard deviation (σ). The 2σ threshold is shown as a dotted vertical line, and identified volcanic peaks are shown as dashed red horizontal lines.*

eruptions (e.g. Kaczmarska et al., 2004) and allows potential matching of 13 volcanoes within our record. However, several other peaks above 2σ could not be associated with any known volcanic eruption. Given this uncertainty, we conclude that the core's ECM record is too noisy for our age-depth scale to be refined with confidence by matching to volcanic eruptions. We therefore keep both estimates resulting from our layer count-based dating process, and use these as an indication of the influence of dating uncertainty on our SMB reconstruction.
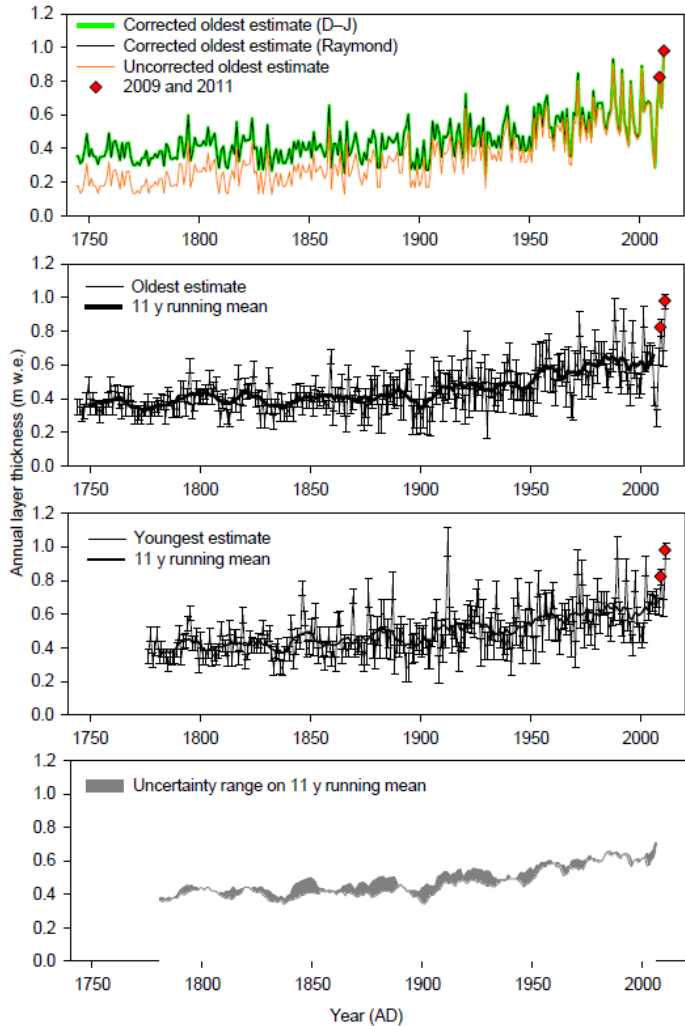
Figure 2.5.7: *Annual layer thicknesses at DIR-IC12 in m w.e. **(a)** For the oldest estimate: uncorrected annual layer thickness (orange line), corrected annual layer thickness using the full Stokes (Drews et al., 2015) model (black line), and corrected annual layer thickness with the modified Dansgaard–Johnsen model (green line, undistinguishable from the black line at this scale); **(b)** corrected annual layer thickness using Drews et al. (2015) model with error bars, showing 5-10 cm depth uncertainty (thin black line) and 11 year running mean (thick black line) for the oldest estimate; **(c)** same as **(b)** but for the youngest estimate; **(d)** range of uncertainty between youngest and oldest estimates (11 year running mean). Red diamonds highlight years 2009 and 2011, discussed in the text.*

2.5.5. Surface mass balance record

Combining annual layer thickness data with gravimetric density best fit (Hubbard et al., 2013) and thinning rate corrections, we reconstructed the SMB record at the DIR summit from AD 1759 ± 16 years to November 2012 (Figure 2.5.7). Without correction for layer thinning, the mean annual layer thickness is 0.36 ± 0.02 m w.e. This is compared with the reconstructed record of SMB including corrections for thinning, via Drews and D-J in Figure 2.5.7a. Both corrections are undistinguishable. Since the correction based on Drews et al. (2015) is more closely guided by field measurements than the modified D–J model, we henceforth consider only the record corrected by Drews. Figure 2.5.7b and c show the oldest and the youngest estimates respectively and include an 11-year running mean applied to reduce inter-annual variability. Error bars are derived from the 5–10 cm depth uncertainty on annual layer thickness, depending on the water stable isotopes resolution, and converted to m w.e. The uncertainty range drawn in Fig. 2.5.7d is bounded by the oldest and youngest estimates. The mean SMB for the whole period is 0.47 ± 0.02 m w.e., ranging between 0.26 ± 0.01 and 1 ± 0.03 m w.e. All curves also show a clear positive trend in SMB from at least the second half of the 20th century.

We define four different SMB time periods (summarized in Table 2.5.1) beginning from 1816 because of the Tambora marker (allowing comparison with other studies), and because confidence is reduced by the decreasing signal-to-noise ratio before this. As the ice core was recovered in November 2012, that incomplete year is not included in the summaries. These periods are (i) the full 195-year time period (1816 to 2011), (ii) the last 111 years relative to the previous full time period (i.e. 1900-2011 vs. 1816-1900), (iii) the last 50 years relative to the previous

full time period (i.e. 1962–2011 vs. 1816–1961), and (iv) the last 20 years relative to the previous full time period (i.e. 1992–2011 vs. 1816–1992). For the full 195-year time period (1816 to 2011), the mean SMB, including correction for layer thinning, is 0.49 ± 0.02 m w.e. a^{-1}. For the last 111 years (1900–2011), the SMB is 0.55 ± 0.02 m w.e. a^{-1}, representing a 26 ± 1 % increase compared to the previous period. For the last 50 years (1962–2011), the SMB is 0.61 ± 0.01 m w.e. a^{-1}, representing a 32 ± 4 % increase compared to the previous period. For the last 20 years (1992- 2011), the SMB is 0.64 ± 0.01 m w.e. a^{-1}, representing a 32 ± 3 % increase compared to the previous period. Detailed annual SMBs reconstructed for the last 10 years for our oldest and youngest estimates are summarized in Table 2.5.2. These records indicate recent SMB values that fall at the top end of those reconstructed throughout the period 1816–2011. For the oldest estimate, the highest SMB during the last 10 years occurred in 2011, followed by 2009. With values of 0.98 and 0.82 m w.e. a^{-1}, these fall within the 1 and 2 % highest SMB years of the whole record (∼ 250 years) respectively. For the youngest estimate, the highest SMB during the last 10 years occurred in 2011, followed closely by 2002 and 2009. With values of 0.98, 0.89, and 0.82 m w.e. a^{-1}, these fall within the 1, 2, and 3 % highest SMB years of the whole record respectively.

Period (years AD)	SMB (m w.e. a^{-1}) (oldest estimate)	SMB (m w.e. a^{-1}) (youngest estimate)	Mean SMB (m w.e. a^{-1})
1816–2011	0.476	0.513	0.495
1816–1900	0.401	0.441	0.421
1900–2011	0.532	0.568	0.550
1816–1961	0.432	0.476	0.454
1962–2011	0.604	0.623	0.614
1816–1991	0.459	0.498	0.479
1992–2011	0.626	0.651	0.638

Year (AD)	SMB (m w.e. a^{-1}) (oldest estimate)	SMB (m w.e. a^{-1}) (youngest estimate)
2011	0.980	0.980
2010	0.641	0.641
2009	0.824	0.824
2008	0.651	0.651
2007	0.287	0.699
2006	0.419	0.661
2005	0.661	0.681
2004	0.681	0.666
2003	0.666	0.621
2002	0.621	0.891

Table 2.5.1: *Mean SMB at DIR-IC12 for different time periods.*

Table 2.5.2: *SMB of the last 10 years from DIR-IC12 ice core (oldest and youngest estimates; see text for details).*

2.5.6. Sources of uncertainty

Surface mass balance reconstructed from ice cores can be characterized by substantial uncertainty (Rupper et al., 2015). The accuracy of reconstructed SMB depends on the dating accuracy, which in our case is bounded by the oldest and youngest estimates. Also, given our vertical sampling resolution of δ^{18}O, the location of summer peaks is only identifiable to a precision of 0.05 m where no other data are available. However, our multi-parameter records (Figs. 2.5.3 and 2.5.4) indicate that annual layer thickness throughout the core's full length (and particularly since ∼ 1815, the time period we focus on) is greater than our sample length, providing confidence that we are not missing annual layers that are thinner than our samples. Our belief that δ^{18}O cycles demarcate annual layers throughout the record is further supported by the one-to-one correspondence between this parameter and the Na^+/SO_4^- ratio, even in the deepest part of the core. SMB reconstructions are also influenced by density measurement error (∼ 2 % herein) and small-scale variability in densification. However, the influence of this effect on SMB is very small. For example, Callens et al. (2016) used a semi-empirical model of firn compaction (Arthern et al., 2010), adjusting parameters to fit the discrete measurements instead of using the best fit from Hubbard et al. (2013). Applying the model of Callens et al. (2016) to our data results in reconstructed SMB mean values that differ by less than 2% from our analysis based on Hubbard et al. (2013).

Vertical strain rates also represent a potential source of error. A companion paper (Philippe et al., 2016b, see section 2.6) is dedicated to a more precise assessment of this factor using repeated borehole optical televiewer stratigraphy. However, the present study uses a field-validated strain rate model and shows that using the simpler modified Dansgaard–Johnsen model changes the reconstructed SMB by a maximum of 0.001 m w.e. a^{-1}. Therefore, we are confident that refining the strain rate profile will not change our main conclusions.

Temporal variability of SMB at certain locations can also be due to the presence of surface undulations upstream (e.g. Kaspari et al., 2004), but this effect is minimized at ice divides. Another possible source of error is the potential migration of the crest. Indeed, radar layers show SMB asymmetry next to the DIR crest. Although the crest of DIR must have remained laterally stable for thousands of years or more to explain the comparatively large Raymond arches in the ice stratigraphy (Drews et al., 2013; Callens et al., 2016), we cannot exclude a recent crest migration over the last decades, particularly because the lateral offset of the SMB maximum towards the upwind side (inferred from the radar stratigraphy) remains unexplained. However, there is twofold evidence to argue against a recent divide migration: (1) a similar offset in the SMB maximum is also found on another ice rise (Drews et al., 2013), suggesting that this offset reflects a generic pattern of atmospheric deposition near the crests rather than a recent and coincidental crest migration of two ice divides and, (2) the shallow arches in the radar stratigraphy which define the lateral offset are vertically aligned and not tilted as would be expected for a migrating divide (Drews et al., 2015; Fig. 3b).

2.5.7. Comparison with models outputs
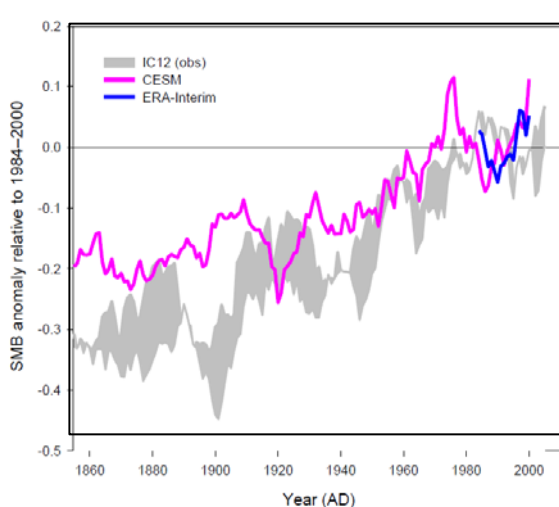
Figure 2.5.8: *Comparison of SMB trends between DIR-IC12 record, with a range between youngest (upper boundary) and oldest estimate (lower boundary) shown as grey band, CESM output (pink curve), and ERA-Interim reanalysis (blue curve). All data represent anomaly relative to 1979-1989 (black line) for the overlapping period 1850-2011.*

We compare the trend in our DIR IC12 SMB record with outputs from three atmospheric models: ERA-Interim reanalysis (Dee et al., 2009), the CESM model (Fig. 2.5.8), and RACMO2 (Lenaerts et al., 2014). ERA-Interim shows no trend in the relatively short overlapping period (1979–2012). The ice core-derived SMB correlates moderately to ERA-Interim and RACMO2, yielding coefficients of determination (r^2) of 0.36 and 0.5 respectively. For a longer period of overlap, we used the output of the CESM model, although it is a freely evolving model that does not allow a direct comparison with measured data. The CESM-derived average SMB at the closest grid point to DIR is too low (0.295 $\pm$ 0.061 m a^{-1}, 1850-2005), probably because the orographic precipitation effect is not well simulated. However, CESM does reproduce the general trend reconstructed from our DIR-IC12 core. Subtle small-scale variations in wind speed and direction, typically not resolved by reanalyses or regional climate models, might disrupt the inter-annual variability of SMB, although we assume that it does not influence the positive SMB trend found in the ice core record. Unfortunately, our method does not allow for an explicit partitioning of the SMB explained by precipitation as opposed to wind processes. Instead, we focus on the drivers of precipitation at the ice core site using the output of CESM (Fig. 2.5.9). In anomalously high SMB years, sea ice coverage is substantially lower than average (20-40 fewer days) with sea-ice cover, i.e. about 10-30 % reduction compared to the average of 120-200 days (Fig. 2.5.9) in the Southern Ocean northeast of the ice core location, which is the prevalent source region of atmospheric moisture for DIR IC12 (Lenaerts et al., 2013). This is associated with considerably higher near-surface temperatures (1-3 °C). In low SMB years (not shown) we see a reverse, but less

pronounced, signal with a higher sea ice fraction (10–20 days) and slightly lower temperatures at the oceanic source region of precipitation.

2.5.8. Spatial and Temporal variability of the surface mass balance (net accumulation rate)

Regional-scale variability

Output of the CESM shows that, along with atmospheric circulation, sea-ice cover and near-surface temperatures have an influence on precipitation at a regional scale (Fig. 2.5.9). Orography can also greatly affect SMB variability (Lenaerts et al., 2014), as can local variations in wind strength and di- rection. Indeed, the lower correlation between SMB derived from ERA-Interim and RACMO2 and the results of our study than with those from ice cores collected in West Antarctica (e.g. Medley et al., 2013; Thomas et al., 2015) may be explained by the strong influence of local wind-induced snow redistribution and sublimation on the wind-exposed ridge of the DIR (Lenaerts et al., 2014). However, both Drews et al. (2015) and Callens et al. (2016) showed that this spatial SMB pattern has been constant for the last few thousand of years. Therefore, our observed trend of increasing annual SMB in the ice core represents the temporal changes and is highly unlikely to be explained by a different orographic precipitation pattern caused by a change in local wind direction or strength. This argument, along with positive correlations with ERA-Interim and RACMO2 outputs, suggests that the trend we reconstruct at DIR is representative of at least the Roi Baudouin Ice Shelf, surrounding the DIR. More studies are however needed in the area to confirm this inference.
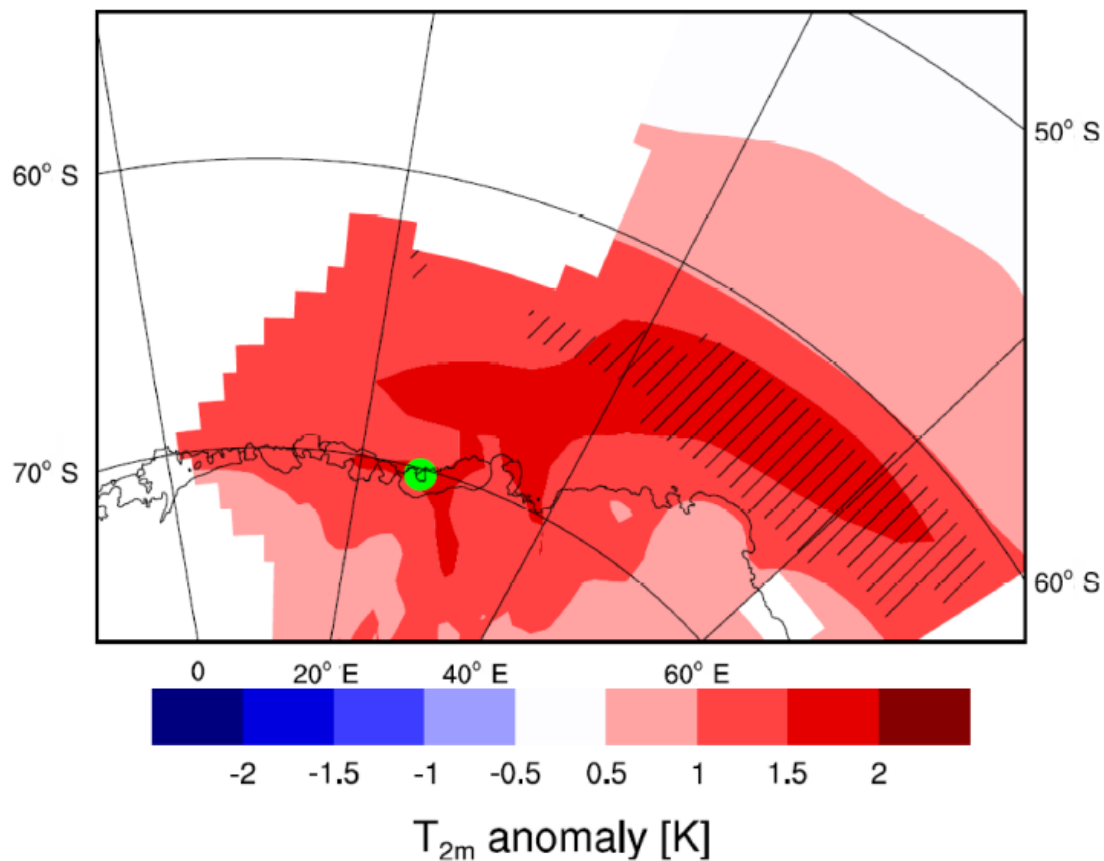

Figure 2.5.9: *Large-scale atmospheric, ocean and sea-ice anomalies in high-SMB (10 % highest) years in the CESM historical time series (1850–2005). The colours show the annual mean near-surface temperature anomaly (in °C), and the hatched areas show the anomaly in sea-ice coverage (> 20 days less sea ice cover than the mean). The green dot shows the location of the ice core.*

Continental-scale variability

Our results show generally increasing SMB on the DIR in coastal DML over the past ~ 100 years. This trend continues, and possibly accelerates, up to the present. This finding is consistent with the results of large-scale modelling and climate-based studies that also indicate a SMB increase in the area. However, until now, no increase had been detected in ice cores from the area. Our study is the first to detect in situ an increase in coastal Antarctic precipitation, which is expected to occur mainly in the peripheral areas at surface elevations below 2250 m (Krinner et al., 2007; Genthon et al., 2009).

Figure 2.5.10 shows that coastal sites (below 1500 m a.s.l. and less than 100 km from the ice shelf) do not all behave similarly. Most of the sites with high SMB (coastal or not) show an increase in SMB between the last ~50 years and the reference period (last ~200 years), whereas the sites with lower SMB show no trend, even if they are coastal (Fig. 2.5.10a). This figure also shows that only two other coastal sites can be used to compare the last ~ 200 years with the last 20 years (Gomez and S100, Fig. 2.5.10b). Comparing the last ~20 years with the last ~50 years, the increase is less visible (Fig. 2.5.10c).
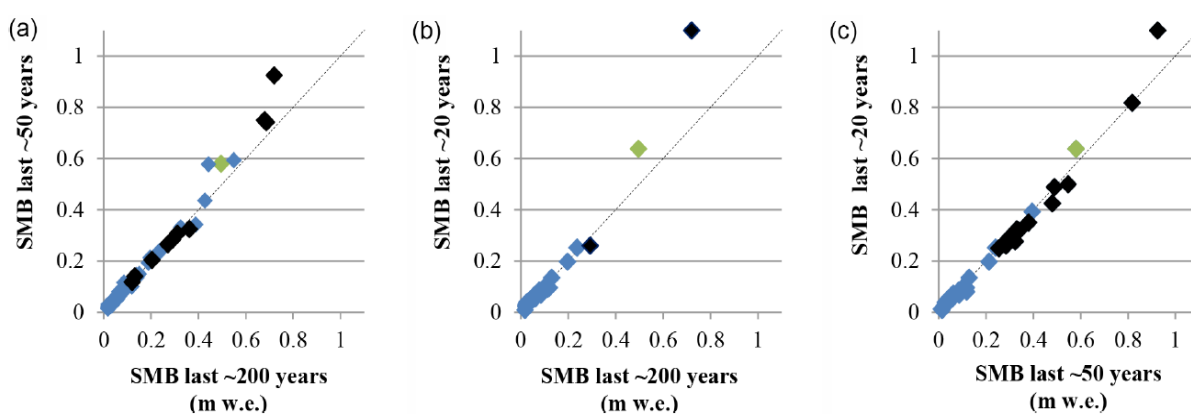
Figure 2.5.10: *Comparison of SMB between different periods reconstructed for ice cores from the continent: **(a)** the last ~200 years and the last ~50 years; **(b)** the last ~200 years and the last ~20 years; **(c)** the last ~50 years and the last ~20 years. Coastal sites (< 1500 m a.s.l. and < 100 km away from the ice shelf) are shown in black, with the exception of our study site, DIR IC12, which is shown in green. Inland sites are shown in blue. The 1:1 slope (0 % change) is shown as a dotted line.*

Causes of spatial and temporal SMB variability

The positive temporal trends and contrasts in SMB measured here and in ice cores from other areas could result from thermodynamic forcing (temperature change), dynamic forcing (change in atmospheric circulation), or both. Higher temperature induces higher saturation vapour pressure, generally enhancing precipitation. Oerter et al. (2000) demonstrated a correlation between temperature and SMB in DML. On longer timescales (glacial–interglacial), using ice cores and models, Frieler et al. (2015) found a correlation between temperature and SMB for the whole Antarctic continent. However, both Altnau et al. (2015) and Fudge et al. (2016) found that SMB and changes in ice $\delta^{18}O$ are not always correlated. They hypothesized that changes in synoptic circulation (cyclonic activity) have more influence than thermodynamics, especially at the coast. In the presence of a blocking anticyclone at subpolar latitudes, an amplified Rossby wave induces the advection of moist air (Schlosser et al., 2010; Frezzotti et al., 2013). On these rare occasions, meridional moisture transport towards the interior of DML is concentrated into atmospheric rivers. Two recent manifestations of these short-lived events, in 2009 and 2011, have led to a recent positive mass balance of the East Antarctic Ice Sheet (Shepherd et al., 2012; Boening et al., 2012). The effect was also recorded in situ, at a local scale, next to the Belgian

Princess Elisabeth base (72°S, 21°E) (Gorodetskaya et al., 2013, 2014). Several of these precipitation events in a single year can represent up to 50 % of the annual SMB away from the coast (Schlosser et al., 2010; Lenaerts et al., 2013). At the coast, precipitation is usually event-type, but the events occur throughout the whole year. However, the 2009 and 2011 events are also observed in our data as two notably higher- than-average SMB years (Table 2.5.2). Our record places these extreme events within a historical perspective. Despite the fact that higher SMB years exist in the recent part of record, 2009 and 2011 are amongst the 2-3 % highest SMB years of the last two centuries for 2009, depending on the estimate, and 1 % for 2011.

A change in climate modes could also partly explain recent changes in SMB. The Southern Annular Mode has shifted to a more positive phase during the last 50 years (Marshall, 2003). This has led to increased cyclonic activity, but also to increased wind speed and sublimation. Kaspari et al. (2004) also established a link between periods of increased SMB and sustained El Niño events (negative Southern Oscillation Index anomalies) in 1940-1942 and 1991-1995 but our record does not support this observation.

Wind ablation represents one of the largest sources of uncertainty in modelling SMB, and is an important cause of spatial and interannual variability. Highest snowfall and highest trends in predicted snowfall are expected in the escarpment zone of the continent due to orographic uplift and the associated wind erosion (Genthon et al., 2009). For example, in the escarpment area of DML, low- to medium- sized precipitation events can be entirely removed by the wind, while high-precipitation events lead to net positive SMB (Gorodetskaya et al., 2015). An increase in SMB coupled with an increased wind speed could result in increased SMB where wind speed is low and decreased SMB where wind speed is high, which is ~ 90 % of the Antarctic surface (Frezzotti et al., 2004). Accordingly, Frezzotti et al. (2013) suggested that SMB has increased at low-altitude sites and on the highest ridges due to more frequent anticyclonic blocking events, but has decreased at intermediate altitudes due to stronger wind ablation in the escarpment areas. In DML, however, Altnau et al. (2015) reported a SMB increase on the plateau (coupled to an increase in $\delta^{18}O$) and a decrease on coastal sites, which they associated with a change in cir culation patterns. Around Dome A, Ding et al. (2011) also reported an increase in SMB in the inland area and a recent decrease towards the coast. Their explanation is that air masses may transfer moisture inland more easily due to climate warming. Atmospheric circulation exhibits a primary role in deter- mining temporal and spatial SMB variability. Sea-ice and ocean surface conditions play a secondary role, and could contribute to a higher SMB in a warmer climate. A more recent study using a fully coupled climate model (Lenaerts et al., 2016) suggests that DML is the region most susceptible to an increase in snowfall in a present and future warmer climate. The snowfall increase in the coastal regions is particularly attributed to loss of sea ice cover in the southern Atlantic Ocean, which in turn enhances atmospheric moisture uptake by evaporation. This is further illustrated in Fig. 2.5.9, which suggests that extremely high SMB years are associated with low sea ice cover. The longer exposure of open water leads to higher near-surface temperatures and enhances evaporation and moisture availability for ice sheet precipitation (Lenaerts et al., 2016).

2.5.9. Conclusive remarks

Our 120 m-long ice core drilled on the summit of the DIR, has been dated back to AD 1759 $\pm$ 16 using $\delta^{18}O$, δ D, major ions, and ECM data. Due to the coastal location of the ice core, the identification of volcanic horizons in the ECM record is hampered by high background acidity. Therefore, we counted annual layers to develop oldest and youngest age-depth estimates. We combine annual layer thickness with density and thinning functions to calculate SMB time series from the core. The mean SMB for the period 1816–2011 is 0.47 $\pm$ 0.02 m w.e. a^{-1}, which increases for more recent time periods such that mean SMB for the past 20 years (1991-2011) rises by 32 $\pm$ 3 % to 0.64 $\pm$ 0.01 m w.e. a^{-1}. This supports the trend calculated by the CESM for the area. Wind redistribution is significant near the ice core location, but this effect appears to

have been temporally uniform, giving confidence that the SMB changes we report represent temporal change rather than the effects of local migration in the spatial pattern of SMB.

SMB trends observed in other records across Antarctica are spatially highly variable. In coastal East Antarctica, our study is the only one to show an increase in SMB during the past ~100 years. Many studies point to a difference in the behaviour of coastal and inland sites, due to a combination of thermodynamics and dynamic processes. A combination of spatial variability in snowfall and snow redistribution by the wind likely explains much of this observed spatial variability. Neither currently available climate models nor reanalysis data are able to resolve ice-rise topography, which makes detailed predictions from these methods difficult to match to our ice-core-derived SMB time series. Nevertheless, their temporal trends broadly match those of our reconstructed SMB, and the comparison suggests that SMB variability is governed to a large extent by atmospheric circulation and to a lesser extent by variations in sea ice cover. More studies are however clearly needed at other coastal sites in East Antarctica to determine how representative this result and our interpretations are.

Long time series of annual SMB are scarce in coastal East Antarctica. The summit of the Derwael Ice Rise represents a suitable site for deep drilling. It has a relatively high SMB, clear annual layering, and appropriate ice conditions (few thin ice layers) for paleoclimate reconstruction. According to the full Stokes model (Drews et al., 2015), drilling to 350 m could reveal at least 2000 years of a reliable climate record at high resolution, which would address one of the priority targets ("IPICS-2k array"; Steig et al., 2005) of the International Partnership in Ice Core Sciences (IPICS).

2.5.10. Data availability

Annual layer thicknesses and age–depth data are available online (doi:10.1594/PANGAEA.857574, Philippe et al., 2016a).

2.6. Present-day surface mass balance of Derwael ice rise

Ice rises are common, locally grounded parts of Antarctic ice shelves that play an important role in regulating ice-flow from the continent towards the ocean. Because they protrude out of the otherwise flat ice shelves, ice rises induce an orographic uplift of the atmospheric flow, resulting in an asymmetric distribution of the surface mass balance (SMB). We developed an original and robust method to quantify this distribution, which is essential in constraining measurements from ice cores. Combining shallow and deep radar layers, the SMB across Derwael Ice Rise is reconstructed. Two methods are employed as a function of the depth of the layers, i.e., the shallow layer approximation for the surface radar layers and an optimization technique based on an ice flow model for the deeper ones.
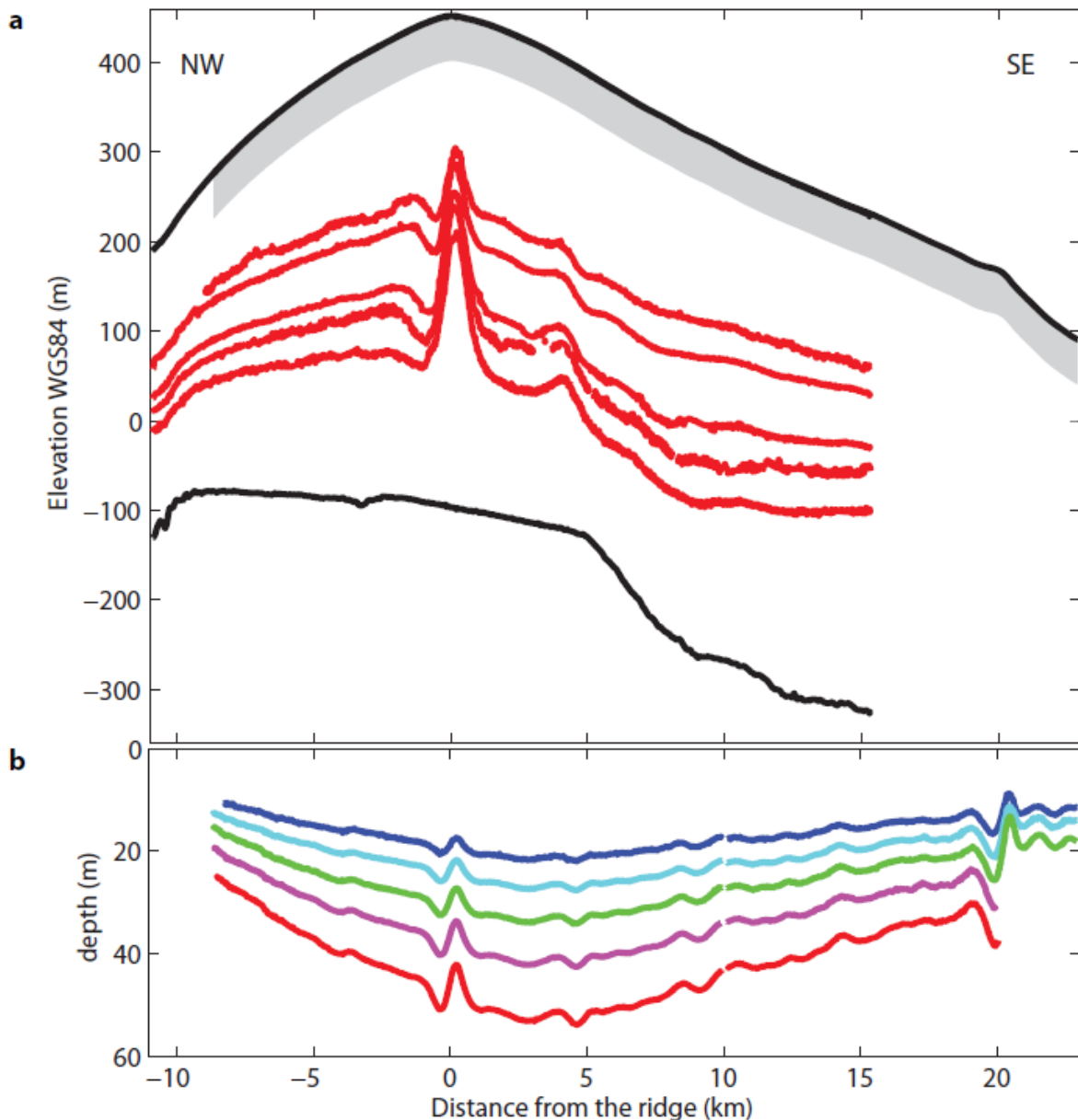

Figure 2.6.1: *(a) Geometry of the Derwael ice rise. Bed and surface are in black and layers detected with the lower frequency radar are in red. The grey zone is the detection range of the high-frequency radar. (b) Depth of the shallow layers located in the grey zone of panel (a). The small data gap situated around 10 km is the link between data from 2012 and 2013.*

The high-frequency (HF) internal reflection horizons (IRHs) were linked to a nearby firn core drilled in 2012 (Hubbard and others, 2013). This 100 m long core provides vertical profiles of temperature, density and age. The density was measured for 48 discrete samples at various depths along the core. To link the core with the IRHs of the HF profile, the two-way travel time was converted to depth using the density-depended radar-wave propagation speed parameterized by the mixing formula of Looyenga (1965). To estimate the SMB corresponding to each layer, we divide the total amount of ice between two layers by their difference in age. For the first layer, we consider the surface as a layer of age 0. The absolute values of surface accumulation derived here are inflicted with uncertainties, such as the error on the firn-core dating and errors in the density-depth model impacting both the depth determination of the IRHs and the determination of the cumulative mass above the IRHs. The uncertainty on the layer age is estimated to be 1 year (based on the layer counting method). The error on the density is defined as the root mean square difference between the density-depth model and the density samples of the firn core. The combined error on the derived SMB values is then calculated using standard error propagation.

The same profile as discussed in the previous paragraphs was also occupied with the LF system in the austral summer of 2010 (Figure 2.6.1). This radar profile shows both reflections from the bed and englacial reflectors. We used the same processing techniques as for the HF data and picked the bed together with five continuous IRHs in the LF radar data. As the deep layer geometry is
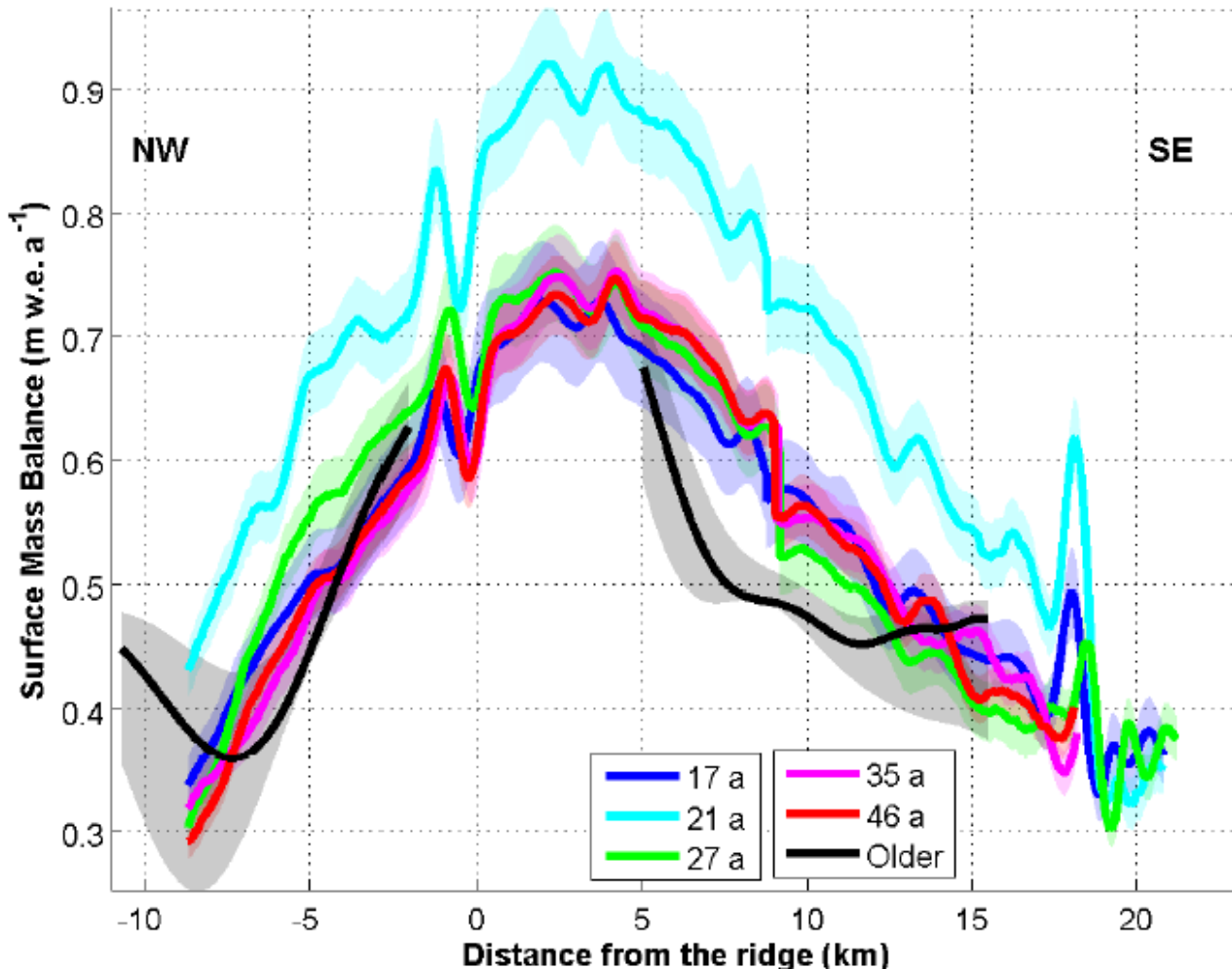
Figure 2.6.2: *Spatial distribution of the SMB across the DIR inferred from shallow and deep layers. The color code for the shallow layers is the same as in Figure 2.6.1. The shaded areas denote the confidence intervals (with respect to the error on the accumulation). The solid black line is the result of the optimization on deep layers. The grey shaded area represents the range of SMB derived while taking into account depth uncertainty.*

imprinted by the internal deformation of ice, this influence has to be accounted for prior to extracting the SMB signal. Therefore, we reconstruct the SMB by inverse modelling. The problem has two components: the forward model describing the dynamics of the ice, and the optimization scheme aiming to find the best SMB pattern for the forward model to match the internal layering from the LF data. The flank-flow regime of an ice rise is adequately captured with the Shallow-Ice approximation (SIA), which can efficiently be applied in an inversion framework. Because Drews and others (2015) established that basal ice temperature is negative (about -5°C), we prescribe that ice is frozen to the bed. Given the fact that the ice divide of Derwael Ice Rise follows a more or less straight line near the highest surface elevation, we may safely assume plain strain and model velocities along the flow line. Finally, the ice-sheet geometry is prescribed with the observed one (using the surface from GNSS and thickness from the radar-measurements) and we assume steady state (meaning that the geometry remains fixed, and we solve for the velocities without time dependence). Both the ice-flow field in flank-flow regime and the age field are solved using an Eulerian approach (Rybak and Huybrechts, 2003) with a model described in Pattyn (2010).

In the inverse procedure, we determine the SMB distribution which minimizes the difference between the depths of the observed and modelled isochrones. This problem is under-constrained as the SMB of the last millennium as well as the ages of the observed layers are unknown. To make an assumption on the age of these layers, we apply a Nye time scale in the ice-rise flanks (Haefeli, 1963) with a mean SMB (0.55 m w.e./a) to the mean depth of the layer in the region of interest. The mean layers depths range from 180 to 341 m and the corresponding ages range from 432 to 1030 years before 2012. This dating procedure was chosen because the presence of the Raymond arches prevents the use of the Nye time scale under the divide (Raymond, 1983). Even state-of-the-art full Stokes models struggle to accurately represent the magnitude of the Raymond effect on DIR (Drews and others, 2015). Given an SMB distribution $a\_(x)$, the algorithm calculates the flow and age fields providing the modelled isochrones. The minimization problem is solved with a vector-valued approach with an error vector. The first vector components are the terms of the summation and the last components are the regularisation terms. The error vector is used to compute a preconditioned conjugate gradient (computed numerically using small variations in SMB along the flowline). The subspace trust-region method based on the interior-reflective Newton method (trust-region-reflective algorithm) described by Coleman and Li (1994, 1996) then determines the modified SMB-profile for the next iteration (this step is implemented in the MATLAB function lsqnonlin). The iterations stop when the variation of the residual is below an arbitrarily small threshold.

The results of the inverse method are shown on Figure 2.6.2. The amplitude of the SMB distribution is consistent with the results inferred from shallow layers with approximately the same spatial distribution. However, we draw attention to the fact that only the relative variation can be considered since absolute values depend on the parametrisation of the depth-age scale. Nevertheless, comparison with results from shallow layers shows a good agreement between the two methods. The gradients on the downwind side (NW) are very similar while the agreement is less good on the upwind side. The gradient inferred from the inversion is more variable on this side compared to the results from HF radar.

2.7. Vertical strain-rate variations on Derwael ice rise

2.7.1. Context

Evaluating the contribution of ice caps to sea level rise requires the determination of the mass balance. The latter can be inferred by measuring the net surface submergence velocity from radar or laser altimetry. However, ice height change at the surface of ice caps is the net consequence of different components of vertical movement, i.e. snow accumulation, snow ablation, firn densification, ice deformation due to ice flow and isostatic rebound (Hamilton et al., 1998; Spikes et al., 2003). Snow accumulation and snow ablation define together the surface mass balance (SMB), which is generally measured from annual layer thickness and density measurements in ice cores (e.g. Isaksson et al., 1996) and can be extrapolated spatially using

remote sensing (e.g. Fujita et al., 2011). The measurement of firn densification requires a density profile obtained from direct measurements on the ice core or from indirect measurements of optical properties of the borehole wall (section 2.4; Hubbard et al., 2013; 2016). Ice deformation due to ice flow can therefore be deduced from the net vertical movement, considering the isostatic rebound as negligible. These parameters are crucial for the interpretation of altimetry data. In other cases, they are needed to correct annual layer thickness, improve model-based ice core chronologies, constrain ice rheology, or reconstruct age-depth relationship in firn when annual layering is not available (e.g. Hawley et al., 2002), or even infer depth-density function (Kingslake et al., 2016).

In practice, vertical strain rate profiles are scarcely available, and, in previous surface mass balance studies, provided ice deformation was taken into account, it was done via model estimates (e.g. Thomas et al., 2008). In most cases, vertical strain rate is then assumed to be constant along the full depth (Nye, 1963), or constant at shallow depth and then decreasing below a depth threshold (Dansgaard and Johnsen, 1969). However, vertical velocity profiles are non-linear, especially near ice divides and this nonlinearity can not be fully captured by any ice-flow model (Kingslake et al., 2014). Therefore, vertical strain rate should ideally be measured along the depth for correct interpretation of the ice core data.

Direct measurement of these vertical strain rates can only be done by in situ techniques such as the coffee cans method (Hamilton et al., 1998), pRES (phase-sensitive radio-echo-sounder, Kingslake et al., 2014) or borehole stratigraphy (Hawley et al., 2011). The latter technique has the advantage of being directly associated with an ice core (with validation opportunities for the density profile), but it can also be used in boreholes drilled by hot water (Hubbard et al., 2016). Of these techniques, only the pRES profile has yielded profiles of vertical movement down to the bedrock, which is therefore described in a Cartesian coordinates system. Other techniques have only measured vertical movement relative to the surface of the borehole. However, the movement of the surface can be measured by GNSS and added to the relative movement for absolute referencing, and this technique is applied here.

Here we focus on the determination of the submergence due to firn densification and ice deformation due to ice flow and the associated vertical strain rates, within the uppermost 100 m of snow, firn and ice at the crest of the Derwael Ice Rice (DIR), East Antarctica. This section reports the results of repeat borehole optical televiewing (OPTV), which has been applied to the same 120 m deep borehole in 2012 and 2014. Differencing of over 130 individual markers (ice layers) and selecting 60 of them, in order to increase precision up to 4 mm, allows vertical submergence to be calculated for each marker separated by $\sim$ 1 m. These are compared to 'coffee-can' (CCN) analysis at three discrete depths. The movement of the surface is determined with by precise geodetic GNSS measurements during three years. Vertical submergence velocities and vertical strain rates are then compared with the output of a full Stokes model (Drews et al., 2015), which has been previously used to correct annual layer thicknesses at the DIR location (section 2.5; Philippe et al., 2016).

2.7.2. Field measurements and methods

Location and "in situ" measurements

The measurements were performed at the location of the DIR-IC12 120m ice core (70°14′44.88′′S, 26°20′5.64′′E, Figure 2.2.1), located in coastal Dronning Maud land (DML), East Antarctica. This 120 m ice core, was drilled in 2012 on the divide of Derwael Ice Rise (see section 2.2). This topographic feature rises above the flat surrounding Roi Baudouin ice shelf, due to an elevation of the seabed on which the floating ice is grounded. It is 550 m thick and shows a local ice flow (Drews et al., 2015). The ice core was dated back to 1759 A.D. by annual layer stratigraphy and the mean long-term accumulation is 0.47 $\pm$ 0.02 m m ice equivalent a^{-1} showing an increasing trend since the mid-20th century to a mean value of 0.70 $\pm$0.01 m ice equivalent a^{-1} for the 1992-2011 period (see section 2.5; Philippe et al., 2016). A GNSS station was installed a few 10s of meters away from DIR-IC12 for the period end 2012 to beginning 2016 (see section 2.1). This station, anchored at 1.85 m below the surface, allowed the

estimation of the vertical movement at top of the ice rise with a few millimetres level of precision.

The 2012 borehole was logged with a borehole OPTV probe in 2012 (see section 2.2). It was then closed with a wooden plate and recovered in 2014, by digging next to it and opening up an access sideways. Density in 2014 was estimated by assuming a steady-state depth-density profile and shifting the 2014 depth by 2.82 m, corresponding to the measured depth of the snow accumulated during 2 years on top of the wooden plate.

Submergence velocity and vertical strain rate determination

In the following, we distinguish between "total" submergence and strain rate and "net" submergence and strain rate, i.e. the part of the submergence and strain rate due to ice deformation only (therefore excluding firn densification and working in "ice equivalent").

We apply two different methods to estimate submergence and vertical strain rate: the OPTV and the coffee can's method. For the first method, we consider a 10 cm error in the absolute vertical position of individual markers at time t_1 to account for eventual differential compaction caused by the weight of the wooden plate, the digging process of the access trench in 2014 or uncertainties on the density profiles. The coffee can's method is affected by a larger error (probably 20 cm), due to anchoring problems in the ice. We will therefore only use it as a comparison for the results obtained with the OPTV method. In all cases, submergence velocities are plotted at the marker depth and strain rates are plotted at the mid-layer depth, as the latter represents the strain encountered by the whole ice column above the marker.

Total submergence velocity and vertical strain rate
Relative submergence velocity of a layer n, $w_n(z_{rel})$ is calculated using Eq. 2.7.1.

$$w_n(z_{rel}) = \frac{L_n(t_0) - L_n(t_1)}{dt}$$
Eq. 2.7.1

where $L_n(t_0)$ and $L_n(t_1)$ are layer thicknesses for the same layer at time t_0 and time t_1 respectively, z_{rel} is the mean depth of layer n, relative to the surface at t_0, and dt is the time between t_0 and t_1 in years.

Each layer n is defined between the surface and a marker, following Eq. 2.7.2

$$L_n = z_s - z_n,$$
Eq. 2.7.2

Where z_s is the elevation of the surface and z_n is the elevation of the marker.

In the case of OPTV, markers are visually identified from repeat borehole stratigraphy (see below). In the coffee can's method, 3 markers are anchored at a different depth in 3 different boreholes.

This method yields a relative submergence value (in m a^{-1}) with the reference layer at the surface at t_0. To calculate the total vertical submergence, of a layer n, $(w_n(z))$ we substract this relative submergence velocity from the vertical movement of the surface measured by GNSS (see section 2.5) between time t_0 and time t_1, w_s, calculated with Eq. 2.7.3.

$$w_s = \frac{z_s(t_1) - z_s(t_0)}{dt}$$
Eq. 2.7.3

Therefore,

$$w_n(z) = \frac{[z_s(t_1) - z_s(t_0)] - [L_n(t_0) - L_n(t_1)]}{dt}$$
Eq. 2.7.4

Net submergence velocity and vertical strain rate
To calculate the change in layer thickness due to ice deformation only (excluding firn densification), we convert L_n and z_s at times t_0 and t_1 to meters ice equivalent, using the density profile measured in 2012 (t_0) and shifted by 2.82 m (measured thickness of snow accumulation) in 2014 (t_1).

Due to the error on $\rho_{(n)}$ and $\rho_{(n+1)}$, this conversion is affected by uncertainties, which would be larger than the actual deformation if the two density profiles were independent. However, we assume that the error on the 2012 density profile affects the 2014 profile in the same way and

the remaining error is therefore only due to the error on the position of the reference (surface or wooden plate) between two measurements. This 10 cm error mentioned above on marker depths is larger than the error on density.

In this case of net submergence velocity, the vertical movement of the surface is taken as 0.70 m ice equivalent a[-1], to reflect the recent increase in surface accumulation. For the model simulation, the long-term mean accumulation rate (0.55 m ice equivalent a[-1], see section 2.4 and Philippe et al., 2016) has been used.

Vertical strain rate

By definition, the vertical strain rate is the derivative of the vertical velocity along the z axis (Eq. 2.7.5).

$$\dot{\varepsilon}_{zz}(z) = \frac{dw(z)}{dz} \qquad \text{Eq. 2.7.5}$$

In this work, two approaches have been taken as to which layer thickness is considered: the "cumulated" option and the "differential" option. In the former case, each layer is defined between the surface and a marker; in the latter case, each layer is defined between two successive markers.

Cumulated strain rates are calculated between the surface and each marker n, as in Eq. 2.7.6

$$\dot{\varepsilon}_{zz,n}(z_{cum}) = \frac{L_n(t_0) - L_n(t_1)}{L_n(t_0)\, dt}, \qquad \text{Eq. 2.7.6}$$

plotted at mid-layer depth, which is half the distance between the surface and the marker, $z_{cum} = \frac{z_n - z_s}{2}$.

To avoid cumulating errors from the top layers (smallest errors) towards the bottom layers (largest errors), we also calculated the strain rate with a differential method. Instead of considering all cumulated strain between each layers and the surface, we take each layer individually and calculate the strain encountered by that layer at the corresponding mid-depth. This yields wider error bars and variability, as the thickness considered is less important, but it removes any unphysical trend that would occur if one of the top markers has encountered more strain (e.g. due to the weight of the wooden plate). It also prevents overestimating bottom layers strain rates.

Differential strain rates are calculated between two successive markers *n-1* and *n*, as in Eq. 2.7.7.

$$\dot{\varepsilon}_{zz,n}(z_{diff}) = \frac{[L_n(t_1) - L_{n-1}(t_1)] - [L_n(t_0) - L_{n-1}(t_0)]}{[L_n(t_0) - L_{n-1}(t_0)]\, dt}, \qquad \text{Eq. 2.7.7}$$

plotted at mid-depth between those two markers, $z_{diff} = z_n - \frac{L_n - L_{n-1}}{2}$

In both cases, net strain rates are calculated similarly to net submergence velocity.

Borehole optical televiewing (OPTV)

Relative vertical submergence and strain were calculated on the basis of depth differences between multiple tie points identified in the luminosity traces (defined as the mean luminosity intensity recorded around each pixel row) of both the initial 2012 OPTV log and the subsequent 2014 OPTV log.

Although the depth encoder linked to the OPTV tripod's surface sheave wheel records 9600 pulses per 400 mm rotation (yielding a precision of ∼0.04 mm), the system (particularly in 2014, see below) is additionally subject to minor operational error in recorded depth, even when comparing two logs relative to a fixed datum. While such an error is expected to be very small, even a millimetre error in depth between the two logs to be compared can represent a significant vertical strain rate at the spatial and temporal scales considered herein. In order to minimise the effect of such errors on our vertical strain calculations we define tie points between the two logs that are (i) defined by clear and sharp peaks or troughs in the luminosity trace,
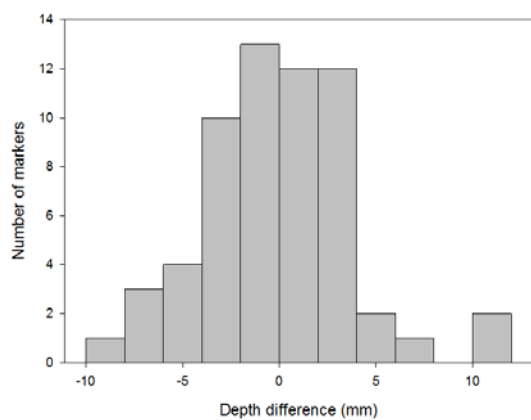
Figure 2.7.1: *Histogram of depth differences between two logs of the chosen 60 markers, repeated the same day (02/12/2014) in the same direction (up). This is used to estimate the uncertainty in the measurements (see text for details).*

thereby assisting in their precise identification, and (ii) separated by at least 1 m, thereby increasing the length over which vertical strain is measured. Applying these criteria to the luminosity traces recorded in 2012 and 2014 yielded 60 unique tie points along the full length of the borehole. Our operational error is then quantified by comparing the depths of these 60 tie-points recorded by two separate logs carried out on the same day and in the same direction. Once corrected to a common datum, this comparison yields a normal (P = 0.364) distribution of depth difference with a standard deviation of 3.78 mm (Figure 2.7.1) that does not change as a function of depth. The most likely cause of this error is wobbling in the OPTV probe as it passed along the borehole. This error has a very limited impact on submergence and strain rates determination and is well below the 10 cm error considered above.

Coffee can method

The coffee-can method (CCN) involves installing an anchor at a known depth within a borehole and recording its displacement through time relative to a fixed datum, usually at the ice surface. Changes in depth between measurement periods, in the present study between 2012 and 2013, are then expressed as an integrated function of submergence over the distance from the top of the borehole to the anchor (and plotted at the mid-point). Occasionally, it is possible for the anchor to slip, commonly evident as an unfeasibly large strain, and such data may be ignored. Two such points were found in the current study in 2013 and all data points 2014 were ignored for the same reason. Errors of 10 mm are reported to be associated with the method but here we considered a 20 cm error. Three anchors were installed in separate boreholes, each drilled within some 10s of m of the borehole logged by OPTV (above). Anchor depths were 12; 21.7; and 42.35, yielding strain mid-point data at depths of 6; 10.85 and 21.175 m.

Full-Stokes model

The full-Stokes model described in Drews et al. (2015) results from the best match with the radar layers at depth, (run A(n = 3), dH = 100, χ = 0.03 m/a, layer-depth SMB), taking into account a small amount of surface lowering (0.03 m a^{-1}) and anisotropy (although the former is not essential).
A hexagonal strain network was set up using 8 markers located along a circle with a 2 km radius around the dome. The markers were positioned using differential GPS in 2012 and 2013. The authors calculated horizontal strain rates ($\varepsilon_{xx} + \varepsilon_{yy}$) to be 0.002 a^{-1}. Mass conservation then gives a vertical strain rate at the surface of -0.002 a^{-1}. The vertical velocity profile was then scaled to match the measured vertical strain rate at the surface. Considering no vertical motion at the base, the strain profile and ice sheet model yield a mean long-term accumulation rate of 0.55 m a^{-1} ice equivalent, close to the value measured for the last 2 centuries (0.54 $\pm$ 0.02 m a^{-1} ice equivalent, Philippe et al., 2016).

GNSS 2012-2016 elevation changes

In December 2012 we installed a high precision dual-frequency GNSS receiver called ROB1 on the top of the Derwael ice rise. The daily position of the antenna, initially anchored at 1.85m depth, has been estimated using the Bernese 5.2 software (Dach et al. 2015) using state of the art approach. We analyzed GPS and GLONASS data from a global network of IGS (International GNSS Service, Dow et al, 2009) stations for the period 1995-2016 including the ROB1 observations (i.e. up to January 2016). The global network allowed to properly express the GNSS position and velocity estimates in the global ITRF2014 (Altamimi et al, 2016). The resulting daily vertical position of ROB1 is estimated with a few millimeter level precision (Figure 2.7.2). The velocity is obtained by stacking the daily solutions using CATREF (Altamimi et al, 2007) and modeling the annual signal. Three successive velocities were estimated: -139.2 +/- 0.8 cm.a^{-1}, -136.8 +/- 0.9 cm.a^{-1} and -129.8 +/- 0.6 cm.a^{-1}, for respectively 2013, 2014 and 2015 (plot of the time serie for Up component).
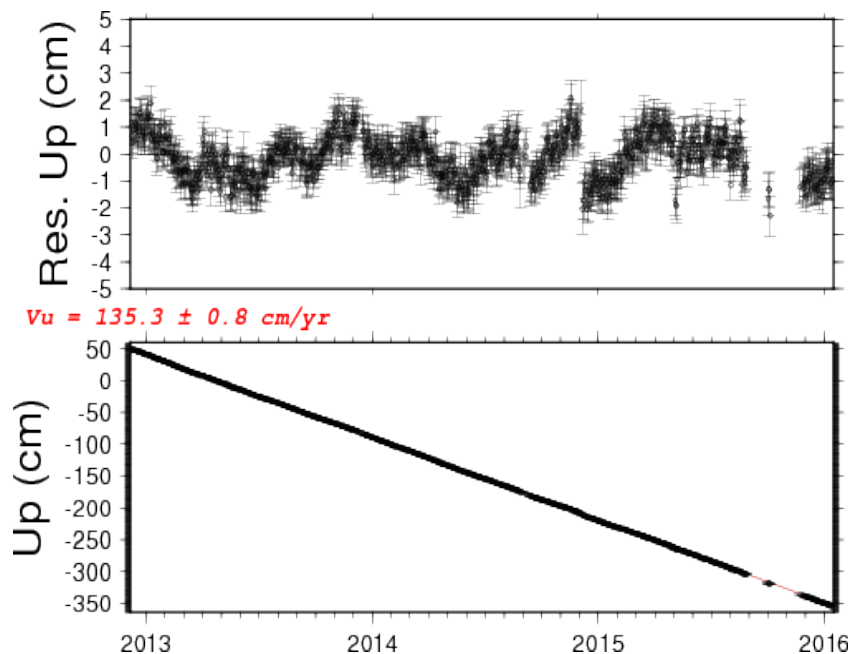
Figure 2.7.2: *Time-series of the vertical displacement estimated at ROB1 GNSS station. Bottom: Vertical displacement. Up: Position residuals with respect after removal of the linear velocity.*
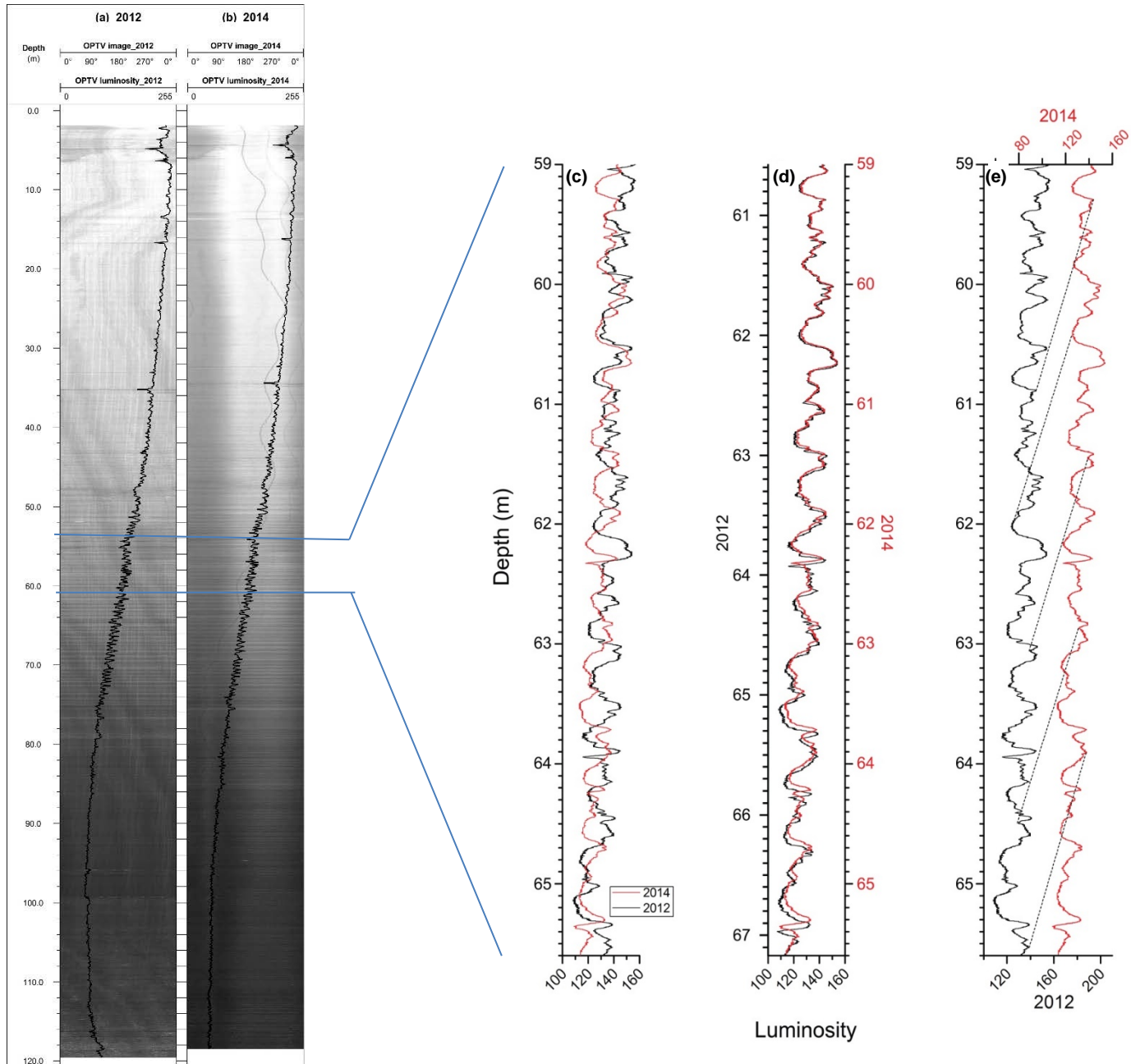
Figure 2.7.3. *Raw OPTV logs with overlaid luminosity traces for (a) the DIR borehole in 2012 and (b) the DIR borehole in 2014 (not including new snow accumulation). (c) Expansion of OPTV luminosity logs between 59.0 and 65.6 m illustrating (c) both logs (black line = 2012, red line = 2014) on the same depth scale measured from the borehole top fixed by a plate located just below the snow surface in 2012 and buried by 2.82 m of accumulation in 2014; (d) both logs with the 2012 log raised by 1.575 m (with the new depth scale plotted on the left-hand-side of the panel) to bring it into equivalence with the 2014 log at the top of the expansion at 59.0 m, and (e) both logs plotted as in panel (c) but separated laterally to illustrate five of the tie points used in the analysis. Note the offset between the two logs increases slightly down the expansion due to compressive strain rates between 2012 and 2014, particularly evident in panels (d) and (e).*
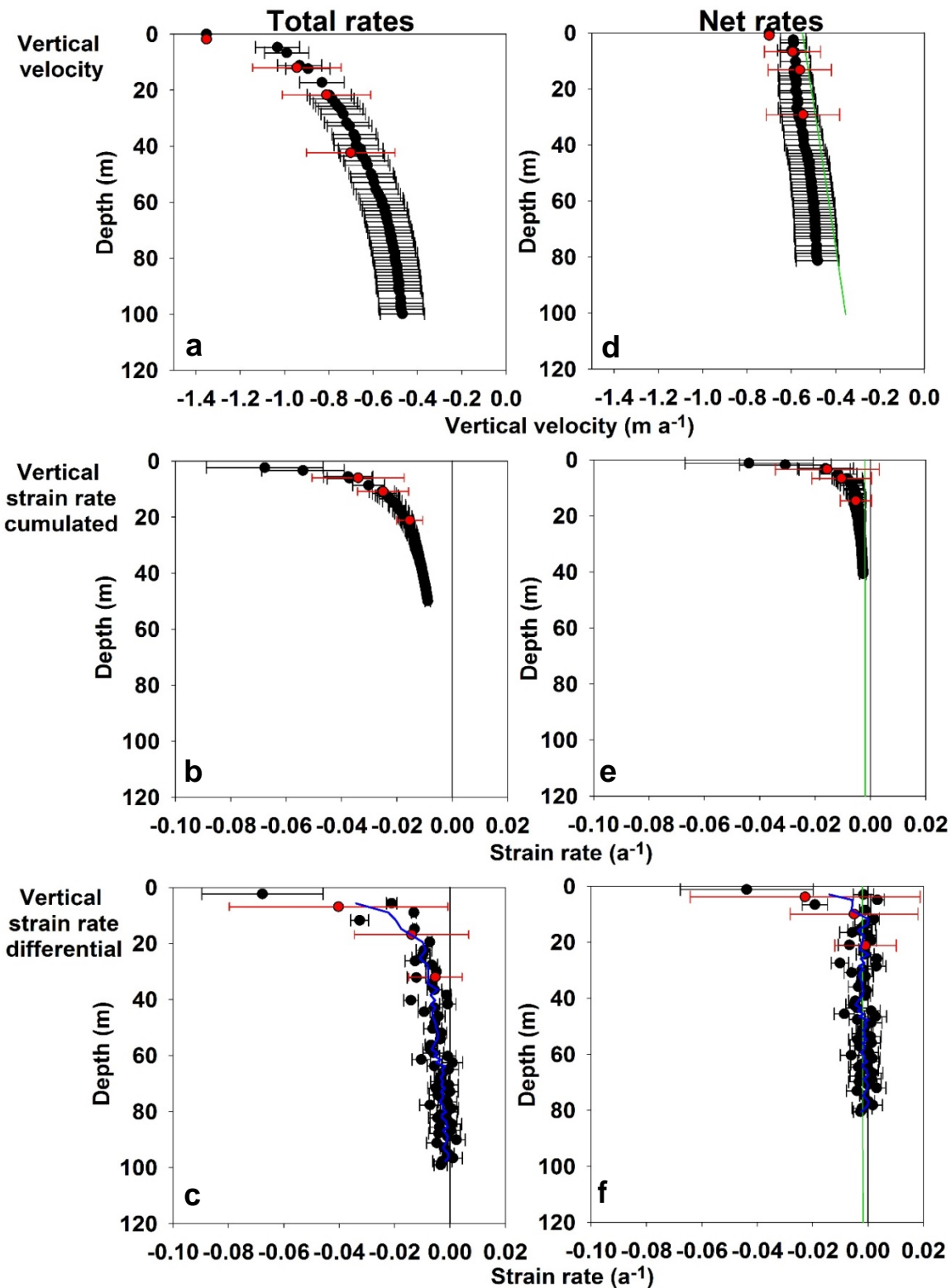
Figure 2.7.4: *Vertical velocity and compressive vertical strain rates (black dots) reconstructed from either change in spacing between 2012 surface and successive individual OPTV markers from 2012 and 2014 (cumulated) or change in spacing between two successive OPTV markers from 2012 and 2014 (differential) and from CCN markers between 2012 and 2013 (red), with associated error bars. Total rates (a to c) and Net rates (d to f) with depths in m ice equivalent) are presented in both cases. The blue line in panels c and f are 3-values running means of the differential vertical strain rates. The green lines show the results from the Full-Stokes simulation. Note that the surface submergence velocity has been taken as 1.41, 0.70 ice equivalent and 0.55 ice equivalent m a^{-1} for respectively the measured total, the measured net and the full-Stokes model velocity profiles. See text for details.*

2.7.3. OPTV results

The two logs from 2012 and 2014 (Figure 2.7.3) have the same general aspect, with a decreasing trend in luminosity with increasing depth, due to firn compaction, as described in Hubbard et al. (2013). Note that some quasi vertical streaks visible along the 2012 log are caused by scoring of the borehole walls by corer and OPTV probe centralisers (Figure 2.7.3a). In 2014, the centralisers were not used, and this results in a darker zone vertically (Figure 2.7.3b). None of these vertical features affects the present analyses since this work is focused only on the horizontal features (annual layers and melt layers). Figure 2.7.3 also shows the luminosity traces of the 2012 and 2014 logs. Mean luminosity is slightly lower in 2014 than in 2012, partly due to firn compaction that occurred during 2 years. Particular drops in luminosity are already visible at this scale (at about 5 m, 18 m and 35 m) due to transparent melt layers in an opaque firn matrix. In Figure 2.7.3 a, b and c, the top of the two logs are aligned to the initial surface of the borehole. This surface is our reference to calculate vertical movement. Therefore, the identified drops in luminosity appear more and more offset as depth increases, even if the bottom of the borehole is submitted to less movement.

As shown in Figure 2.7.3c-e, the small scale variability of the OPTV luminosity record can be efficiently used to precisely synchronize patterns between the 2012 and 2014 records. At that scale, thin ice layers are identifiable as well as regular annual variability. With the logs shifted vertically (Figure 2.7.3d), it is clear that this annual variability is well preserved during the period of 2 years, and most of the 2014 log is directly comparable to the 2012 log, down to a depth of 100 m. Tie points have been chosen as shown in Figure 2.7.3e (see figure caption for details). The depth-difference between these tie points in 2012 and the same tie points in 2016 allow us to reconstruct vertical velocities relative to the top of the drill hole: 2012 surface reference, as described in section 2.7.2). This velocity can be translated into absolute submergence velocities, knowing the surface velocity (-1.41 m a^{-1} from the GPS measurements, cf. Section 2.7.2).

2.7.4. Vertical strain rate and submergence velocity reconstruction

Total vertical strain rate and submergence velocity from OPTV and coffee can's methods

Figure 2.7.4 shows vertical velocity (a,d), cumulated vertical strain rates (b, e) and differential vertical strain rates (c, f) for both the total (firnification + ice deformation) and net (deformation only) rates. Black dots show values calculated from the OPTV markers (comparison between 2012 and 2014) and red dots, those calculated from the Coffee Cans (comparison 2012 and 2013). At the surface, the total submergence velocity is taken as -1.41 m a^{-1} (from GPS measurements) and the net submergence velocity is -0.70 m ice equivalent a^{-1} for the measurements (a combination of the mean value for the last 20 years and 0.1 m ice equivalent a^{-1} of the cover plate compaction bias) and -0.55 m ice equivalent a^{-1} for the modelled value (from long term accumulation rates). The blue line in panels c and f are 3-values running-mean of the differential vertical strain rate. The green lines in panels d to f are the model simulations.

Because deformation strain rates are small compared to firnification rates, differential vertical strain rates show more variability than the cumulated ones, due to combined errors on density and layer thickness measurements. However, part of the variability could also be associated to the higher resolution of the differential approach, capturing more accurately the heterogeneity of the medium. Also, samples along the cumulated approach profile are not, by definition, independent of each other, the surface values being recycled in all the following ones. There is, nevertheless, a very good correspondence between vertical velocities and strain rates measured by the CCN method and those measured with the OPTV. The uncertainties affecting the cumulated strain rates are smaller at higher depths, since they include movement between the surface and markers at a given depth. The deepest marker is estimated over the thickest layer and is therefore less affected by depth measurements errors.

Comparison with full-Stokes model

Net strain rate at 100 m can be estimated in two different ways: by calculating the slope of the total velocity below ~65 m (firn-ice transition), or by calculating the slope of the net vertical velocity along depth. Both methods yields a vertical strain rate of 0.0019 $\pm$ 0.0001 a^{-1}, coherent with the strain rate deduced from the surface strain network and used in the model.
Vertical velocity and strain rate profiles obtained with the full-Stokes model very well agree.
For the vertical velocity, the agreement would be even better if a higher surface velocity was considered, in accordance with recent observed accumulation changes. For the strain rates most of the discordance lie in the top tens of meters. At the surface, the net strain rate is indeed 10 times more important than the value from the model (between 0.02 and 0.07 a^{-1}) and it decreases rapidly to 0.002 a^{-1} below the first 10 m. However, the error bar on the measurements is also more important at the surface in the cumulated approach, because each strain value incorporates the strain of the upper layers, and this effect reduces the error down-profile.
This surface discordance suggests that the impact of deformation on the accumulation rate of the last decade might have been underestimated in Figure 2.5.7.

2.7.5. Discussion and concluding remarks

Vertical strain is the result of layer stretching (also called thinning) due to outward flow (a non-zero velocity component), and therefore a function of accumulation rate and thermophysics of the ice. Its value is determined by the Raymond effect, ice thickness, accumulation rate, horizontal ice flow (hence surface slopes away from the ice divide), etc. Accumulation rates define absolute value of vertical velocity close to the surface.
The variability in our reconstructed vertical strain rates is not significant, considering the uncertainty of the measurements, especially onthe density profile.
Figure 2.5.7a shows our measured density profile in 2012, with associated error bars. In figure 2.5.7b we plot, as a continuous black curve, the 2014 density at the level of each marker obtained from the 2012 density best-fit shifted 2.82 m downwards, to account for the surface depth change due to snow accumulation in two years. Dots in Figure 2.5.7b are obtained by inverting the modelled full stokes strain rate (see above) to calculate the density of each layer between successive markers in 2014 (equations 2.7.8 and 2.7.9).

$$\dot{\varepsilon}_{zz,model}(z_{diff}) = \frac{[L_n(t_1) - L_{n-1}(t_1)]\rho_{z_{diff}}(t_1) - [L_n(t_0) - L_{n-1}(t_0)]\rho_{z_{diff}}(t_0)}{[L_n(t_0) - L_{n-1}(t_0)]\rho_{z_{diff}}(t_0)\, dt} \qquad \text{eq. 2.7.8}$$

$$\rho_{z_{diff}}(t_1) = \frac{[1 + dt * \dot{\varepsilon}_{zz,model}(z_{diff})][L_n(t_0) - L_{n-1}(t_0)]\rho_{z_{diff}}(t_0)}{[L_n(t_1) - L_{n-1}(t_1)]} \qquad \text{eq. 2.7.9}$$

This clearly shows that combining a "non error bar affected" modelled epsilon with 2012 densities obtained from a best fit curve, gives 2014 density variability of the same order, if not lower, than the error bars on the measured 2012 densities. It therefore suggests that any deviation from the assumption of a steady density profile between 2012 and 2014 is enough to explain the variability in our reconstructed vertical strain rates.

Using borehole stratigraphy at Greenland Summit, Hawley and Waddington (2011) found a vertical velocity of 0.3 m a^{-1} at 30 m depth relative to the surface, which is two times slower than our measured velocity. This difference is relatively small, knowing that the ice at Summit is 3 km thick and the accumulation rate is half that of the DIR. However, the strain rate reported by Gilet-Chaulet et al. (2011) in the first 1000 m of Summit ice is 10^{-4} a^{-1}, one order of magnitude smaller than at the DIR. Arthern and Wingham (1998) found a smaller strain rate of 0.001 a^{-1} at 100 m at Site 2, Greenland.

At Taylor Dome, Hawley et al. (2002) measured a relative velocity at 100 m of 0.16 m a^{-1}, 6 times slower than our relative velocity at the same depth, although the ice thickness is similar as the DIR (~550 m). However, the snow accumulation rate is 6-9 times lower at Taylor Dome than at the DIR.

At Siple Dome, which is 1 km thick and receives 5 times less accumulation than the DIR, strain rates are smaller by one order of magnitude, i.e. 2-3 10^{-4} a^{-1} at 100 m (Pettit et al., 2011; Elsberg et al., 2004).

The strain rate found at the DIR is similar to the one measured by pRES at Berkner Island (0.002 a^{-1}) and at Roosevelt Island and Fletcher Promontory (0.001 a^{-1}) and is lower than the strain measured at Roosevelt Island (0.006 a^{-1}) and at Adelaide Island (0.02 a $^{-1}$) (Kingslake et al., 2014).

These differences in vertical movement can be attributed to three factors. First, due to is coastal location, the DIR is characterized by higher accumulation rates than other domes. High accumulation rates enhance vertical movement (Lingle and Troshina, 1998). Second, the ice thickness has an impact on the vertical movement: Thick ice domes deform much slower than small ice rises. Finally, the Raymond effect enhances surface vertical strain rates at ice divides relative to the flanks (Kingslake et al., 2014) and the borehole investigated here is located at the divide of the DIR, which shows a well pronounced Raymond Bump (Drews et al., 2015).

There is a very good correspondence between the OPTV and the coffee-cans techniques, especially for total strain rate and vertical velocity. Deducing firn compaction, the net values are slightly lower for the CCN method than for the OPTV but are within the error bars. The difference can be attributed to the use of a single depth-density profile, which corresponds to the exact location of the OPTV borehole in 2012. Although it is very unlikely that this profile changes spatially or temporally during such a short period, both techniques are very sensitive to the depth-density function. The CCN boreholes are 10s of meters distant from the OPTV borehole, and the accumulation in 2013 was most probably different from the 2014 one, therefore shifting the density profile by 1.41 m contributes to the uncertainty.

The full-Stokes model (Drews et al., 2015) agrees well with the measured vertical velocity and strain rates. There is more small-scale variability in strain rate along depth than what is expected from the model. We observe that strain rate is much higher in the top 10 meters, even if we deduce the effect of firn compaction (net strain rate). This could be due to a recent increase in accumulation rates (Philippe et al., 2016) but the errors are also the largest at the surface, which limits the interpretation of these higher value. Globally, this validates the use of this model to correct annual layer thicknesses (see section 2 and Philippe et al., 2016). Drilling to the bedrock would provide boundary conditions, necessary to reduce the error and measure the whole profile. These results will also be compared with the phase-sensitive radar available in the near-future (pRES and ApRES) (Kingslake et al., 2014; Martin et al., 2015, Nicholls et al., 2015).

In summary, previous techniques of direct measurement of the vertical movement included both densification (change of the air/ice volume) and actual ice deformation (e.g. Hawley and Waddington, 2011; Kingslake et al., 2014). Here we presented a novel method to quantify net movement, independently from any modeling approach. Theoretically, the OPTV technique should be capable of capturing very small-scale variability using luminosity as a proxy for density (Hubbard et al., 2013; 2016). However, the method for reconstructing density still needs to be refined at that scale. If the technique is improved, it could even be capable of identifying annual layers from seasonal variations in luminosity (Hubbard and Malone, 2013) and correct individual annual layer thicknesses with measured strain rate at annual resolution. These future efforts could also help deciphering the variability in deformation rates, e.g. in the presence of melt layers.

2.8. Kinematic GNSS and radar measurements

During the first two campaigns, kinematic GNSS surveys were made to retrieve the surface topography. Markers were installed in 2012 and revisited in 2013 to derive ice-flow velocities. Deep- and shallow-sounding radar profiles were done in 2010 and 2012; the former were used to determine bed topography and englacial structures, the latter to estimate and approximate surface

mass balance. Ice-flow models were constrained using these field data in order to examine the evolution of the ice rise.

We conducted kinematic GNSS surveys to determine the surface topography and positions of radar profiles, and rapid-static GNSS surveys to determine ice flow. Satellite-derived surface topography is not accurate enough over many ice rises (Drews et al., 2009; Wesche et al. 2009), and surface velocities over ice rises are too small to be detected by satellites in many cases.

In 2012 and 2013, GNSS data were collected with Trimble L1L2 receivers at one second intervals, simultaneously with a fixed base station at the summit. The global coordinates of the base station were fixed using static precise point positioning, the data of the remaining receivers were post-processed differentially using the GAMIT, GLOBK/TRACK v.10.5 software package (Herring et al. 2013). In 2010, kinematic GNSS data were collected at one second intervals using Leica's L1 receivers. The data were processed using the kinematic precise point positioning from the Canadian Geodetic survey.

Mean and standard deviation for internal cross-overs from the 2010 and 2012 surveys are 0.2 ± 1.3 m and 0.0 ± 0.1 m, respectively. The lower deviations for the 2012 data reflect the more advance processing with the dual phase receivers. External cross-over errors for the topographic profiles in 2010 and 2012 are 0.1 ± 2.6 m. The latter are likely linked to differences in the global solutions of the precise point positioning of the different years, and also at least partly reflect the inter-annual variability in surface elevation.

For static measurements in 2012 and 2013, twelve 3 m long conduits were installed in a 2 km radius around the dome and along the central radar profile (A-A', Figure 2.8.1). The GPS antennas were mounted on top of the conduits, and occupied for at least 30 minutes. The processing included GPS dual frequency observables, precise GPS orbits, absolute phase center corrections for the ground and satellites antennas, tropospheric refraction modeling (and estimation) as well as ocean loading and earth tides (e.g. Bergeot et al. 2009). The static processing was done in two steps. First, the daily coordinates of the base station were estimated from 24 hour data using the Precise Point Positioning Atomium software (Defraigne et al. 2008). The resulting position is at 2 cm precision (3 sigma). Second, we estimated every baseline length in a network approach with fixed base station coordinates (the daily motion of the base station is within millimeters and therefore negligible). The resulting positions for the 12 markers are estimated with a mean precision of 0.8 and 4.3 cm for the East and North components, leading to processing uncertainty on the velocities of ~5 cm/a (3 sigma). Errors reported above are purely from the GPS analysis, and do not include errors associated with tilts of the markers. Nevertheless, velocities along the center line range between 2-14 m/a and the observed tilts were small, therefore we considered these less-well constrained uncertainties negligible and use the data for comparison with an ice-flow model in section.
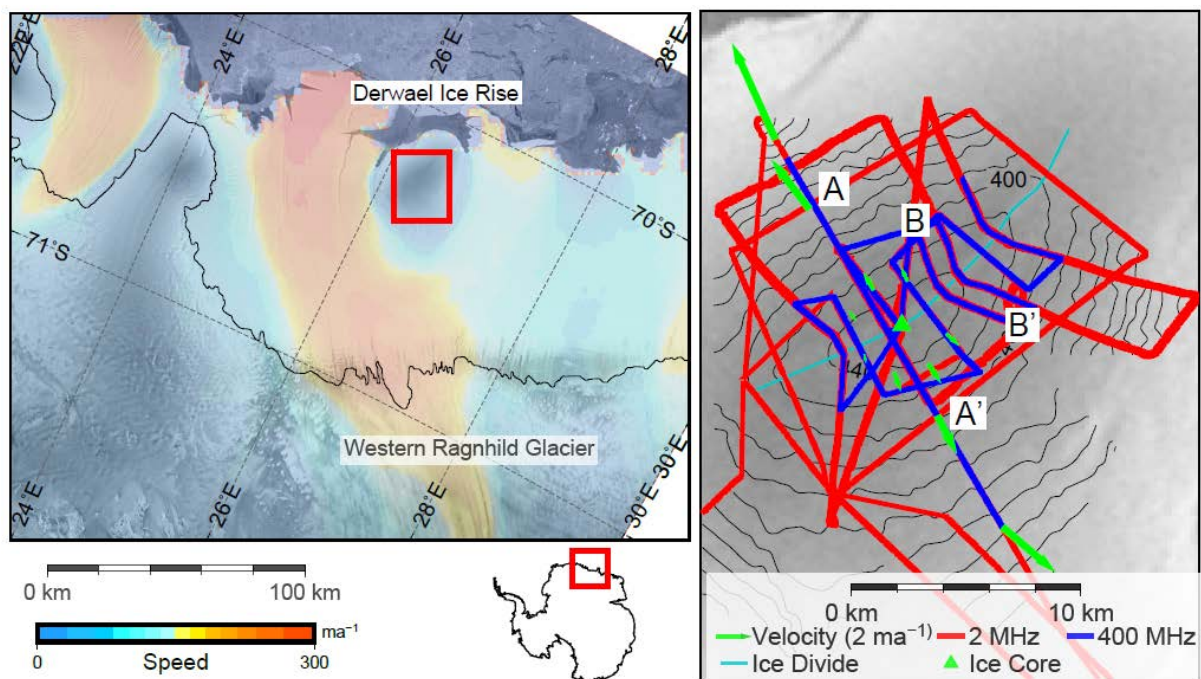
Figure 2.8.1: *Derwael Ice Rise in the Roi Baudoin Ice shelf. (a) Ice-flow speed (Rignot et al. 2011) illustrates that the ice rise deviates the flow from the western Ragnhild glacier, one of the biggest outlet glaciers in Dronning Maud Land (Callens et al. 2014). Background image was taken from the Radarsat Mosaic (Jezek et al. 2002), the grounding line in black from Bindschadler et al. (2011). (b) Radar-profile locations, ice velocity, surface topography (20 m contours, meters above WGS84), and ice-core site in our study area. Data along B-B' is shown in Figure 3.8. Ice-flow modeling was made along the flow line A-A' through the summit.*

A 400 MHz ground-penetrating radar (GSSI:SIR 3000) imaged the upper ∼50 m of the firn column. We use the changing depth of internal radar layers as proxy for variations in surface mass balance (SMB). We assume that traced layers are isochronous, and that the layer depth is only a function of the local SMB and not a function of ice flow (shallow layer approximation; Waddington et al. 2007). To keep this limitation in mind, we refer to the radar derived SMB as layer-depth SMB.

In order to convert the measured two-way travel time to depth, we parameterize the wave propagation speed as a function of firn density using the mixing formula given by Looyenga (1965). The depth–density scale is based on discrete density measurements taken on an ice core located at the center of the survey grid (Hubbard et al. 2013). To approximate the density profile between the core samples, we used a semi-empirical compaction model (Arthern et al. 2010). The model was fitted to the measurements, assuming a steady-state densification, and using the activation energy for grain growth (Cuffey and Paterson, 2010). Lateral variations in density are neglected.

The englacial radar layers are dated by linking the layer depth to the tentative ice core's age-depth scale (based on $\delta^{18}O$ measurements). The ice equivalent depth of the radar reflector divided by the layer age results in the layer-depth SMB, which is spatially mapped along the radar profiles. The internal reflection horizon used here is dated 21 years before 2012. More details for this approach can be found, for example, in Eisen et al. (2008).

We consider errors in linking the radar reflector to the tentative depth–age scale of ±1 year. The error in fitting the depth-density scale is calculated out of the misfit between the discrete ice-core samples and the density model (in a least square sense). Using standard error propagation, this yields a lower bound error of $\pm8\%$ for the SMB. In areas where the depth-density scale varies laterally, or where dynamic deformation of the radar layers is non-negligible the derived layer-depth is erroneous.

Ice thickness and layering of ice at depths greater than ± 50 m were measured using a 2 MHz radar system with resistivity loaded dipole antennas (Matsuoka et al. 2012) and a code-based GPS receiver. The system was towed at an average speed of 8-12 ~ km/h which results in a mean trace spacing of ~ 20 m. The principal steps of the post-processing included dewow filtering, bandpass filtering, and a depth-variable gain function. To account for the spatial separation of transmitter and receiver, oblique (but straight) propagation paths to the midpoint between the receiver and transmitter is assumed. Internal reflection horizons were picked in OpendTect. We derived depths from two-way travel time using a uniform propagation speed (168 m/μs) and add a bulk firn correction of 8.8 m based on density data (the shallowest, continuously picked radar reflector of the 2 MHz data is more than 120 m deep which is below the firn-ice transition). The vertical component of the GPS geotags was improved with differentially processed data from the L1L2 GPS.

Figure 2.8.2a illustrates the surface topography with a dome at the center. Along the divide the slope is steeper towards the south-west compared to the north-east. On other ice rises, Goodwin and Vaughan (1995) identified double-ridges which correspond to elongated depressions in the surface profile on either side of the divide. The double-ridges appear in satellite imagery as dark lineations accompanying the main divide. Martin et al. (2009) interpret the double-ridges as a feature which evolves over time as a consequence of ice anisotropy. We find no evidence for a double-ridge at Derwael Ice Rise neither in the elevation model of Figure 3.10a, nor in individual cross-profiles. The bed in Figure 2.8.2b is marine-based everywhere, exhibits a plateau in the vicinity of the dome and declines towards the south.
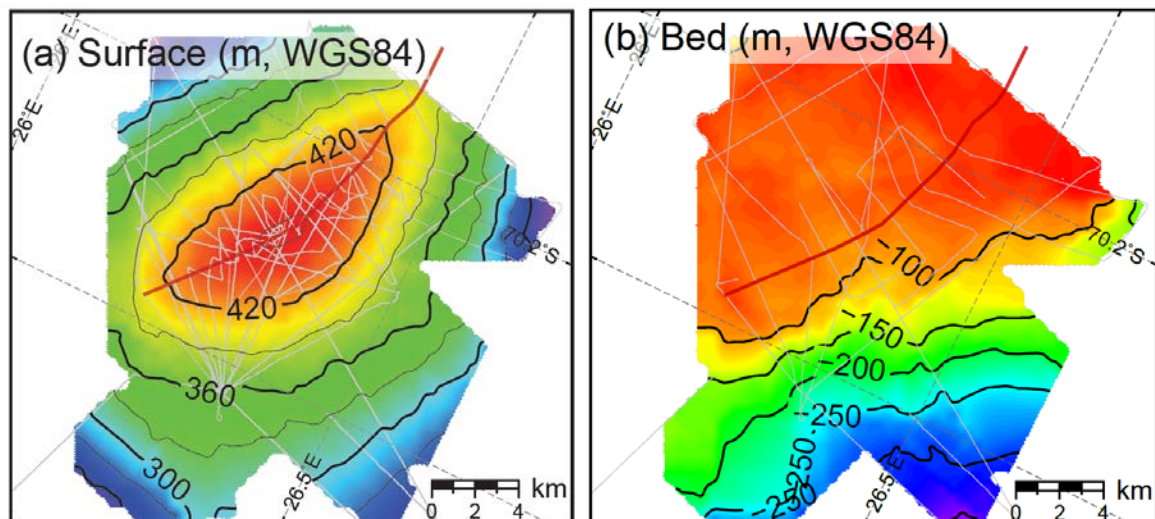

Figure 2.8.2: Interpolated maps of (a) surface elevation and (b) bed. The red curve indicates the divide position, white lines the profiles used for the interpolation.

2.9. Investigating the Raymond effect and timing of deglaciation

Many (if not all) internal reflection horizons which appear in the radar data are linked to depositional processes at the former surface and as such represent isochrones within the ice. At shallow depths, the spacing between layers is dominated by the amount of snowfall between their depositions. This allows deducting the spatial variations in accumulation. At larger depths, the stratigraphy is deformed through ice flow. For ice-rises in particular this can be used as a proxy for paleo-ice dynamics through the analysis of the Raymond effect. The Raymond effect is named after the initial publication of Raymond (1983), who predicted that the internal layering beneath ice divides should arch upwards due to the non-linear ice rheology. The resulting anticlines in the ice stratigraphy are referred to as isochrone arches or Raymond bumps.

Radar measurements are capable to illuminate the three-dimensional geometry of the Raymond bump. In combination with an ice-flow model, the characteristics of the Raymond bump (e.g. Bump-Amplitude vs. Depth function or the vertical alignment of the bump maxima) can be related to (non-)changing boundary conditions of the ice-dome (e.g. thinning or thickening, varying ice-thickness at the transition to the ice-shelf, etc.).

The radar dataset includes ten profiles which approximately cross the divide at a 90 degree angle. Figure 2.9.1 displays a typical radar profile. In many cases the main central Raymond stack is accompanied by a syncline on its north-western boundary and a side-stack on its south-eastern boundary. In both the LF and the HF data it is possible to pick several internal reflection horizons which connect all cross sections with each other. This allows for an interpolation in between and a comparison of the bump-amplitude versus depth function as a function of the along-ridge slope. This will be explained below.
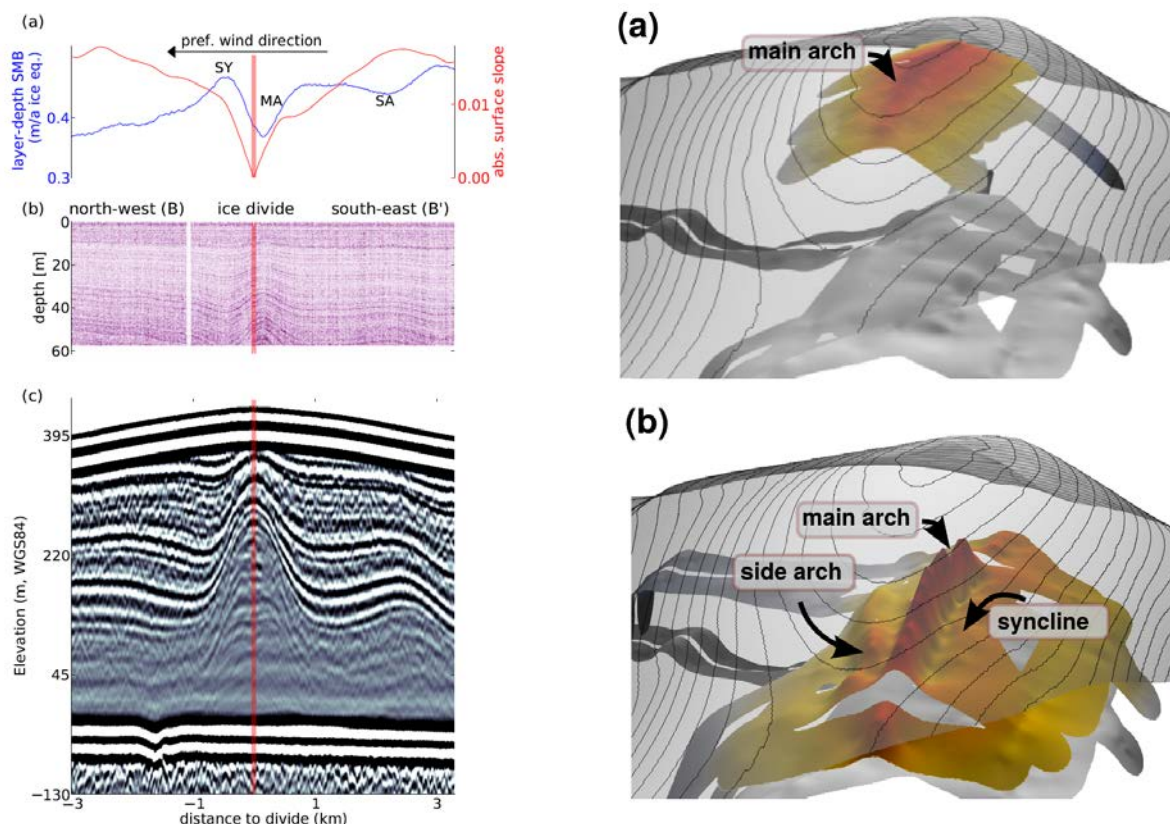
Figure 2.9.1: LEFT: Radar and GPS data collected along profile B-B'. See Figure 3.3 for the profile location. (a) Surface slope and layer-depth SMB. Radargrams in (b,c) are 400 MHz in (b) and 2 MHz in (c). Labeled are the main arch (MA) with its flanking syncline (SY), and the side arch (SA) in the south-eastern flank. The red vertical bar indicates the position of the topographic summit. RIGHT: Spatial interpolation of the englacial stratigraphy at average depths of 30 m (a) and 300 m (b). The surface and bed topography are given in grey. Viewing angle is from the north-east along the divide.

The field data is used together with a two dimensional, full-Stokes, thermomechanically-coupled, transient ice-flow model. The code is based on the finite element solver Elmer/Ice (Gagliardini et al. 2013) and includes implementations of isotropic and anisotropic ice rheology (Martin et al. 2009).

All model runs use a constant geothermal heat flux of 50 mW/m^2, which is a value consistent for the area of Derwael Ice Rise (Purucker et al. 2013). We prescribe no horizontal temperature gradient at the margins, and use a constant surface temperature of -13.5°C which stems from our own measurements at 10-20 m depths. We assume no basal sliding and the surface is allowed to evolve freely.

We consider two lateral boundary conditions: (1) a mass-conserving flux which exports the amount of ice which is equivalent to the integral over the surface mass balance from the divide to either side of the domain (Hvidberg 1996) and (2) an elevated flux resulting from the mass conserving flux plus a thinning rate χ (in m/a ice equivalent). The latter causes the surface to lower, since the exported mass is out of balance with the incoming surface mass balance.

Previous studies have shown that the arch amplitude is critically affected by the rheology used in the model (e.g., Martin et al. 2009). No field data directly constrain ice rheology in this study. Therefore, we use three different rheological settings. The first two settings are isotropic cases with Glen's power index $n = 3$ and $n = 4.5$. The latter is based on measurements at Greenland Summmit (Gillet-Chaulet et al. 2011). The third setting is an anisotropic case with $n = 3$ to account for a non-uniform alignment of ice-crystal axes. Ice anisotropy on ice rises has been inferred from seismic studies (Hofstede et al. 2013) and also linked to the double-peaked arches at greater depths (Martin et al. 2009). Hereafter, we refer to these three settings as I($n = 3$), I($n = 4.5$) and A($n = 3$), respectively.

For A($n = 3$), we initialize the model with an isotropic crystal orientation fabric which evolves with ice dynamics. We used fabric evolution parameters given by Martin et al. (2009). The model domain is centered at the divide and extends 8 km in both directions. The initial geometry is based on the bed and surface elevation from our own data. The mesh has 400 cells in the horizontal, which corresponds to a grid spacing of 40 m. I($n = 3$) and I($n = 4.5$) have 40 cells in the vertical ~14 m at the dome). To improve computational efficiency, we reduce the number of cells in the vertical to 30 (~18 m at the dome) for runs with A($n = 3$).

The main arch appears as a depth-continuous feature in the 2 MHz and 400 MHz radar data. There is strong theoretical evidence that the upward arching, at least at intermediate depths and below, is a consequence of the low deviatoric stresses near divides (the Raymond effect). Ice anisotropy additionally increases the upward arching at all depths and causes the double-peaks in the lower third of the ice column (Martin et al. 2009). The double-peaked arches are only visible in 2 MHz profiles close to the summit. However, because they develop at depths which are close to the radar detection limit, their absence in the radar data does not immediately mean that the double-peaked arches are exclusively present at the dome. In the model from Martin et al. (2009), which is also used here, the double-peaked arches start to develop after 1-2 times the characteristic time (ice thickness divided by SMB, ~1000 a for Derwael Ice Rise), suggesting that the Derwael Ice Rise has maintained its divide position longer than 1500 years.

Figure 2.9.2 illustrates the main arch's amplitude versus relative depth distribution for all cross sections. The amplitude is defined as the vertical distance between the arch maximum and a point in the flank (chosen 2 km away from the divide on the north-western flank). All values are normalized to the local ice thickness. The largest amplitudes, 25% of the ice thickness, are encountered near the dome. In cross sections farther away from the dome, the amplitudes are increasingly damped. We interpret the small arch amplitudes at steeper slopes are caused by along-ridge flow. Figure 4.1 illustrates the importance of taking the lateral positioning of the cross section into account when interpreting the arch amplitudes. The dependency on the along-ridge slope hampers a detailed comparison to other ice rises where the topography is often less well

constrained. Nevertheless, a gross comparison yields that the normalized amplitudes observed here are large, i.e., larger than Roosevelt Island (Martin et al. 2006), Siple Dome (Nereson and Raymond, 2001), Halvfaryyggen Ice Dome (Drews et al. 2013), and Kealey Ice Rise (Martin et al. 2014)); comparable to Fletcher Promotory (Hindmarsh et al. 2011), and Fuchs Piedmont (Martin et al. 2006).
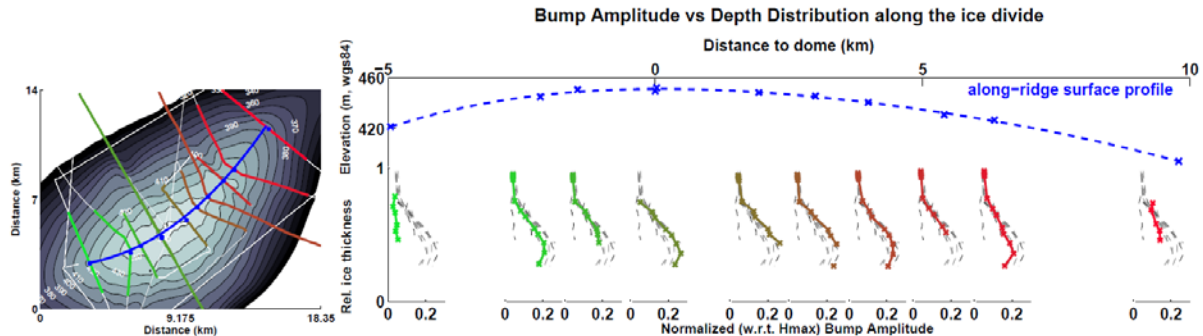

Figure 2.9.2: *Along-ridge variations of the main arch amplitudes. The main panel illustrates depth profiles of the arch amplitude relative to the local ice thickness in color corresponding to the radar profiles shown in the map. Amplitudes observed at other ridge-cross points are shown in gray as a reference.*

In order to minimize effects of along-ridge flow, we apply the two-dimensional model along a flowline across the dome (A–A', Figure 2.8.1). We first examine the arch amplitudes for steady-state conditions by applying the mass-conserving boundary conditions at the downstream model boundaries. We consider the three rheologies I($n = 3$), I($n = 4.5$), and A($n = 3$). The model is run to 10 times the characteristic time scale, i.e. 10000 year after which the geometry of the isochrones does not change significantly (apart from getting older).
The model is forced with the SMB that stems from the 400 MHz radar data and corresponds to a 21 year average before 2012. We multiply it by a constant, so that the magnitude corresponds to the 114 year long average at the site (Hubbard et al. 2013). We assume that the radar derived layer-depth SMB does not change in time.

Figure 2.9.3 displays the steady-state results for the smoothed SMB. We compare the radar reflectors with the isochrones of the modelled age field. All three cases match the internal radar layering in the flanks reasonably well, albeit the three deeper radar reflectors in the south-eastern high-SMB regime appear systematically lower than the modelled isochrones. The A($n = 3$) case produces larger double-peaked isochrone arches than the ones foreshadowed by the lowest radar reflector. The magnitude of the flanking syncline (around kilometer -1) is not well represented and also the remnants of the side arch (around kilometer 4) have no counterpart in the modelled age fields. Even though the arch amplitudes increase with increasing n and with anisotropy, all three cases result in a smaller main arch than the observed one.
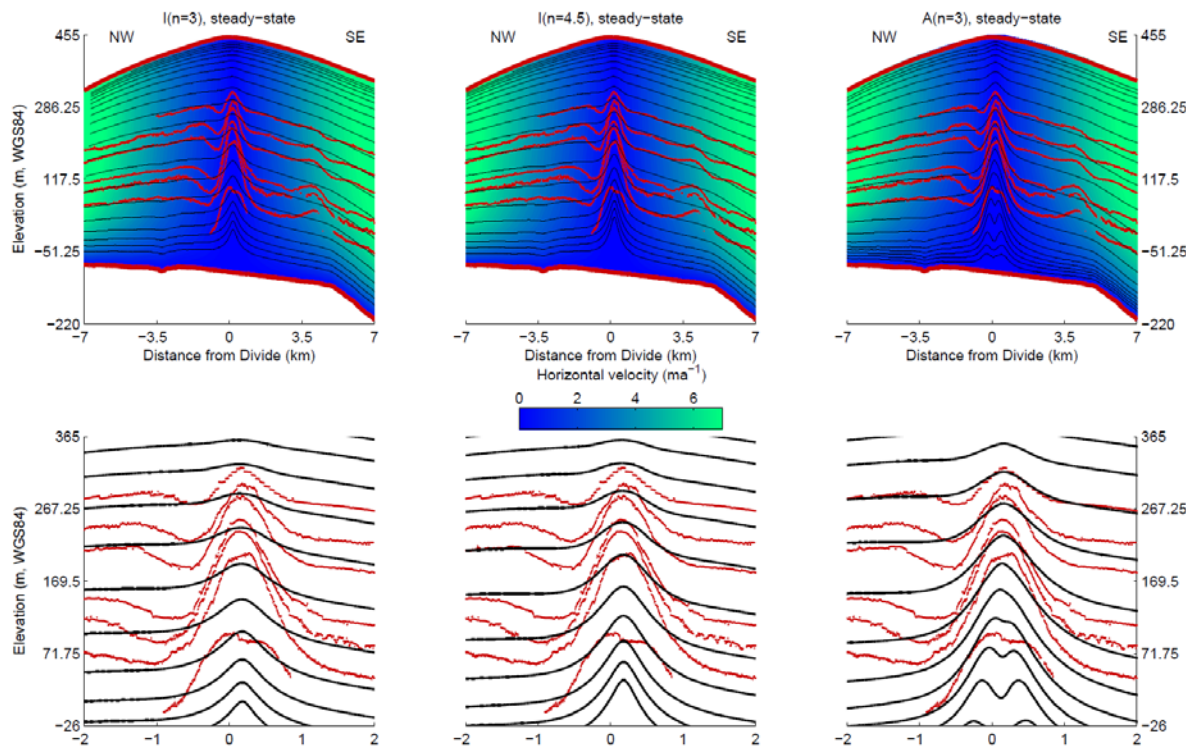
Figure 2.9.3*: Comparison of data and steady-state model outputs along the A-A' profile (Figure 2.8.1): The three panels on the top show the results for different rheologies and no thinning. The horizontal velocities are color-coded and modelled isochrones in black. The red curves correspond to the 2 MHz radar reflectors. The lower panels zoom closer to the divide.*

We next explore the possibility of thinning as some ice rises near the Antarctic coast have experienced thinning as the ice sheet retreated since the last glacial maximum (Vaughan et al. 1999, Martin et al. 2006). Here we use the smoothed layer-depth SMB, and initialize as described above with the exception that prior to the evolution, a constant ice thickness dH is added. This simulates a thicker ice rise with the same surface and bed geometry as Derwael Ice Rise. We evolve this ice rise to steady-state using the mass-conserving boundary condition. The absolute arch amplitudes are now larger because the ice rise is thicker. In the following step, the SMB is kept constant, but the thinning rate χ is added to the SMB within the integral that defines the flux boundary condition at the sides. This causes an imbalance of the incoming and outgoing mass fluxes and a lowering of the surface. We refer to these runs as being 'transient'. Since the internal stratigraphy does not adjust immediately to the new geometry, thinning results in oversized isochrone arches compared to the ones in a steady-state scenario with a constant ice thickness.
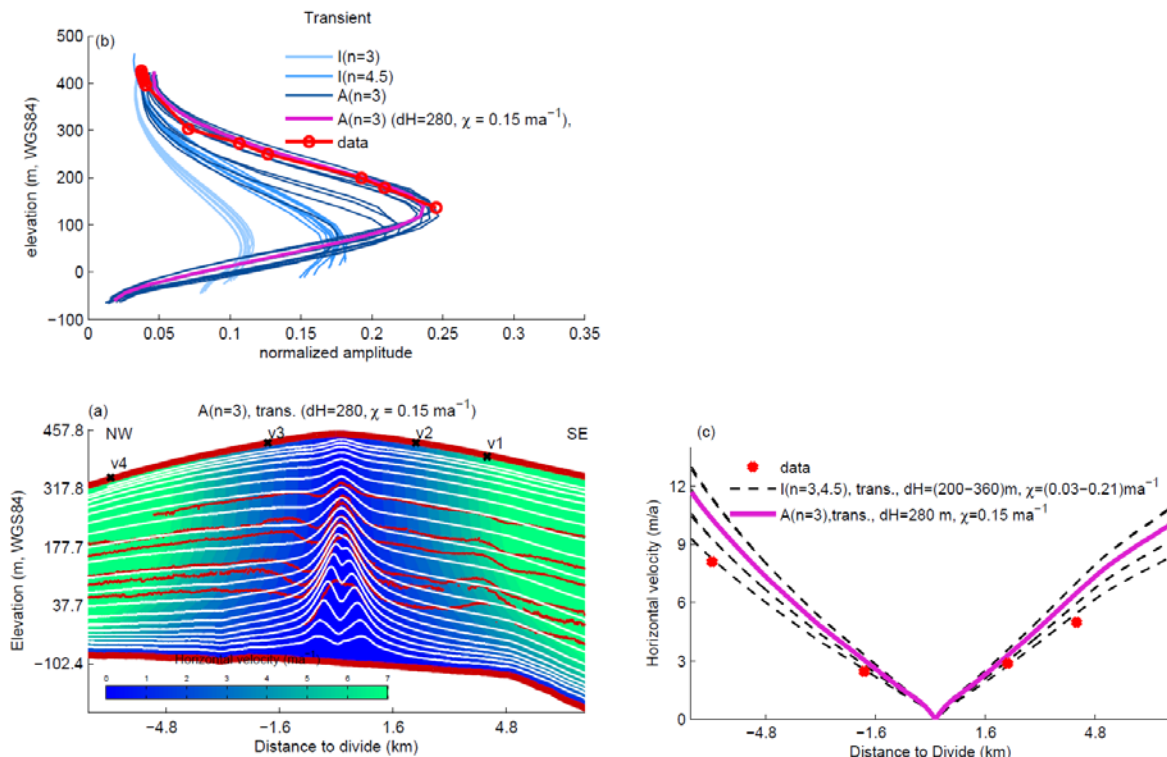
Figure 2.9.4: Transient model results. (a) modeled isochrones and flow speed (background color) for the case of dH = 280 m and χ = 0.15 m/a together with observed radar reflectors (red). (b) Depth profiles of the main arch amplitudes for all transient model cases (blue) and for observation (red). Our preferred model case is shown in magenta. (c) modeled horizontal flow speeds compared to the GPS measurements.

We consider values for dH of 200, 280, and 360 m and thinning rates χ of 0.03, 0.09, 0.15, and 0.21 m/a. The transient simulations are computed for the three rheologies mentioned above and stopped when the modelled surface matches the presently observed surface in a least squares sense.

Figure 2.9.4a displays the modelled arch amplitudes for all 36 cases. Ice rheology is the most important factor controlling the arch amplitudes, and there are three characteristics which are largely independent of the applied rheology: (1) increasing values of dH (and χ to a lesser extent for the ranges considered here) increase the final arch amplitudes, (2) as χ increases the maximum arch amplitudes appear at smaller depths, and (3) the surface velocities increase with χ and are virtually independent of dH. The I(n=3), I(n=4.5) cases result in too small amplitudes but we find a good match for A(n=3): The amplitudes are slightly underestimated for (dH, χ) = (280 m, 0.15 m/a), and slightly overestimated for (dH, χ) = (360 m, 0.15 m/a). In terms of surface velocities, we find the best match for χ = 0.03 m/a (independent of dH). In summary, to explain the arch amplitude of the Raymond effect of Derwael ice rise, long-term stable local-flow conditions should prevail, but the large amplitude can only further be explained by the fact that surface thinning is occurring, while anisotropic effects do play a major role in the deeper part under the ice divide.

An initial interpretation of the dataset is that (1) the recumbent arch is the remnant of a former divide migration which stopped sometime in the past to form the main isochrone arch which is seen today below the current divide, or (2) the recumbent arch is a remnant of a former triple junction, meaning in the past Derwael Ice Rise had two divides. So far it is unclear which forcing would cause this divide to migrate (or to vanish) and over which time-scales the migration occurred. Most likely candidates for the forcing are variations in the surrounding Roi Baudouin Ice Shelf, which induced thickness changes at the grounding line of Derwael Ice Rise. The different hypothesis can be further pursued by using ice-flow models.

The sustained thinning of Derwael Ice Rise in East Antarctica, along with the evidence of a former divide migration are likely indicative for changing dynamics in the sheet/shelf system surrounding the ice rise. This shows that the region is less stable than previously imagined which may have consequences for its future behaviour.

2.10. Effect of ice rises on the deglaciation of the ice sheet

Topographic highs on the continental shelf underneath ice shelves may induce the formation of either an ice rumple or an ice rise, once the ice shelf bottom is in contact with the so-called pinning point. Ice rumples are characterized by an overriding ice sheet and hence do not induce horizontal divergence of the main ice flow direction. Their formation has been previously studied numerically by Favier et al. (2012), who investigated how local grounding of an ice shelf has an important effect on grounding line advance: pinning of the ice shelf substantially increases buttressing, slows down the ice shelf, and makes the grounding line advance until it engulfs the ice rumple that has formed on top of the pinning point.

When the contact between an ice shelf and the pinning point is lost, one expects that the subsequent loss of buttressing leads to an acceleration of the ice and subsequent retreat of the grounding line (see the verification experiment by Favier et al. (2012)). However, acceleration of an ice sheet due to unpinning of the ice shelf has not been clearly demonstrated so far. In the Amundsen Sea sector, the eastern ice shelf of Thwaites Glacier has been accelerating since 2008 (Mouginot et al., 2014). This could be explained by a progressive unpinning of the ice shelf at its terminus (Tinto and Bell, 2011) or by a retreat of the grounding line caused by enhanced sub–ice shelf melting (Mouginot et al., 2014). Moreover, ungrounding of the eastern ice shelf of Thwaites Glacier seems to have little influence on the ice mass flux according to a recent model study (Joughin et al., 2014).

In order to gain an insight in the formation and evolution of ice rises, we test the hypothesis that ice rises are formed during deglaciation and subsequent grounding line retreat across the continental shelf since the Last Glacial Maximum. During that period, the East Antarctic Ice Sheet advanced to the continental shelf margin in some parts of East Antarctica, and the ice sheet characteristically thickened by 300–400 m near the present-day coastline at these sites (Mackintosh et al., 2014). This advance was associated with the formation of low-gradient ice streams that grounded at depths greater than 1 km below sea level on the inner continental shelf (Mackintosh et al., 2014).

With a state-of-the-art ice sheet model, we simulate the deglaciation of a grounded ice sheet resting over a continental shelf-like topography across a topographic high. Grounding line retreat is triggered by a constant rate in sea level rise over millennia. During the retreat, the topographic high gives rise to the development of an ice rise promontory and subsequently a local-flow ice rise, for which a steady state ice sheet/ice shelf system is obtained. Results are compared with a simulation lacking the topographic high to inform about the effect of ice rises on ice shelf stability, buttressing, and grounding line migration rates.

We use the freely available adaptive mesh finite-volume ice sheet model BISICLES (http://BISICLES.lbl.gov) (see Cornford et al. (2013) for a comprehensive overview of the model characteristics). BISICLES solves the Schoof-Hindmarsh approximation (L1L2) of the full Stokes equations on an adaptive horizontal grid produced with the Chombo adaptive mesh refinement toolkit.

Since the weak topographic high is engulfed by the grounded ice sheet at the initial state, there is hardly any surface expression of the topographic effect (Figure 2.10.1). Therefore, both initial steady states are comparable. Due to the limited influence of the topographic high, the initial grounding line is barely curved in plan view. Also, the final shape of the grounding line follows a straight line.
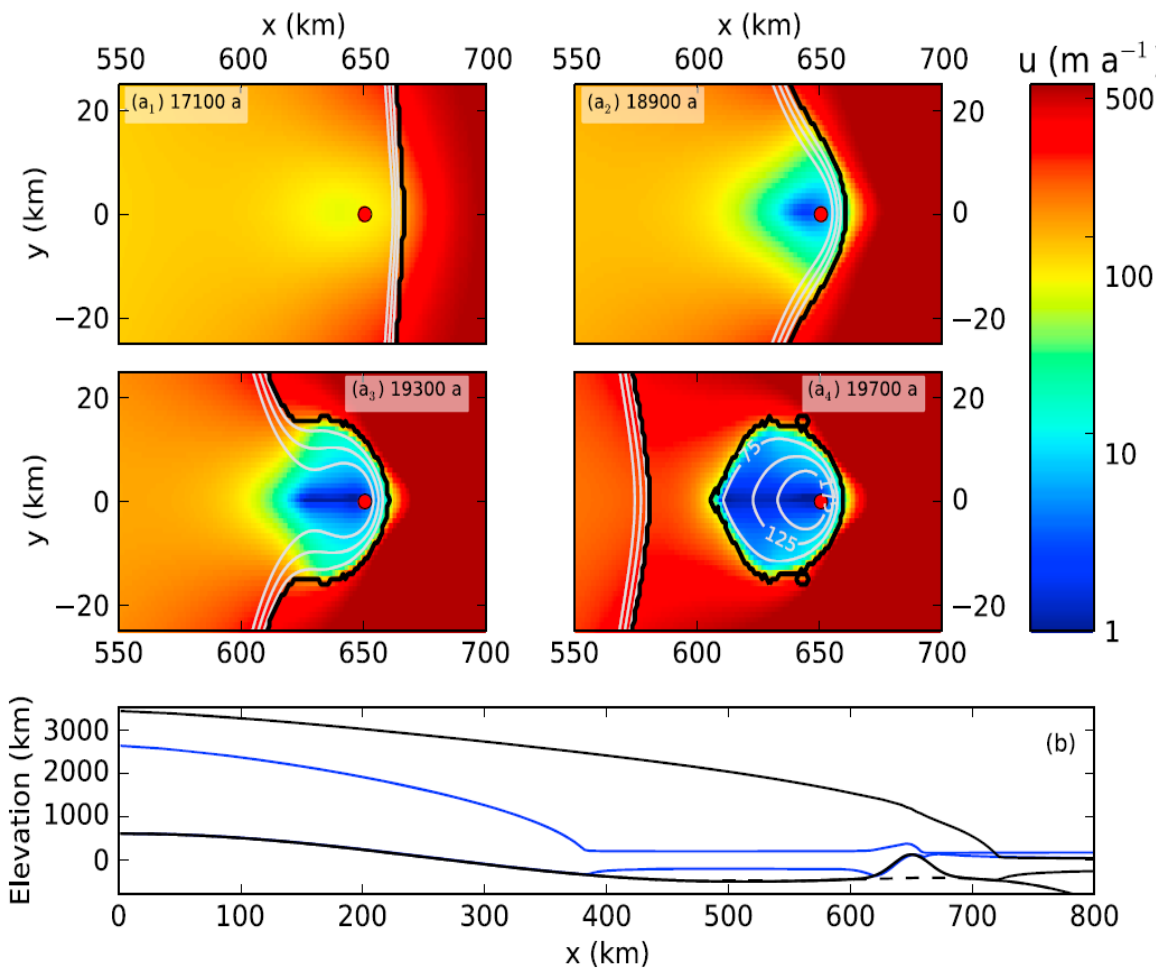
Figure 2.10.1: *(a1 –a4) Plan view snapshots (elapsed time written inside the figure) of the evolution of the grounding line during the formation of the ice rise. The red dot shows the topographic high summit, the gray lines are elevation contours (shown every 50 m from 75 m to 175 m height to focus on the ice rise), and the background color displays ice velocities. The complete movie of the transient behavior is included in the supporting information. (b) Elevations along the central flow line (y = 0). Bedrock elevation of the iceRise and noRise experiments are shown in solid and dashed black lines, respectively. The initial and final steady states of the iceRise experiments are shown in solid black and blue lines, respectively.*

The grounding line of the iceRise experiment is initially located approximately 1 km downstream of its position in the noRise experiment, and both initial volume above flotation are quite similar within a few percent. Durand et al. (2011) studied the effect of a topographic high beneath a 2-D grounded ice sheet on its volume above flotation and grounding line position in steady state, for different distances to the grounding line and height above the bed of the topographic high. In our simulations, this height is about 500 m above the bed and the high is located 70 km upstream of the grounding line at the initial steady state. For topographic highs with similar height and distance to the grounding line, the study by Durand et al. (2011) gave similar results, even though their simulation was 2-D and used a linear downsloping bed toward the sea. In our simulations, the topographic high has a more pronounced influence on the final steady state grounding line position. The non-buttressed ice shelf (not influenced by the topographic high) retreats 25 km farther inland compared to the buttressed ice shelf, which clearly demonstrates the effect of the buttressing involved by the newly established ice rise.

Contrary to the noRise experiment, where the grounding line is not influenced by lateral variations in ice flow, the grounding line in the iceRise experiment curves progressively around the topographic high between 15 and 19 ka (Figures 2.10.1 a1–a4). This curving first elucidates an ice

rise promontory, characterized by a local peak and separated from the main ice sheet by a saddle. The local peak equally induces local ice flow with flow speeds that are several orders of magnitude lower than the flow speeds of the surrounding ice shelf (Figures 2.10.1 a1–a4). During the next 500 years, the saddle area disconnects from the main grounded ice sheet and an ice rise appears. For the remaining time of the simulation, the main features of the ice rise barely change until the final steady state is reached. The final curvature of the main grounding line is straight, as it obviously is without the ice rise effect. This underscores that once the ice rise develops during grounding line retreat, it becomes a stable feature within the ice shelf.

We simulated for the first time the formation and evolution of an ice rise within an ice shelf and demonstrated that such a feature is the consequence of ice sheet deglaciation and inland migration of the grounding line across the continental shelf. A number of field-observable features showed up in the modeling: (i) a very low ice shelf thickness downstream of an ice rise that explains the formation of rifts, ice shelf breakup, and open water in similar areas in Antarctica; (ii) the formation of an ice rise promontory separated from the continental ice sheet by a saddle, which are found to be transient features; and (iii) the formation of a stable ice rise characterized by a radial ice flow center pattern on top of the topographic high pinning the ice shelf, while most of the ice flow from the ice shelf is diverted around the ice rise.

2.11. Importance of ice rises and pinning points on the deglaciation in Dronning Maud Land

The measurements and analyses are the prime input to constrain a coupled ice-sheet/ice-shelf model that is employed to investigate the deglaciation of the eastern Dronning Maud Land sector. This sector is characterized by a large drainage basin starting at the Dome Fuji ice divide towards the coast and encompassing the Sor Rondane Mountains and the Roi Baudouin ice shelf. Most of the ice discharge occurs around the range, especially through the West Ragnhild glacier that drains directly into the Roi Baudouin ice shelf, to the west of Derwael ice rise.

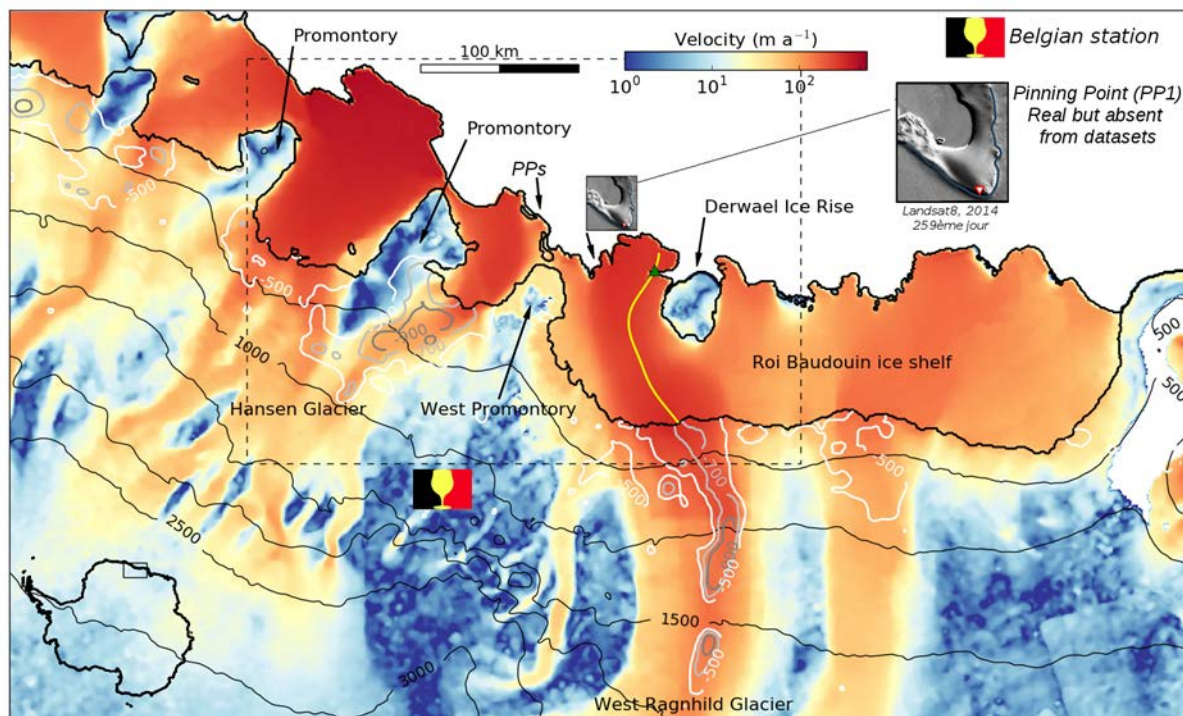**Figure 2.11.1**: *Computational domain with ice surface velocities in the background (Berger et al., 2016). The thick black lines show the grounding line – separating grounded ice from floating ice - and the calving front. The thin black lines show ice surface elevation contours every 500 m. The white, light grey, and dark grey lines are bed elevation contours of −500, −750, and −1000 m, respectively.*

The ice shelf fed by the West Ragnhild glacier is slowed down by a small pinning point (named PP1 in Figure 11.1), about 10 km2 in area, touching the ice shelf from beneath and inducing clearly visible surface expression. However, this pinning point is absent from the Antarctic dataset that are used by ice sheet modelers to constrain ice sheet models. Prior to making predictions of future ice sheet volume and their subsequent contribution to sea level changes, the ice sheet in models needs to be initialised to present day using ice geometry and surface velocity field. The initialisation enables to infer fundamental data that are not available through observations, such as the friction between the ice sheet and the bed beneath, and the stiffening of the ice that is due to various aspects of the ice rheology that are too poorly understood to be accounted for in the model. A typical example is the presence of crevasses among the ice shelf that can only be represented in the model through this ice stiffening. In the initialisation procedure, those two unknown parameters are optimised in order to best match observed current conditions of the ice sheet.

In Berger et al., 2016, we used the ice-sheet model BISICLES (Cornford et al., 2015) to initialise the area shown in Figure 11.1, using different datasets including or not including the pinning point PP1, in order to investigate the consequences of non accurate databases onto initialisation of ice sheet models. We discovered that the effect is quite dramatic around the pinning point in terms of ice stiffening. The ice-sheet model yields much stiffer ice in the vicinity of the pinning point when it is absent. The initialisation procedure is aimed at reproducing the ice surface velocity field by making slight changes in the basal friction and the stiffening factor. When a pinning point is absent, ice that is actually grounded is floating in the ice-sheet model. Therefore, the changes that cannot be made in the basal friction – there is no friction between the ice and the water beneath – are made in the stiffening factor by the model to better fit ice surface velocities (Figure 11.4). Another question was: how can such spurious initialisation will affect the behaviour of the ice sheet in the future.

We answer this question in the present study, which can be seen as a follow up of the study published by Berger et al., 2016. We investigated the impact of those two different initialisations – with or without the pinning point - onto the future ice sheet behaviour and its contribution to sea level changes. A third experiment was also setup to explore the effect of unpinning the ice sheet by using the initialisation accounting for the pinning point, and removing it during the first years of the time evolutive simulations. This kind of situation where a pinning point could lose its contact with the ice is likely to happen in the future with the current thinning of ice shelves around the Antarctic ice sheet. Those three different experiments (summarized in Table 11.1) were ran over the next millennium for two different scenarios of sub-ice shelf melting (which is the main driver of ice sheets current retreat) comparable to observations, and for two different sliding laws. A sliding law controls the interaction between the ice and the bed where the ice sheet is grounded. For clarity reasons, we show only the results obtained with the linear sliding law and the first type of sub-ice shelf melt rates (shown in Figure 11.2). Even though slight differences appear with the use of the non linear sliding law and the second kind of sub-ice shelf melt rates, similar conclusions remain. The other results are readable within the published paper (Favier et al., 2016).

	Dataset used for	
Experiment name	Initialisation (ice geometry and velocity)	Initial geometry
Reference	With PP1 (Berger et al., 2016)	With PP1 (Berger et al., 2016)
Unpinning	With PP1 (Berger et al., 2016)	Without PP1 (Fretwell et al., 2013)
NoPP	Without PP1 (Fretwell et al., 2013; Rignot et al., 2011)	Without PP1 (Fretwell et al., 2013)

Table 2.11.1: *Experiments shown in this document for the linear sliding law and the first type of sub-ice shelf melt rates. We explored three melting scenarios, using low, medium and high melting, all comparable to current observations.*
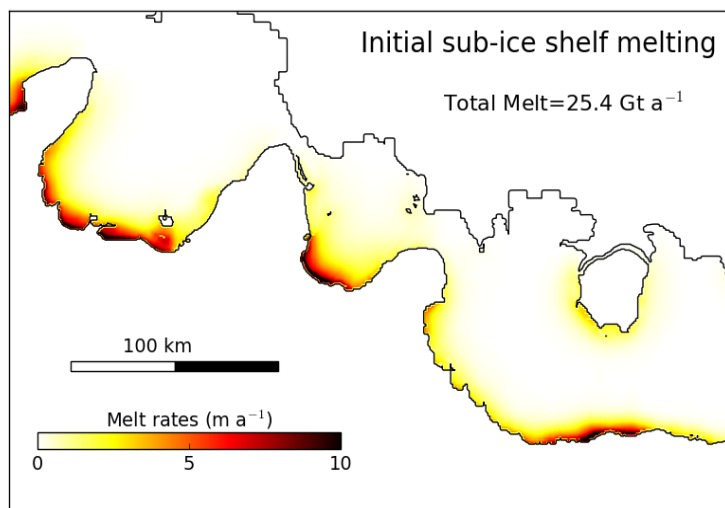
Figure 2.11.2: One of the two types of sub-ice melt rates applied to the ice sheet, here for the medium melting experiment, which yields overall melting almost equal to the observations (Rignot et al., 2013; Depoorter et al., 2013).

From now on, we focus on the evolution over the next millennium of the three drainage basins of Tusse, Hansen and West Ragnhild glaciers (Figure 11.1). The main steps of grounding line migration and contribution to sea level changes are shown in Figure 11.4 for the Reference experiments. Whatever the amount of sub-ice shelf melting (three values comparable to current observations were tested), the model shows a retreat of the Hansen glacier grounding line. The retreat here is much quicker and larger than for the other two glaciers. As shown in Figure 11.1, the bed upstream of the grounding line is quite deep and wide beneath the Hansen glacier. This makes the ice sheet prone to an instability called Marine Ice Sheet Instability (MISI), which happens in that case. Even though the bed upstream of the West Ragnhild glacier grounding line has an equal depth, it is also comparatively much narrower, which makes the glacier more stable and prevents any retreat. Overall, the ice-sheet model predicts that this sector of the East Antarctic ice sheet will have rised the current sea level by 35 +/- 10 mm by the end of the next millennium, which needs to be put in perspective with the small domain simulated (representing about 1 % of the Antarctic ice sheet) and the possible increase of sub-ice shelf melting over time while they are held constant in this study.

The immediate acceleration of ice that follows the unpinning of PP1 is shown in Figure 11.3. The speed-up of the ice reaches 300 m a^{-1} at the former location of PP1, and the velocities at the ice-shelf front are about 20 % higher. This however does not increase much the future contribution to sea level compared to the Reference experiment (about 10 % more sea level rise due to unpinning of PP1).

Figure 2.11.3: Speed up of the ice sheet due to unpinning after 50 years for the medium melt rates experiment and linear sliding. We show absolute velocity differences in m a^{-1}.
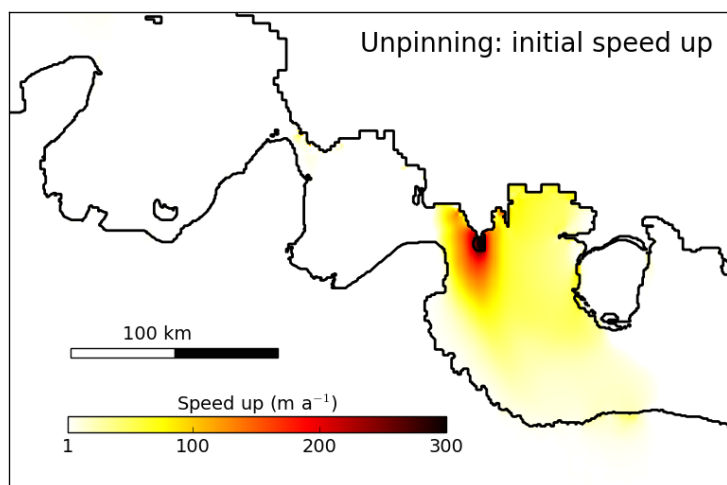
The increase of sub-ice shelf melting increases the contribution to sea level rise. Regardless of the experiment type, we obtain about 25 mm of contribution for the lowest melting scenario up to 45 mm for the highest melting scenario.
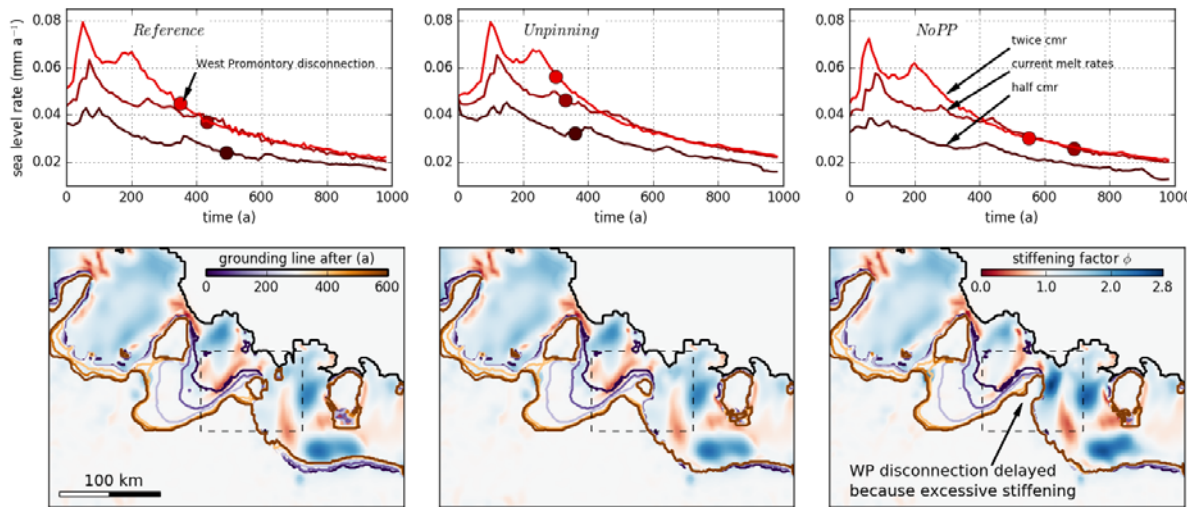

Figure 2.11.4*: Results of the linear sliding experiments for the Reference (left column), Unpinning (medium column) and NoPP (right column) experiments. The top row shows the sea level change rates for the three different values of sub-ice shelf melting. The bottom row shows grounding line positions every 100 years, with the stiffening factor obtained during initialisation at the background (blue is stiffer ice while red is softer ice – see the patch of stiff ice appearing close to PP1 when it is not accounted for in the initialisation).*

Omitting PP1 in the initialisation of the ice sheet (see the noPP experiment) decreases the contribution to sea level rise by about 10 % compared to the Reference experiment. This is due to the spurious excessive stiffening (right hand side of Figure 11.4) computed by the model to match ice surface velocities. It has also a local consequence in the retreat of the grounding line between the West Ragnhild and the Hansen glaciers. The transition between a promontory and an ice rise that occurs there is delayed by 200 years or so compared to the Reference experiment. This study thus confirms the fact that ice promontories are transient features of the ice sheet during a deglaciation (Section 2.10), which means that they are not stable when the ice sheet retreats, and that they quickly transition into ice rises.

Since the early 2000s, uncertainties of ice-sheet modelling outputs have been reduced by substantial numerical improvements, enabling key processes to be grasped more accurately such as grounding-line migration. We are now able to simulate the behaviour of the Antarctic ice sheet using complex models at a high spatial resolution in the relevant areas for a wide range of scenarios over the next centuries, which was not feasible a few years ago. Nevertheless, the lack of knowledge of essential observations still affects our ability to forecast the future behaviour of the ice sheets. This is of high concern because of their potential to rise global sea level by metres. The improvement of these predictions using ice sheet models will have to go through more knowledge of the bathymetry beneath ice shelves, where a substantial amount of these small pinning points can be found, especially in the eastern part of Dronning Maud Land.

3. POLICY SUPPORT

The partners within IceCon have been actively involved in policy support. Since IceCon research fits within the SCAR Horizon Scan priorities, members of IceCon have been effectively involved on different policy levels to disseminate research results and guide science policy on the international level. F. Pattyn is SCAR national delegate and SCAR representative of the international programme ISMASS (Ice Sheet Mass Balance and Sea Level). He has recently been appointed as member of the Steering Committee of SCERCE, one of the main research programmes of SCAR. He has also informed AntClim21 via a workshop invitation. F. Pattyn and J.L. Tison are national representatives of the Standing Scientific Group (SSG) of Physical Sciences (SCAR) and N. Bergeot has just become appointed national representative of the SSG Geosciences. J.L. Tison is also member of the European Polar Board.

F. Pattyn has in collaboration with T. Camelbeeck organized the first scientific conference on research at the Princess Elisabeth Station in 2016, to which policy makers were invited. The symposium was opened by the Secretary of State for Federal Science Policy, Ms Elke Sleurs.

4. DISSEMINATION AND VALORISATION

The IceCon project has led to a large number of new results. Based on the legacy of previous projects on the Roi Baudouin ice shelf in Dronning Maud Land, Antarctica (BELISSIMA), equally supported by BELSPO, we now dispose of a large and very detailed dataset of GNSS, radar, snow density, ice composition and ice core records. With the advent of the Princess Elisabeth Station, this led for the first time to such a large scale monitoring and measurement programme since the region was first visited at the end of the 1950s. All data has been collected in collaboration with our international partners, and conform SCAR policy, is publicly available. Published datasets are available on the Pangaea platform. Analyzed ice-core data is available via https://doi.pangaea.de/10.1594/PANGAEA.857574; collected and processed radar data via https://doi.pangaea.de/10.1594/PANGAEA.836299.

Results of the research are published in international peer reviewed journals of high impact factor and have been presented on international conferences, such as AGU, EGU, and IGS symposia.

Broader dissemination of results has been done via media and social media. The website of the IceCon expeditions (http://icecon2012.blogspot.be/) has been linked to Facebook and Twitter. Four published IceCon papers have received media attention via the ULB media hub (ULB and Faculty of sciences) as well as in the national and international press.

5. PUBLICATIONS

Berger, S., L. Favier, R. Drews, J.J. Derwael, F. Pattyn (2016) Uncharted pinning points and their control on the flow of Antarctic ice shelves. J. Glaciol., in press.

Callens, D., K. Matsuoka, D. Steinhage, B. Smith, E. Witrant and F. Pattyn (2014) Transition of flow regime along a marine-terminating outlet glacier in East Antarctica. The Cryosphere. 8, 867-875.

Callens, D., N. Thonnard, J. Lenaerts, W.J. van de Berg, K. Matsuoka, and F. Pattyn (2015) Mass balance of the Sør Rondane Glacier System, East Antarctica. Annals of Glaciology 56(70): 63-69.

Callens, D., R. Drews, E. Witrant, M. Philippe, F. Pattyn (2016) Temporally stable surface mass balance asymmetry across an ice rise derived from radar internal reflection horizons through inverse modeling. J. Glaciol. 62(233): 525-534.

Callens, Denis; Matsuoka, Kenichi; Steinhage, Daniel; Pattyn, Frank (2015): Surface elevation and ice thickness measurements of an airborne radar survey made in the Sør Rondane Mountains, Antarctica. doi:10.1594/PANGAEA.836299.

Drews, R., K. Matsuoka , C. Martin, D. Callens , N. Bergeot , and F. Pattyn (2015) Sustained thinning over millennia of an ice rise in Dronning Maud Land, Antarctica.Journal of Geophysical Research (Earth Surface) doi:10.1002/2014JF003246

Drews, R., J. Brown, K. Matsuoka, E. Witrant, M. Philippe, B. Hubbard, F. Pattyn (2016) Constraining variable density of ice shelves using wide-angle radar measurements. The Cryosphere 10:811-823.

Favier, L. and F. Pattyn (2015) Antarctic ice-rise formation, evolution and stability. Geophysical Research Letters 42, doi:10.1002/2015GL064195.

Favier, L., F. Pattyn, S. Berger, R. Drews (2016) Dynamic influence of pinning points on marine ice-sheet stability: a numerical study in Dronning Maud Land, East Antarctica. The Cryosphere. Accepted.

Hubbard, B., J.L. Tison, M. Philippe, B. Heene, F. Pattyn, T. Malone, J. Freitag (2013) Ice-shelf density reconstructed from optical-televiewer borehole logging. Geophys. Res. Lett. 40 (22): 5882-5887.

Lenaerts, Jan, Brown, Joel, van den Broeke, Michiel, Matsuoka, Kenichi, Drews, Reinhard, Callens, Denis, Philippe, Morgane, Gorodetskaya, I.V., van Meijgaard, E., Tijm - Reijmer, Catharina, Pattyn, F. & van Lipzig, N.P.M. (2014). High variability of climate and surface mass balance induced by Antarctic ice rises.Journal of glaciology, 60 (224), (pp. 1101-1110).

Lenaerts, J.T.M., S. Lhermitte, R. Drews, S.R.M. Ligtenberg, S. Berger, V. Helm, C.J.P.P. Smeets, M.R. vandenBroeke, W.J. vandeBerg, E. van Meijgaard, M. Eijkelboom, O. Eisen and F. Pattyn (2016) Meltwater produced by wind-albedo interaction stored in an East Antarctic ice shelf. Nature Climate Change. In press.

Matsuoka, K, R.C.A. Hindmarsh, G Moholdt, M. J. Bentley, H. D. Pritchard, J. Brown, H. Conway, R. Drews, G. Durand, D. Goldberg, T. Hattermann, J. Kingslake, J.T.M. Lenaerts, C. Martín, R. Mulvaney, K. Nicholls, F. Pattyn, N. Ross, T. Scambos, P. Whitehouse (2015) Antarctic ice rises and rumples: their properties and significance for ice-sheet dynamics and evolution. Earth Science Reviews 150, 724-745.

Philippe, M., J.-L. Tison, K. Fjøsne, B. Hubbard, H. A. Kjær, J. T. M. Lenaerts, S. G. Sheldon, K. De Bondt, P. Claeys, and F. Pattyn (2016) Ice core evidence for a 20th century increase in surface mass balance in coastal Dronning Maud Land, East Antarctica. The Cryosphere 10: 2501-2516.

Philippe, Morgane; Tison, Jean-Louis; Fjøsne, Karen; Hubbard, Bryn; Kjær, Helle A; Lenaerts, Jan T M; Drews, Reinhard; Sheldon, Simon G; De Bondt, Kevin; Claeys, Philippe; Pattyn, Frank (2016): Annual layer thicknesses and age-depth (oldest estimate) of Derwael Ice Rise (IC12), Dronning Maud Land, East Antarctica. doi:10.1594/PANGAEA.857574

6. ACKNOWLEDGMENTS

7. REFERENCES

Altamimi, Z., P. Rebischung, L. Métivier, and C. Xavier (2016), ITRF2014: A new release of the International Terrestrial Reference Frame modeling nonlinear station motions, J. Geophys. Res. Solid Earth, 121, 6109–6131, doi:10.1002/2016JB013098.

Altamimi Z, P. Sillard, C. Boucher (2007), CATREF software: Combination and analysis of terrestrial reference frames. LAREG Technical, Institut Géographique National, Paris, France

Altnau, S., Schlosser, E., Isaksson, E., and Divine, D.: Climatic signals from 76 shallow firn cores in Dronning Maud Land, East Antarctica, The Cryosphere, 9, 925–944, doi:10.5194/tc-9-925-2015, 2015.

Anschütz, H., Sinisalo, A., Isaksson, E., McConnell, J. R., Ham- ran, S.-E., Bisiaux, M. M., Pasteris, D., Neumann, T. A., and Winther, J.-G.: Variation of accumulation rates over the last eight centuries on the East Antarctic Plateau derived from volcanic signals in ice cores, J. Geophys. Res., 116, D20103, doi:10.1029/2011JD015753, 2011.

Aristarain, A. J., Delmas, R. J., and Stievenard, M.: Ice-core study of the link between sea-salt aerosol, sea-ice cover and climate in the Antarctic Peninsula area, Clim. Change, 67, 63-86, doi:10.1007/s10584-004-0708-6, 2004.

Arthern, R. J., Vaughan, D. G., Rankin, A. M., Mulvaney, R., and Thomas, E. R.: In situ measurements of Antarctic snow compaction compared with predictions of models, J. Geophys. Res., 115, F03011, doi:10.1029/2009JF001306, 2010.

Berger, S., Favier, L., Drews, R., Derwael, J.-J., and Pattyn, F. (2016) The control of an uncharted pinning point on the flow of an Antarctic ice shelf, J. Glaciol., 62, 37–45, doi:10.1017/jog.2016.7.

Boening, C., Lebsock, M., Landerer, F., and Stephens, G.: Snowfall driven mass change on the East Antarctic ice sheet, Geophys. Res. Lett., 39, L21501, doi:10.1029/2012GL053316, 2012.

Bromwich, D. H., Nicolas, J. P., and Monaghan, A. J.: An assessment of precipitation changes over Antarctica and the Southern Ocean since 1989 in contemporary global reanalyses, J. Clim., 24, 4189–4209, doi:10.1175/2011jcli4074.1, 2011.

Bromwich, D. H., Nicolas, J. P., Monaghan, A. J., Lazzara, M. A., Keller, L. M., Weidner, G. A., and Wilson, A. B.: Corrigendum: Central West Antarctica among the most rapidly warming regions on Earth, Nat. Geosci., 7, 76–76, doi:10.1038/ngeo2016, 2014.

Callens, D., Drews, R., Witrant, E., Philippe, M., and Pattyn, F.: Temporally stable surface mass balance asymmetry across an ice rise derived from radar internal reflection horizons through inverse modeling, J. Glaciol., 1, 1–10, doi:10.1017/jog.2016.41, 2016.

Cornford, S. L., Martin, D. F., Payne, A. J., Ng, E. G., Le Brocq, A. M., Gladstone, R. M., Edwards, T. L., Shannon, S. R., Agosta, C., van den Broeke, M. R., Hellmer, H. H., Krinner, G., Ligtenberg, S. R. M., Timmermann, R., and Vaughan, D. G. (2015) Century scale simulations of the response of the West Antarctic Ice Sheet to a warming climate, The Cryosphere, 9, 1579–1600, doi:10.5194/tc-9-1579-2015.

Cuffey, K. M. and Paterson, W.: The Physics of Glaciers, Elsevier, 693 pp., doi:10.1016/c2009-0-14802-x, 2010. Dansgaard, W. and Johnsen, S.: A flow model and a time scale for the ice core from Camp Century, Greenland, J. Glaciol., 8, 215– 223, 1969.

Dach R., F. Andritsch, D. Arnold, S. Bertone, P. Fridez, A. Jäggi,Y. Jean, A. Maier, L. Mervart, U. Meyer, E. Orliac, E. Ortiz–Geist, L. Prange, S. Scaramuzza, S. Schaer, D. Sidorov, A. Sušnik, A. Villiger, P. Walser, C. Baumann, G. Beutler, H. Bock, A. Gäde, S. Lutz, M. Meindl, L. Ostini, K. Sośnica, A. Steinbach, D. Thaller (2015), Bernese GNNS Software Version 5.2, Eds. R. Dach, S. Lutz, P. Walser and P. Fridez, Astron. Inst. University of Bern, Switzerland

Dansgaard, W. and Johnsen, S. (1969), A flow model and a time scale for the ice core from Camp Century, Greenland, J. Glaciol., 8, 215–223.

Davis, C. H., Li, Y., McConnell, J. R., Frey, M. M., and Hanna, E.: Snowfall-driven growth in East Antarctic Ice Sheet mitigates recent sea-level rise, Science, 308, 1898–1901, doi:10.1126/science.1110662, 2005.

Dee, D. P. and Uppala, S. M.: Variational bias correction of satellite radiance data in the ERA-Interim reanalysis, Q. J. Roy. Meteorol. Soc., 135, 1830–1841, doi:10.1002/qj.493, 2009.

Ding, M., Xiao, C., Li, Y., Ren, J., Hou, S., Jin, B., and Sun, B.: Spatial variability of surface mass balance along a traverse route from Zhongshan station to Dome A, Antarctica, J. Glaciol., 57, 658–666, doi:10.3189/002214311797409820, 2011.

Dow, J.M., Neilan, R.E. & Rizos, C. (2009), The International GNSS Service in a changing landscape of Global Navigation Satellite Systems, J Geod 83: 191. doi:10.1007/s00190-008-0300-3

Drews, R., Steinhage, D., Martín, C., and Eisen, O.: Characterization of glaciological conditions at Halvfarryggen ice dome, Dronning Maud Land, Antarctica, J. Glaciol., 59, 9–20, doi:10.3189/2013JoG12J134, 2013.

Drews, R., Matsuoka, K., Martín, C., Callens, D., Bergeot, N., and Pattyn, F.: Evolution of Derwael Ice Rise in Dronning Maud Land, Antarctica, over the last millennia, J. Geophys. Res.-Earth, 120, 564–579, doi:10.1002/2014JF003246, 2015.

Elsberg, DH, Harrison WD, Zumberge MA, Morack JL, Pettit EC, Waddington ED, Husmann E. (2004), Depth- and time-dependent vertical strain rates at Siple Dome, Antarctica. Journal of Glaciology. 50:511-521.

Favier, L., F. Pattyn, S. Berger, R. Drews (2016) Dynamic influence of pinning points on marine ice-sheet stability: a numerical study in Dronning Maud Land, East Antarctica. The Cryosphere, 10, 2623-2635, doi:10.5194/tc-10-2623-2016.

Fernandoy, F., Meyer, H., Oerter, H., Wilhelms, F., Graf, W., and Schwander, J.: Temporal and spatial variation of stable- isotope ratios and accumulation rates in the hinterland of Neumayer station, East Antarctica, J. Glaciol., 56, 673–687, doi:10.3189/002214310793146296, 2010.

Frezzotti, M., Pourchet, M., Flora, O., Gandolfi, S., Gay, M., Urbini, S., Vincent, C., Becagli, S., Gragnani, R., Proposito, M., Severi, M., Traversi, R., Udisti, R., and Fily, M.: New estimations of precipitation and surface sublimation in East Antarctica from snow accumulation measurements, Clim. Dynam., 23, 803–813, doi:10.1007/s00382-00004-00462-0038500803-00813, 2004.

Frezzotti, M., Pourchet, M., Flora, O., Gandolfi, S., Gay, M., Urbini, S., Vincent, C., Becagli, S., Gragnani, R., Proposito, M., Severi, M., Traversi, R., Udisti, R., and Fily, M.: Spatial and temporal variability of snowaccumulation in East Antarctica from traverse data, J. Glaciol., 51, 113–124, doi:10.3189/172756505781829502, 2005.

Frezzotti, M., Scarchilli, C., Becagli, S., Proposito, M., and Urbini, S.: A synthesis of the Antarctic surface mass balance during the last 800 yr, The Cryosphere, 7, 303–319, doi:10.5194/tc-7-303-2013, 2013.

Frieler, K., Clark, P. U., He, F., Buizert, C., Reese, R., Ligten- berg, S. R., van den Broeke, M. R., Winkelmann, R., and Levermann, A.: Consistent evidence of increasing Antarctic accumulation with warming, Nat. Clim. Change, 5, 348–352, doi:10.1038/nclimate2574, 2015.

Fudge, T. J., Markle, B. R., Cuffey, K. M., Buizert, C., Taylor, K. C., Steig, E. J., Waddington, E. D., Conway, H., and Koutnik, M.: Variable relationship between accumulation and temperature in West Antarctica for the past 31,000 years, Geophys. Res. Lett., 43, 3795–3803, doi:10.1002/2016GL068356, 2016.

Fujita, S., Holmlund, P., Andersson, I., Brown, I., Enomoto, H., Fujii, Y., Fujita, K., Fukui, K., Furukawa, T., Hansson, M., Hara, K., Hoshina, Y., Igarashi, M., Iizuka, Y., Imura, S., Ingvander, S., Karlin, T., Motoyama, H., Nakazawa, F., Oerter, H., Sjöberg, L. E., Sugiyama, S., Surdyk, S., Ström, J., Uemura, R., and Wilhelms, F.: Spatial and temporal variability of snow accumulation rate on the East Antarctic ice divide between Dome Fuji and EPICA DML, The Cryosphere, 5, 1057–1081, doi:10.5194/tc-5- 1057-2011, 2011.

Genthon, C., Krinner, G., and Castebrunet, H.: Antarctic precipitation and climate-change predictions: horizontal resolution and margin vs plateau issues, Ann. Glaciol., 50, 55–60, doi:10.3189 /172756409787769681, 2009.

Gillet-Chaulet, F., Hindmarsh, R. C., Corr, H. F., King, E. C., & Jenkins, A. (2011). In-situquantification of ice rheology and direct measurement of the Raymond Effect at Summit, Greenland using a phase-sensitive radar. Geophysical Research Letters, 38(24).

Gorodetskaya, I. V., Van Lipzig, N. P. M., Van den Broeke, M. R., Mangold, A., Boot, W., and Reijmer, C. H.: Meteorological regimes and accumulation patterns at Utsteinen, Dronning Maud Land, East Antarctica: Analysis of two contrasting years, J. Geophys. Res.-Atmos., 118, 1700-1715, doi:10.1002/jgrd.50177, 2013.

Gorodetskaya, I. V., Tsukernik, M., Claes, K., Ralph, M. F., Neff, W. D., and Van Lipzig, N. P. M.: The role of atmospheric rivers in anomalous snow accumulation in East Antarctica, Geophys. Res. Lett., 41, 6199-6206, doi:10.1002/2014GL060881, 2014.

Gorodetskaya, I. V., Kneifel, S., Maahn, M., Van Tricht, K., Thiery, W., Schween, J. H., Mangold, A., Crewell, S., and Van Lipzig, N. P. M.: Cloud and precipitation properties from ground-based remote-sensing instruments in East Antarctica, The Cryosphere, 9, 285–304, doi:10.5194/tc-9-285-2015, 2015.

Hamilton, G. S., & Whillans, I. M. (2000). Point measurements of mass balance of the Greenland ice sheet using precision vertical global positioning system (GPS) surveys. J. Geophys. Res.: Solid Earth, 105(B7), 16295-16301.

Hamilton, G.S., I.M. Whillans and P.J. Morgan (1998), First point measurements of ice sheet thickness change in Antarctica. Ann. Glaciol., v.27, 125-129.

Hammer, C. U.: Acidity of polar ice cores in relation to absolute dating, past volcanism, and radio-echoes, J. Glaciol., 25, 359– 372, doi:10.3198/1980JoG25-93-359-372, 1980.

Hammer, C. U., Clausen, H. B., and Langway Jr., C. C.: Electrical conductivity method (ECM) stratigraphic dating of the Byrd Station ice core, Antarctica, Ann. Glaciol., 20, 115–120, doi:10.3189/172756409787769681, 1994.

Hawley, R. L. and Waddington, E. D. (2011), In situ measurements of firn compaction profiles using borehole optical stratigraphy, J. Glaciol., Vol. 57, No. 202.

Hawley, R. L., Waddington, E. D., Morse, D. L., Dunbar, N. W., & Zielinski, G. (2002), Dating firn cores by vertical strain measurements. J. Glaciol., 48(162), 401-406.

Hofstede, C. M., van de Wal, R. S. W., Kaspers, K. A., van den Broeke, M. R., Karlöf, L., Winther, J. G., Isaksson, E., Lappegard, G., Mulvaney, R., Oerter, H., and Wilhelms, F.: Firn accumulation records for the past 1000 years on the basis of dielectric profiling of six firn cores from Dronning Maud Land, Antarctica, J. Glaciol., 50, 279–291, doi:10.3189/172756504781830169, 2004.

Hubbard, B., Roberson, S., Samyn, D., and Merton-Lyn, D. (2008), Digital optical televiewing of ice boreholes. J. Glaciol., 54(188), 823-830.

Hubbard, B., Tison, J. L., Pattyn, F., Dierckx, M., Boereboom, T., and Samyn, D. (2012), Optical-televiewer-based identification and characterization of material facies associated with an Antarctic ice-shelf rift, Ann. Glaciol., 53(60), 137-146.

Hubbard, B., and Malone, T. (2013a), Optical-televiewer-based logging of the uppermost 630 m of the NEEM deep ice borehole, Greenland. Ann. Glaciol., 54(64), 83-89.

Hubbard, B., Tison, J.-L., Philippe, M., Heene, B., Pattyn, F., Malone, T., and Freitag, J. J.: Ice shelf density reconstructed from optical televiewer borehole logging, Geophys. Res. Lett., 40, 5882-5887, doi:10.1002/2013gl058023, 2013b.

Hubbard, B., Luckman, A., Ashmore, D. W., Bevan, S., Kulessa, B., Kuipers, M. P., ... and Tison, J. L. (2016), Massive subsurface ice formed by refreezing of ice-shelf melt ponds. Nat. Comm., 7, 11897.

Isaksson, E. and Melvold, K.: Trends and patterns in the recent accumulation and oxygen isotope in coastal Dronning Maud Land, Antarctica: interpretations from shallow ice cores, Ann. Glaciol., 35, 175-180, doi:10.3189/172756402781817356, 2002.

Isaksson, E., Karlén, W., Gundestrup, N., Mayewski, P., Whitlow, S., and Twickler, M.: A century of accumulation and temperature changes in Dronning Maud Land, Antarctica, J. Geophys. Res., 101, 7085–7094, doi:10.1029/95jd03232, 1996.

Isaksson, E., van den Broeke, M. R., Winther, J.-G., Karlöf, L., Pinglot, J. F., and Gundestrup, N.: Accumulation and prox- ytemperature variability in Dronning Maud Land, Antarctica, determined from shallow firn cores, Ann. Glaciol., 29, 17–22, doi:10.3189/172756499781821445, 1999.

ISMASS Committee: Recommendations for the collection and syn- thesis of Antarctic Ice Sheet mass balance data, Global Planet. Change, 42, 1-15, doi:10.1016/j.gloplacha.2003.11.008, 2004.

Kaczmarska, M., Isaksson, E., Karlöf, K., Winther, J.-G., Kohler, J., Godtliebsen, F., Ringstad Olsen, L., Hofstede, C. M., van den Broeke, M. R., Van DeWal, R. S. W., and Gundestrup, N.: Accumulation variability derived from an ice core from coastal Dronning Maud Land, Antarctica, Ann. Glaciol., 39, 339–345, doi:10.3189/172756404781814186, 2004.

Karlöf, L., Winther, J. G., Isaksson, E., Kohler, J., Pinglot, J. F., Wilhelms, F., Hansson, M., Holmlund, P., Nyman, M., Pettersson, R., Stenberg, M., Thomassen, M. P. A., van der Veen, C., and van de Wal, R. S. W.: A 1500 years record of accumulation at Amundsenisen western

Dronning Maud Land, Antarctica, derived from electrical and radioactive measurements on a 120 m ice core, J. Geophys. Res., 105, 12471–12483, doi:10.1029/1999JD901119, 2000.

Karlöf, L., Isakson, E., Winther, J. G., Gundestrup, N., Meijer, H., A. J., Mulvaney, R., Pourcher, M., Hofstede, C., Lappegard, G., Petterson, R., van den Broecke, M. R., and van de Wal, R. S. W.: Accumulation variability over a small area in east Dronning Maud Land, Antarctica, as determined from shallow firn cores and snow pits: some implications for ice, J. Glaciol., 51, 343– 352, doi:10.3189/172756505781829232, 2005.

Kaspari, S., Mayewski, P. A., Dixon, D. A., Spikes, V. B., Sneed, S. B., Handley, M. J., and Hamilton, G. S.: Climate variability in west Antarctica derived from annual accumulation-rate records from ITASE firn/ice cores, Ann. Glaciol., 39, 585–594, doi:10.3189/172756404781814447, 2004.

King, M. A., Bingham, R. J., Moore, P., Whitehouse, P. L., Bent- ley, M. J., and Milne, G. A.: Lower satellite-gravimetry estimates of Antarctic sea-level contribution, Nature, 491, 586–589, doi:10.1038/nature11621, 2012.

Kingslake, J., Hindmarsh, R. C. A., Aðalgeirsdóttir, G., Conway, H., Corr, H. F. J., Gillet-Chaulet, F., Martín, C., King, E. C., Mulvaney, R., and Pritchard, H. D.: Full-depth englacial vertical ice sheet velocities measured using phase-sensitive radar, J. Geophys. Res.-Earth, 119, 2604–2618, doi:10.1002/2014jf003275, 2014.

Kjær, H., Vallelonga, P., Svensson, A., Elleskov, L., Kris- tensen, M., Tibuleac, C., Winstrup, M., and Kipfstuhl, S.: An optical dye method for continuous determination of acidity in ice cores, Environ. Sci. Technol., 50, 10485–10493, doi:10.1021/acs.est.6b00026, 2016.

Krinner, G., Magand, O., Simmonds, I., Genthon, C., and Dufresne, J. L.: Simulated Antarctic precipitation and surface mass balance at the end of the 20th and 21th centuries, Clim. Dynam. 28, 215- 230, doi:10.1007/s00382-006-0177-x, 2007.

Lenaerts, J. T. M., van den Broeke, M. R., van den Berg, W. J., van Meijgaard, E., and Munneke, P. K.: A new, high resolution surface mass balance map of Antarctica (1979–2010) based on regional climate modeling, Geophys. Res. Lett., 39, L04501, doi:10.1029/2011GL050713, 2012.

Lenaerts, J. T. M., van Meijgaard, E., van den Broeke, M. R., Ligtenberg, S. R. M., Horwath, M., and Isaksson, E.: Recent snowfall anomalies in Dronning Maud Land, East Antarctica, in a historical and future climate perspective, Geophys. Res. Lett., 40, 1–5, doi:10.1002/grl.50559, 2013.

Lenaerts, J. T. M., Brownvan, J., den Broeke, M. R., Matsuoka, K., Drews, R., Callens, D., Philippe, M., Gorodetskaya, I., van Meijgaard, E., Reymer, C., Pattyn, F., and van Lipzig, N. P.: High variability of climate and surface mass balance induced by Antarctic ice rises, J. Glaciol., 60, 1101–1110, doi:10.3189/2014jog14j040, 2014.

Lenaerts, J. T. M., Vizcaino, M., Fyke, J., van Kampenhout, L., and van den Broeke, M. R.: Present-day and future Antarctic ice sheet climate and surface mass balance in the Community Earth System Model, Clim. Dynam., 47, 1367-1381, doi:10.1007/s00382- 015-2907-4, 2016.

Levasseur, M.: Impact of Arctic meltdown on the microbial cycling of sulphur, Nat. Geosci., 6, 691-700, doi:10.1038/ngeo1910, 2013.

Lingle, C. S., & Troshina, E. N. (1998), Relative magnitudes of shear and longitudinal strain rates in the inland Antarctic ice sheet, and response to increasing accumulation. Ann. Glaciol., 27(1), 187-193.

Ludescher, J., Bunde, A., Franzke, C. L., and Schellnhuber, H. J.: Long-term persistence enhances uncertainty about anthropogenic warming of Antarctica, Clim. Dynam., 46, 263–271, doi:10.1007/s00382-015-2582-5, 2015.

Magand, O., Genthon, C., Fily, M., Krinner, G., Picard, G., Frezzotti, M., and Ekaykin, A. A.: An up-to-date quality-controlled surface mass balance data set for the 90-180E Antarctica sector and 1950-2005 period, J. Geophys. Res., 112, D12106, doi:10.1029/2006JD007691, 2007.

Malone, T., Hubbard, B., Merton-Lyn, D., Worthington, P., & Zwiggelaar, R. (2013), Borehole and Ice Feature Annotation Tool (BIFAT): A program for the automatic and manual annotation of glacier borehole images. Computers & Geosciences, 51, 381-389.

Marshall, G. J.: Trends in the southern annular mode from observations and reanalyses, J. Climate, 16, 4134–4143, doi:10.1175/1520-0442(2003)016<4134:titsam>2.0.co;2, 2003.

Martín, C., Mulvaney, R., Gudmundsson, G. H., & Corr, H. (2015). Inferring palaeo-accumulation records from ice-core data by an adjoint-based method: application to James Ross Island's ice core. Climate of the Past, 11(3), 547-557.

Matsuoka, K., Hindmarsh, R. C., Moholdt, G., Bentley, M. J., Pritchard, H. D., Brown, J., Conway, H., Drews, R., Durand, G., Goldberg, D., Hattermann, T., Kingslake, J., Lenearts, J., Martin, C., Mulvaney, R., Nicholls, K., Pattyn, F., Ross, N., Scambos, T., and Whitehouse, P.: Antarctic ice rises and rumples: their properties and significance for ice-sheet dynamics and evolution, Earth- Sci. Rev., 150, 724–745, doi:10.1016/j.earscirev.2015.09.004, 2015.

Medley, B., Joughin, I., Das, S. B., Steig, E. J., Conway, H., Gogineni, S., Criscitiello, A. S., McConnell, J. R., Smith, B. E., van den Broeke, M. R., Lenaerts, J. T. M., Bromwich, D. H., and Nicolas, J. P.: Airborne-radar and ice-core observations of annual snow accumulation over Thwaites Glacier, West Antarctica confirm the spatiotemporal variability of global and regional atmospheric models, Geophys. Res. Lett., 40, 3649–3654, doi:10.1002/grl.50706, 2013.

Monaghan, A. J., Bromwich, D. H., Fogt, R. L., Wang, S., Mayewski, P. A., Dixon, D. A., Ekaykin, A., Frezzotti, M., Goodwin, I., Isaksson, E., Kaspari, S. D., Morgan, V. I., Oerter, H., Van Ommen, T. D., van der Veen, C. J., and Wen, J.: Insignificant change in Antarctic snowfall since the International Geophysi- cal Year, Science, 313, 827–831, doi:10.1126/science.1128243, 2006.

Moore, J. C., Narita, H., and Maeno, N.: A continuous 770-year record of volcanic activity from East Antarctica, J. Geophys. Res., 96, 17353–17359, doi:10.1029/91jd01283, 1991.

Mosley-Thompson, E., Paskievitch, J. F., Gow, A. J., and Thompson, L. G.: Late 20th century increase in South Pole snow accumulation, J. Geophys. Res., 104, 3877–3886, doi:10.1029/1998jd200092, 1999.

Mulvaney, R., Pasteur, E. C., and Peel, D. A.: The ratio of MSA to non sea-salt sulphate in Antarctic peninsula ice cores, Tellus, 44b, 293–303, doi:10.3402/tellusb.v44i4.15457, 1992.

Nicholls, K. W., Corr, H. F., Stewart, C. L., Lok, L. B., Brennan, P. V., & Vaughan, D. G. (2015). A ground-based radar for measuring vertical strain rates and time-varying basal melt rates in ice sheets and shelves. Journal of Glaciology, 61(230), 1079-1087.

Nishio, F., Furukawa, T., Hashida, G., Igarashi, M., Kameda, T., Kohno, M., Motoyama, H., Naoki, K., Satow, K., Suzuki, K., Morimasa, T., Toyama, Y., Yamada, T., and Watanabe, O.: Annual-layer determinations and 167 year records of past climate of H72 ice core in east Dronning Maud Land, Antarctica, Ann. Glaciol., 35, 471–479, doi:10.3189/172756402781817086, 2002.

Nye, J.F.: Correction factor for accumulation measured by the thickness of the annual layers in an ice sheet. J.Glaciol., 4(36), 785-788, 1963.

Oerter, H., Graf, W., Wilhelms, F., Minikin, A., and Miller, H.: Accumulation studies on Amundsenisen, Dronning Maud Land, by means of tritium, DEP and stable isotope measurements: first results from the 1995/96 and 1996/97 field seasons, Ann. Glaciol., 29, 1-9, doi:10.3189/172756499781820914, 1999.

Oerter, H., Wilhelms, F., Jung-Rothenhausler, F., Goktas, F., Miller, H., Graf, W., and Sommer, S.: Accumulation rates in Dronning Maud Land as revealed by DEP measurements at shallow firn cores, Ann. Glaciol., 30, 27-34, doi:10.3189/172756400781820705, 2000.

Palerme, C., Genthon, C., Claud, C., Kay, J. E., Wood, N. B., and L'Ecuyer, T.: Evaluation of current and projected Antarctic precipitation in CMIP5 models, Clim. Dynam., online first, doi:10.1007/s00382-016-3071-1, 2016.

Parrenin, F., Dreyfus, G., Durand, G., Fujita, S., Gagliardini, O., Gillet, F., Jouzel, J., Kawamura, K., Lhomme, N., Masson- Delmotte, V., Ritz, C., Schwander, J., Shoji, H., Uemura, R., Watanabe, O., and Yoshida, N.: 1-D-ice flow modelling at EPICA Dome C and Dome Fuji, East Antarctica, Clim. Past, 3, 243–259, doi:10.5194/cp-3-243-2007, 2007.

Pettit, E. C., Waddington, E. D., Harrison, W. D., Thorsteinsson, T., Elsberg, D., Morack, J., & Zumberge, M. A. (2011). The crossover stress, anisotropy and the ice flow law at Siple Dome, West Antarctica. Journal of Glaciology, 57(201), 39-52.

Philippe, M., Tison, J.-L., Fjøsne, K., Hubbard, B., Kjær, H. A., Lenaerts, J. T. M., Drews, R., Sheldon, S. G., De Bondt, K., Claeys, P., and Pattyn, F.: Annual layer thicknesses and age-depth (oldest estimate) of Derwael Ice Rise (IC12), Dronning Maud Land, East Antarctica, doi:10.1594/PANGAEA.857574, 2016a.

Philippe, M., Tison, J. L., Fjøsne, K., Hubbard, B., Kjær, H. A., Lenaerts, J. T., ... & Pearce, N. J. G. (2016), Ice core evidence for a recent increase in snow accumulation in coastal Dronning Maud Land, East Antarctica, The Cryosphere Discuss.

Philippe, M., Hubbard, B., Pattyn, F., Fjøsne, K., Drews, R., Bruyninx, C., Bergeot, N., and Tison, J.-L.: Vertical velocities of firn and ice reconstructed from optical televiewer borehole logging at Derwael ice rise, Princess Ragnhild Coast, Antarctica, in preparation, 2017.

Raymond, C.,Weertman, B., Thompson, L., Mosley-Thompson, E., Peel, D., and Mulvaney, R.: Geometry, motion and balance of Dyer Plateau, Antarctica, J. Glaciol., 42, 510–518, 1996.

Ren,J., Li, C., Hou, S., Xiao, C.,Qin, D., Li, Y., and Ding, M.: A 2680 year volcanic record from the DT-401 East Antarctic ice core, J. Geophys. Res., 115, D11301, doi:10.1029/2009JD012892, 2010.

Rignot, E., Velicogna, I., van den Broeke, M. R., Monaghan, A., and Lenaerts, J.: Acceleration of the contribution of the Greenland and Antarctic ice sheets to sea level rise, Geophys. Res. Lett., 38, L05503, doi:10.1029/2011GL046583, 2011.

Rupper, S., Christensen, W. F., Bickmore, B. R. Burgener, L., Koenig,L., S., Koutnik, M. R., Miège, C., and Forster, R. R.: The effects of dating uncertainties on net accumulation estimates from firn cores, J. Glaciol., 61, 163–172, doi:10.3189/2015jog14j042, 2015.

Savitzky, A. and Golay, M. J. E.: Smoothing and Differentiation of Data by Simplified Least Squares Procedures, Anal. Chem., 36, 1627–1639, doi:10.1021/ac60214a047, 1964.

Schlosser, E. and Oerter, H.: Shallow firn cores from Neumayer, Ekströmisen, Antarctica: a comparison of accumulation rates and stable-isotope ratios, Ann. Glaciol., 35, 91–96, doi:10.3189/172756402781816915, 2002.

Schlosser, E., Manning, K. W., Powers, J. G., Duda, M. G., Birnbaum, G., and Fujita, K.: Characteristics of high-precipitation events in Dronning Maud Land, Antarctica, J. Geophys. Res., 115, D14107, doi:10.1029/2009JD013410, 2010.

Shepherd, A., Ivins, E. R., Geruo, A., Barletta, V. R., Bentley, M. J., Bettadpur, S., Briggs, K. H., Bromwich, D. H., Forsberg, R., Galin, N., Horwath, M., Jacobs, S., Joughin, I., King, M. A., Lenaerts, J. T. M., Li, J., Ligtenberg, S. R. M., Luckman, A., Luthcke, S. B., McMillan, M., Meister, R., Milne, G., Mouginot, J., Muir, A., Nicolas, J. P., Paden, J., Payne, A. J., Pritchard, H., Rignot, E., Rott, H., Sørensen, L. S., Scambos, T. A., Scheuchl, B., Schrama, E. J. O., Smith, B., Sundal, A. V., van Angelen, J. H., van de Berg, W. J., van den Broeke, M. R., Vaughan, D. G., Velicogna, I., Wahr, J., Whitehouse, P. L., Wingham, D. J., Yi, D., Young, D., and Zwally, H. J.: A reconciled estimate of ice-sheet mass balance, Science, 338, 1183–1189, doi:10.1126/science.1228102, 2012.

Sigl, M., McConnell, J. R., Layman, L., Maselli, O., McGwire, K., Pasteris, D., Dahl-Jensen, D., Steffensen, J. P., Vinther, B., Edwards, R., Mulvaney, R., and Kipfstuhl, S.: A new bipolar ice core record of volcanism from WAIS Divide and NEEM and implications for climate forcing of the last 2000 years. J. Geo- phys. Res.-Atmos., 118, 1151–1169, doi:10.1029/2012jd018603, 2013.

Spikes, V. B., Csathó, B. M., Hamilton, G. S., & Whillans, I. M. (2003). Thickness changes on Whillans Ice Stream and Ice Stream C, West Antarctica, derived from laser altimeter measurements. Journal of Glaciology, 49(165), 223-230.

Steig, E., Fischer, H., Fisher, D., Frezzotti, M., Mulvaney, R., Taylor, K., and Wolff, E.: The IPICS 2k Array: a network of ice core climate and climate forcing records for the last two millennia, http://pages-igbp.org/download/docs/working_groups/ipics/ white-papers/IPICS_2kArray.pdf (last access: 14 October 2016), IPICS (International Partnership in Ice Core Science), 2005.

Thomas, E. R., Marshall, G. J., and McConnell, J. R.: A doubling in snow accumulation in the western Antarctic Peninsula since 1850, Geophys. Res. Lett., 35, L01706, doi:10.1029/2007GL032529, 2008.

Thomas, E. R., Hosking, J. S., Tuckwell, R. R., Warren, R. A., and Ludlow, E. C.: Twentieth century increase in snowfall in coastal West Antarctica, Geophys. Res. Lett., 42, 9387–9393, doi:10.1002/2015GL065750, 2015.

Traufetter, F., Oerter, H., Fischer, H., Weller, R., and Miller, H.: Spatio-temporal variability in volcanic sulphate deposition over the past 2 kyr in snow pit and fir cores from Amundsenisen, Antarctica, J. Glaciol., 50, 137–146, doi:10.3189/172756504781830222, 2004.

Turner, J., Colwell, S. R., Marshall, G. J., Lachlan-Cope, T. A., Carleton, A. M., Jones, P. D., Lagun, V., Reid, P. A., and Iagovkina, S.: Antarctic climate change during the last 50 years, Int. J. Climatol., 25, 279–294, doi:10.1002/joc.1130, 2005.

van de Berg, W. J., van den Broeke, M. R., Reijmer, C. H., and van Meijgaard, E.: Reassessment of the Antarctic SMB using calibrated output of a regional atmospheric climate model, J. Geophys. Res., 111, D11104, doi:10.1029/2005JD006495, 2006.

van den Broeke, M., van de Berg, W. J., and van Meijgaard, E.: Snowfall in coastal West Antarctica much greater than previously assumed, Geophys. Res. Lett., 33, L02505, doi:10.1029/2005GL025239, 2006.

Vaughan, D. G., Comiso, J.C., Allison, I., Carrasco, J., Kaser,G., Kwok, R., Mote, P., Murray, T., Paul, F.,Ren, J., Rignot, E., Solomina, O., Steffen, K., and Zhang, T.: Observations: Cryosphere, in: Climate Change 2013: The Physical Science Basis. Contribution of Working Group I to the Fifth Assessment Re- port of the Intergovernmental Panel on Climate Change, edited by: Stocker, T. F., Qin, D., Plattner, G.-K., Tignor, M., Allen, S. K., Boschung, J., Nauels, A., Xia, Y., Bex, V., and Midgley, P. M., Cambridge University Press, Cambridge, United Kingdom and New York, NY, USA, 2013.

Wang, Y., Ding, M., van Wessem, J., Schlosser, E., Altnau, S., van den Broeke, M., Lenaerts, J., Thomas, E., Isaksson, E., Wang, J., and Sun, W.: A comparison of Antarctic Ice Sheet surface mass balance from atmospheric climate models and in situ observations, J. Climate, doi:10.1175/JCLI-D-15-0642.1, early online release, 2016.

Wolff, E. W., Jones, A. E., Bauguitte, S. J.-B., and Salmon, R. A.: The interpretation of spikes and trends in concentration of ntrate in polar ice cores, based on evidence from snow and atmospheric measurements, Atmos. Chem. Phys., 8, 5627–5634, doi:10.5194/acp-8-5627-2008, 2008.

Zhang, M., Li, Z., Ren, J., Xiao, C., Qin, D., Kang, J., and Li, J.: 250 years of accumulation, oxygen isotope and chemical records in a firn core from Princess Elizabeth Land, East Antarctica, J. Geogr. Sci., 16, 23–33, doi:10.1007/s11442-006-0103-5, 2006.